

Chapter 2

Remote Sensing

Remote sensing is a method of obtaining information from distant objects without direct contact. This is possible due to the existence or the generation of force fields between the sensing device and the sensed object. Usable force fields are mechanical waves in solid matter (seismology) or in liquids (sound waves). But the principal force field used in remote sensing is that of electromagnetic energy, as characterized by the Maxwell equations. The emission of electromagnetic waves is suitable for directional separation. Thus, images of the radiation incident on a sensor may be generated and analyzed.

The remote sensing principle using waves of the electromagnetic spectrum is illustrated in [Figure 2.1](#). The energy radiates from an energy source. A passive (naturally available) energy source is the sun. An active energy source may be a lamp, a laser, or a microwave transmitter with its antenna. The radiation propagates through a vacuum with the speed of light, c , at about 300,000 km/second. It reaches an object, where it interacts with the matter of this object. Part of the energy is reflected toward the sensor. At the sensor, which is carried on a platform, the intensity of the incoming radiation is quantized and stored. The stored energy values are transformed into images, which may be subjected to image processing techniques before they are analyzed to obtain object information.

ELECTROMAGNETIC RADIATION

Basic Laws

Electromagnetic energy is radiated by any body having a temperature higher than -273°C (or 0 K), the absolute zero temperature. Such a body radiates energy in all frequencies. The relation between frequency, ν , and wavelength, λ , is expressible as

$$\lambda = \frac{c}{\nu}$$

with λ expressed in meters and frequency in cycles per seconds (i.e., Hertz).

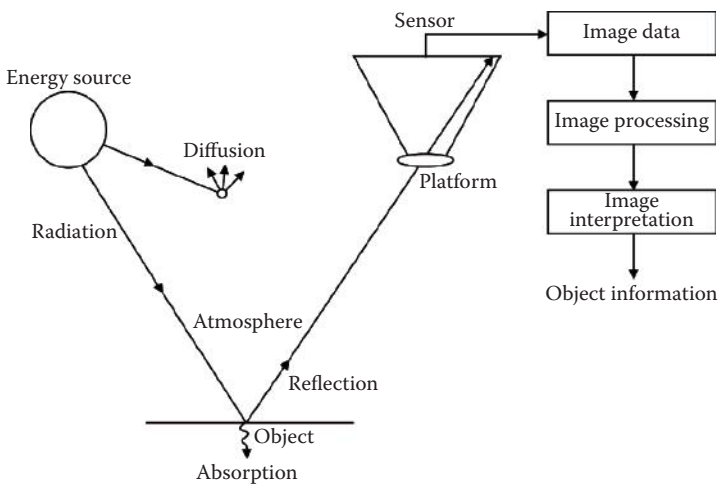


Figure 2.1 Principles of remote sensing.

The amount of radiation for a particular wavelength over an interval, $\Delta\lambda$, is a function of the absolute temperature of the body in kelvins and is expressed by Planck's distribution law

$$L_\lambda(T) = \frac{2h \cdot c^2}{\lambda^5} \cdot \frac{1}{e^{hc/\lambda \cdot kT} - 1}$$

where

$L_\lambda(T)$ = spectral radiance in $\text{W/m}^2 \cdot \text{sr} \cdot \mu\text{m}$

$k = 1.38047 \cdot 10^{-23} [\text{W} \cdot \text{s} \cdot \text{K}^{-1}]$, the Boltzmann constant

$h = 6.6252 \cdot 10^{-34} [\text{J} \cdot \text{s}]$, the Planck's constant

$c = 2.997925 \cdot \text{cm}^8/\text{s}$

This is based upon the observation that energy is emitted in energy quanta, Q_p [$\text{J} = \text{W} \cdot \text{s}$]. Wien's law permits us to determine the radiation maximum at a particular wavelength, λ_{\max} , depending on the body temperature by differentiating $L_\lambda(T)$ with respect to λ :

$$\lambda_{\max} = \frac{0.002898}{T} \cdot \frac{[\text{mL}]}{[\text{K}]}$$

Since the surface temperature of the sun is about 6000 K, this means that the maximum radiance from solar energy will be generated at a wavelength of 480 nm, which corresponds to green light. The earth, with its temperature

TABLE 2.1 RADIOMETRIC QUANTITIES

	Name	Symbol	Relation	Dimension	
Radiator	Radiant energy	Q	—	Joule	$J = W \cdot s$
	Radiant flux	Φ	$\Phi = \frac{Q}{t}$	Watt	$W = J/s$
	Radiant intensity	I	$I = \frac{Q}{t \cdot \omega_1}$	—	W/sr
	Radiance	L	$L = \frac{Q}{t \cdot A_1 \omega_1}$	—	$W/sr \cdot m^2$
Emitted object	Radiant emittance	E	$E = \frac{\Phi}{A_1}$	—	W/m^2
Received signal	Irradiance exposure	E'	$E' = \frac{\Phi}{A_2}$	—	W/m^2
		H	$H = E' \cdot t$	—	$W \cdot s/m^2$

Notes: ω_1 , space angle of radiation in sterad (sr); A_1 , radiating surface in square meters (m^2); A_2 , irradiated surface in square meters (m^2).

between 273 and 300 K ($0^\circ C$ and $27^\circ C$) has its radiance maximum in the thermal range of the spectrum (8 μm to 14 μm).

Radiometric Quantities

The dimensions of radiometric quantities used in absolute remote sensing are shown in Table 2.1.

Electromagnetic Spectrum

The characteristics of electromagnetic energy in the electromagnetic spectrum are shown in Table 2.2.

ENERGY–MATTER INTERACTION

Atmospheric Transmission

Electromagnetic transmission through the atmosphere slows the wave propagation depending on the transmission coefficient, n :

$$\lambda = \frac{c}{v \cdot n}$$

TABLE 2.2 ELECTROMAGNETIC SPECTRUM

Radiation Type	Wavelength	Frequency	Transmission	Use	Detector
Cosmic rays	10^{-13} to 10^{-16}	4.7×10^{21} Hz to 3×10^{24} Hz	Outer space	—	Ionization detector
γ -rays	10^{-4} nm to 0.4 nm (nm = 10^{-9} m)	8×10^{16} to 4.7×10^{21} Hz	Limited through atmosphere	Radioactivity	Ionization detector
X-rays	0.4–10 nm	3×10^{16} to 8×10^{16} Hz	Only at close range outer space	Close range	Phosphorus
Ultraviolet light	10–380 nm	7.9×10^{14} to 3×10^{16} Hz	Weak through atmosphere	—	Phosphorus
Visible light	380–780 nm	3.8×10^{14} to 7.9×10^{14} Hz	Well through atmosphere	Passive remote sensing, vision	Photography, photodiode
Near infrared	780 nm–1 μ m (m = 10^{-6} km)	3.0×10^{24} to 3.8×10^{14} Hz	Well through atmosphere	Passive remote sensing	Photography, photodiode
Medium infrared	1–8 μ m	3.7×10^{13} to 3.0×10^{14} Hz	In windows through atmosphere	Passive remote sensing	Quantum detector
Thermal infrared	8 μ m–1 mm (mm = 10^{-3})	3×10^{11} to 3.7×10^{13} Hz	In windows through atmosphere, day and night	Passive remote sensing	Quantum detector
Thermal infrared	8 μ m–14 μ m (to 1 mm) (mm = 10^{-3})	3×10^{11} to 3.7×10^{13} Hz	In windows through atmosphere, day and night	Passive remote sensing	Quantum detector

Microwaves	1 mm–1 m	300 MHz to 300 GHz (MHz = 10^6 Hz, GHz = 10^9 Hz)	Day and night through clouds	Active remote sensing	Antenna
FM radio	1–10 m	30–300 MHz	Direct visibility	TV, broadcast	Antenna
Short-wave radio	10–100 m	3–30 MHz	Worldwide	Broadcast	Antenna
Medium-wave broadcast	182 m–1 km	300–1650 kHz (kHz = 10^3 Hz)	Regional	Broadcast	Antenna
Long-wave broadcast	1–10 km	30–300 kHz	Worldwide	Broadcast	Antenna
Sound transmission	15–600 km	50 Hz–20 kHz	Cable	Telephone	Cable
AC	6000 km	50 Hz	Cable	Energy transmission	Cable

Furthermore, part of the energy is absorbed when the energy quanta hit the molecules and atoms of the atmospheric gases.

Another part is directionally reflected into diffused energy causing scattering, according to Rayleigh.

$$I_{\text{transmitted}} = I_{\text{original}} \cdot \exp(-kr)$$

where

k = extinction coefficient

r = distance passed through

k is proportional to λ^{-4}

In the infrared ranges of the spectrum, absorption takes place by gases contained in the atmosphere, so that transmission is possible only in atmospheric windows, as shown in [Figure 2.2](#).

Energy Interaction at the Object

Interaction of incident electromagnetic energy with matter depends on the molecular and atomic structure of the object. Energy may be directionally reflected, scattered, transmitted, or absorbed. The process is caused by the interaction of a photon with an electron located in a shell of an atom, which results in the excitation of the electron from the shell. The ratio between the reflected (in all directions), transmitted, and absorbed fluxes or radiances and the incoming radiation is described as:

Reflection coefficient, ρ_λ

Transmission coefficient, τ_λ

Absorption coefficient, α_λ

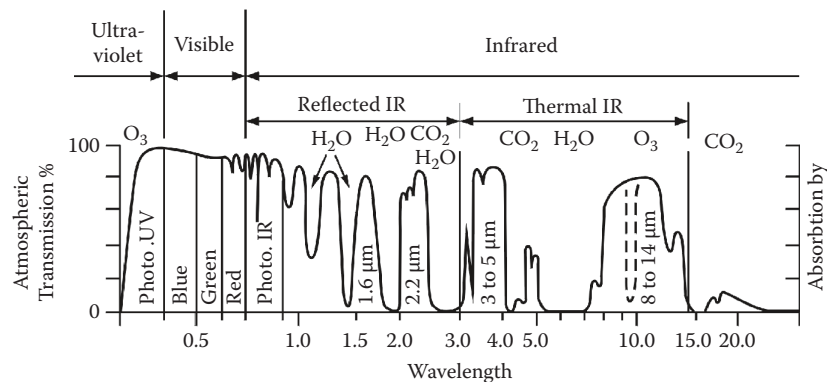


Figure 2.2 Atmospheric windows.

Their sum is equal to 1:

$$\rho_\lambda = \frac{\phi_{\lambda \text{ reflected}}}{\phi_{\lambda \text{ incoming}}}$$

$$\tau_\lambda = \frac{\phi_{\lambda \text{ transmitted}}}{\phi_{\lambda \text{ incoming}}}$$

$$\alpha_\lambda = \frac{\phi_{\lambda \text{ absorbed}}}{\phi_{\lambda \text{ incoming}}}$$

$$\rho_\lambda + \tau_\lambda + \alpha_\lambda = 1$$

Other than through atmospheric particles, transmission is possible, for example, for water. Nontransparent solid bodies have a transmission coefficient of 0.

The incoming energy cannot get lost. Absorption is a process in which higher frequency energy (e.g., light) is converted to lower frequency energy (e.g., heat).

The reflection coefficient of an object is of crucial importance for remote sensing. It varies for different spectral ranges for a particular object. It is characterized by an angle dependent function, the so-called radiometric function:

$$\rho_\lambda(\epsilon_1, \epsilon_2, \epsilon_3) = \rho_{\lambda 0} f(\epsilon_1, \epsilon_2, \epsilon_3) = \rho_\lambda \text{ (solar position)}$$

in which $\rho_{\lambda 0}$ is the normal reflection coefficient, valid for an object illuminated and reflected in the same direction. ϵ_1 is the spatial angle between the direction of illumination and the surface normal. ϵ_2 is the spatial angle between the direction of the sensor and the surface normal. ϵ_3 is the spatial angle between the direction of illumination and the direction to the sensor.

The normal reflection coefficients vary for different object types, for example, for green light:

Coniferous forest, 1%
Water, 3%
Meadow, 7%
Road, 8%
Deciduous forest, 18%
Sand, 25%
Limestone, 60%
New snow, 78%

The spectral reflectance varies with each object type, as shown in Figure 2.3 for soil and vegetation.

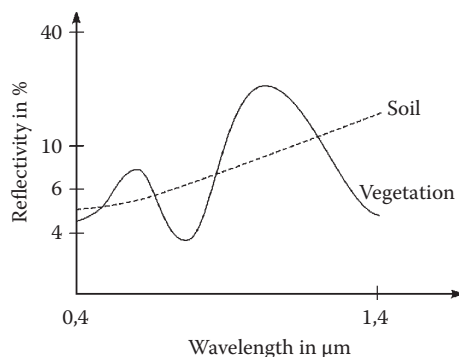


Figure 2.3 Spectral reflectance.

Interaction of Energy in Plants

Whereas the reflection on smooth object surfaces is simple, the interaction of energy in plants is more complicated. A plant leaf consists of at least three layers (Figure 2.4):

- Transparent epidermis
- A palisade type mesophyll, which reflects green light and absorbs red, due to its chlorophyll content
- A spongy type mesophyll that reflects near infrared

Energy Arriving at the Sensor

The radiant density flux arriving at a sensor is composed of the following terms: the radiant flux of solar radiation, E_λ , is diminished by the solar altitude ($90^\circ - \epsilon_1$) and the transmission coefficient of the atmosphere $\tau_{\lambda_{\epsilon_1}}$ for the incident ray to result in the radiant flux of the object: E_{ϵ_1} :

$$E_{\epsilon_1} = \cos \epsilon_1 \int_{\lambda_1}^{\lambda_2} E_\lambda \cdot \tau_{\lambda_{\epsilon_1}} \cdot d\lambda$$

The reflection at the object is dependent on the radiometric function. In case the object is a Lambert reflector, reflecting all incident energy into the half sphere with equal intensity, $f(\epsilon_1, \epsilon_2, \epsilon_3)$ becomes equal to 1.

The radiant flux arriving at the sensor then becomes

$$E_{\epsilon_2} = \frac{\cos \epsilon_1}{\pi} \int_{\lambda_1}^{\lambda_2} E_\lambda \cdot \tau_{\lambda_{\epsilon_1}} \cdot \tau_{\lambda_{\epsilon_2}} \cdot \rho_\lambda \cdot d\lambda$$

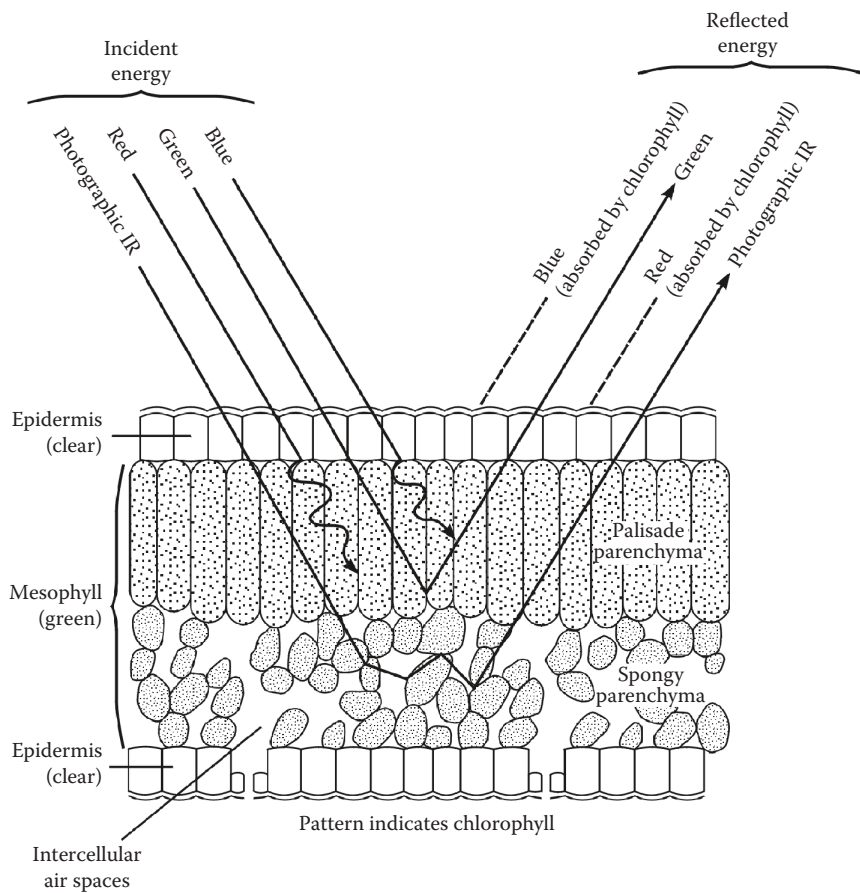


Figure 2.4 Cross-section of a leaf.

with $\tau_{\lambda_{e2}}$ as the transmission coefficient of the atmosphere between object and sensor, and the reflection coefficient, ρ_λ , equal in all directions of reflection.

The actual radiant flux arriving at the sensor, as far as its intensity is concerned, is still augmented, however, by the diffused light of the atmosphere $\rho_{e,\lambda}$, which amounts to about 3%. It is strongly wavelength dependent.

Thus, the incident radial flux, E , at the sensor becomes:

$$E = \frac{1}{\pi} \int_{\lambda_1}^{\lambda_2} E_\lambda (\tau_{\lambda_{e1}} \cdot \tau_{\lambda_{e2}} \cdot \rho_\lambda \cdot \cos \epsilon_1 + \rho_{e,\lambda}) d\lambda$$

E_λ can be derived from solar parameters. The transmission coefficients of the atmosphere can be determined from radiometric measurements of the solar illumination with radiometers directed at the sun and the total illumination of the half sphere, measurable by an Ulbricht sphere in front of the radiometer. With ϵ_1 known and $\rho_{\epsilon_1 \lambda}$ estimated for the diffused light, remote sensing can be treated as a procedure of absolute radiometry.

To use this absolute methodology is, however, impractical because of the need to measure atmospheric transmission parameters and because of assumptions for the radiometric function and the scattered energy.

Thus, remote sensing generally restricts itself to a relative comparison of directionally separable radiant fluxes or radiances of adjacent objects A and B

$$\frac{E_A}{E_B} = \frac{L_A}{L_B} = \frac{\rho_A}{\rho_B}$$

as E_λ , $\tau_{\lambda \epsilon_1}$, $\cos \epsilon_1$, and $d'(x, y)$ are nearly equal in this case.

SENSOR COMPONENTS

The classical remote sensing device is photography.

Optical Imaging

The first historical device to create an image of a scene was the pinhole camera. It contains a small circular hole, which can be considered as the projection center. Light rays passing through this hole may be imaged in an image plane at an arbitrary distance.

The disadvantage of the pinhole camera is that the incident radiation in the image plane is too weak for practical purposes. Optical lenses permit the collection of more radiation. To be imaged the lenses must, however, focus the image according to the condition

$$\frac{1}{a} + \frac{1}{b} = \frac{1}{f}$$

in which a is the distance between the projection center and object point, b is the distance between the projection center and image point, and f is the focal length of the spherically shaped lens.

Simple lenses suffer a number of sharpness restrictions, such as

- Chromatic aberration, which focuses light of different wavelengths in separate image planes

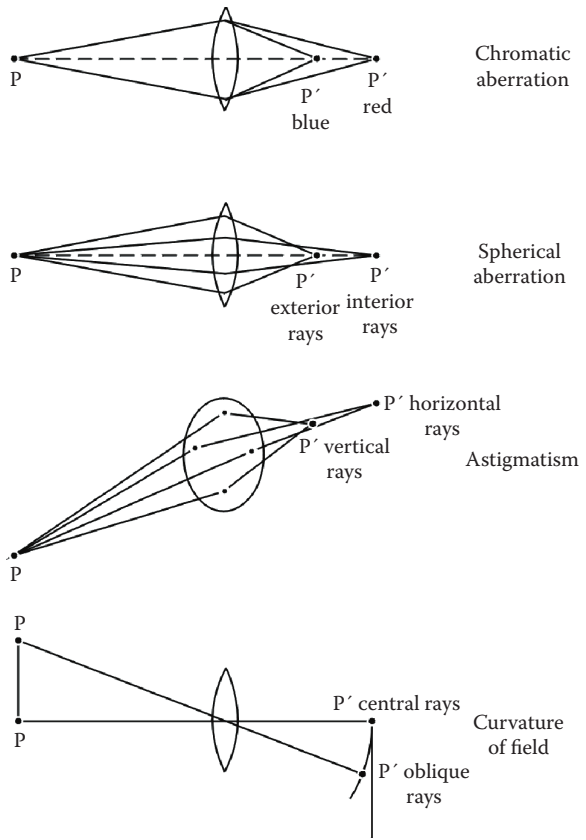


Figure 2.5 Lens errors.

- Spherical aberrations, which collect the inner rays of the lens in different planes with respect to the outer rays of the lens
- Astigmatism, which causes the rays passing vertically through the lens to be collected in a different plane than for the horizontal rays
- Curvature of the field causes the outer rays and the inner rays passing through the lens not in a plane but on a spherical surface (see [Figure 2.5](#))

Lens manufacturers have therefore attempted to combine lenses of different refractive indices, correcting the sharpness deficiencies of simple lenses.

The amount of energy arriving in the image plane through a lens system with the diaphragm, d , is a function of the angle α between its optical axis and the imaged point. This function is influenced by the longer path of the ray, the transmission coefficient of the lens system, and the diameter. For a single lens,

the irradiance diminishes with $\cos^4\alpha$. Objectives are able to reduce the light fall off to a function $\cos^{2.5}\alpha$.

The exposure, H , at a point on the optical axis of the image plane thus becomes

$$H = E \cdot \left(\frac{d}{f} \right)^2 \cdot \frac{\pi}{4} \cdot \tau_0 \cdot t$$

with E being the radiant radial flux at the sensor, d the diaphragm of the optics, f the focal length, t the exposure time, and τ_0 the transmission coefficient of the objective in the direction of the object, which is α dependent.

Photographic Process

The optically produced image in the image plane can be recovered by the photographic process on a film. A layer of film consists of silver halides embedded in gelatin forming the emulsion. When light falls on the emulsion, the silver halide particles are in part chemically converted into metallic silver. The amount of this conversion is proportional to the irradiance.

During the wet development process in the laboratory by methylhydrochion, the conversion process is continued. A second wet process, the fixation, stops the conversion and dissolves the remaining silver halides. After a washing process, the metallic silver becomes visible. Thereafter, the film is subjected to a drying process in which a film negative that can be copied is produced. It may be copied by illumination onto a copying film, which is subjected to the same process of development, fixation, washing, and drying to produce a diapositive.

The gray level of the produced metallic silver on negative or diapositive corresponds to a logarithmic function of the irradiance. This is shown in [Figure 2.6](#) as the so-called D-log E curve, which should better be called the D-log H curve linking photographic density to irradiance.

The D-log H curve is characteristic for a particular film type. Exposure of the entire irradiance range of the scene should be chosen within the linear range of the D-log H curve. In this range, the slope of the curve is equal to the gradation γ :

$$\tan \alpha = \frac{\Delta D}{\Delta \log H} = \gamma$$

The gradation of the film can be influenced by the development process.

$\gamma < 1$ is called a soft development

$\gamma = 1$ is a normal development

$\gamma >$ is a hard development

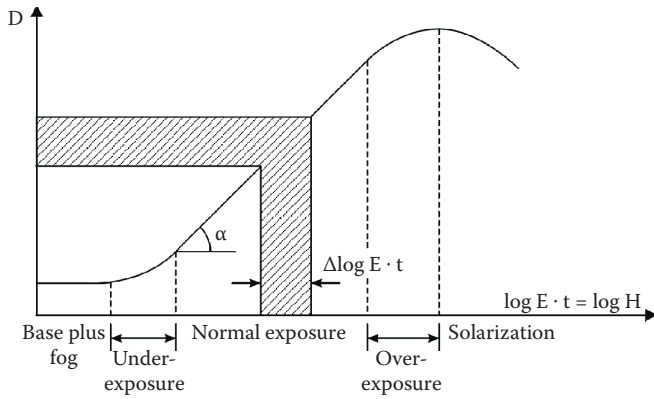


Figure 2.6 D–log H curve.

γ can be changed by the choice of the photographic material, by the developer type, by the temperature of the developer, and by the duration of the development process.

If the development process is fixed as a standard for the type of developer, temperature, and the duration of development, then the sensitivity of the film material can be defined (see Figure 2.7).

A point A on the density curve is reached when the density difference ΔD above fog is 0.1. For this point, the sensitivity in ASA or ISO is

$$\frac{0.8}{H_A}$$

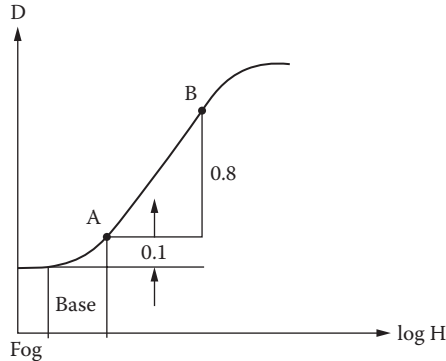


Figure 2.7 Photographic sensitivity.

and the sensitivity in DIN is:

$$10 \cdot \log \frac{1}{H_A}$$

The development process is fixed as a standard so that an irradiance difference $\Delta \log H_{AB} = 1.30$ corresponds to a density difference $\Delta D_{AB} = 0.8$. Silver halides are most sensitive to blue light, which is heavily influenced by scattering in the atmosphere. If this scattering effect is to be minimized, imaging through a yellow filter is mandatory.

The addition of optical dyes permits us to extend the sensitivity of a film into the near-infrared region, not visible to the eye, in which vegetation reflects heavily. Thus, special film types have become available for the visible spectrum or for the spectral range from green to infrared, filtering out the blue light (see [Figure 2.8](#)).

The gray value of the negative or diapositive is determined by the transparency of the developed emulsion. Transparency is the ratio between the light flux passing the emulsion ϕ and the incoming light flux ϕ_0 :

$$\tau = \frac{\phi}{\phi_0}$$

$1/\tau$ is called the opacity; density D is defined as:

$$D = \log \frac{1}{\tau}$$

Color and Color Photography

As human vision has the ability to distinguish different frequency components of the radiances of objects in the form of color, a definition of the color system has been necessary. The Commission Internationale de l'Eclairage (CIE) has defined the three principal colors for the following wavelengths:

Blue = 435.8 nm

Green = 546.1 nm

Red = 700.0 nm

Each perceived color corresponds to an addition of the three principal color components. All colors can be represented in the CIE chromaticity diagram shown in [Figure 2.9](#).

If the colors red, green, and blue are equally represented, their mixing appears to the eye as white at a particular intensity (brightness). On the outside curve of the diagram are pure colors corresponding to a particular frequency between 380 nm and 770 nm. These represent the hue (dominant wavelength) of the light received. Inside the diagram a particular light, coming from a mix of frequencies, is represented by the saturation (purity) of a color.

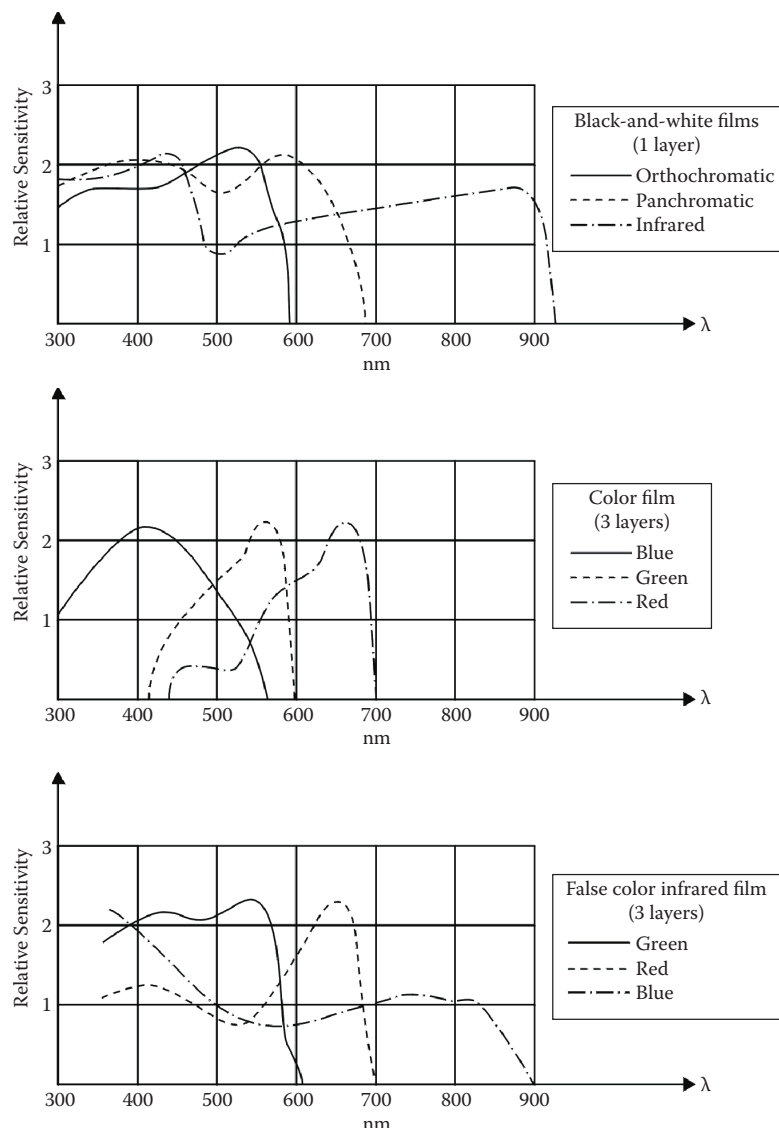
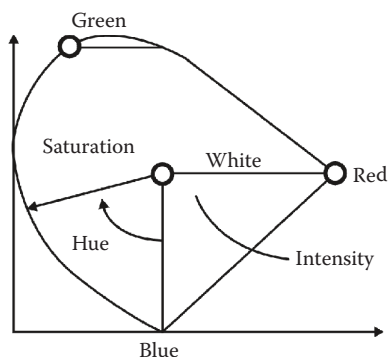


Figure 2.8 Spectral sensitivity of different films.

The colors may be generated artificially by the projection of images of different gray levels in the three primary colors (color additive process). This is the case for a computer or television screen, where three images filtered for the three primary colors are added.



$$\begin{pmatrix} I \\ V_1 \\ V_2 \end{pmatrix} = \begin{pmatrix} 1/3 & 1/3 & 1/3 \\ -1/\sqrt{6} & -1/\sqrt{6} & 2/\sqrt{6} \\ 1/\sqrt{6} & -1/\sqrt{6} & 0 \end{pmatrix} \cdot \begin{pmatrix} d_3 \\ d_2 \\ d_1 \end{pmatrix};$$

$$H = \operatorname{tg}^{-1}(V_2 / V_1);$$

$$S = \sqrt{V_1^2 + V_2^2};$$

with $I = \text{Intensity}$

$H = \text{Hue}$

$d_1 = \text{Density in blue}$

$d_2 = \text{Density in green}$

$d_3 = \text{Density in red}$

Figure 2.9 Chromaticity diagram.

In most photographic work, a color subtractive process is used by absorption filters. This is based on the subtraction of a color from white:

$$\text{White} - \text{Red} = \text{Cyan}$$

$$\text{White} - \text{Green} = \text{Magenta}$$

$$\text{White} - \text{Blue} = \text{Yellow}$$

In color or false color films, three separate film layers are used, which have been sensitized and filtered for the three principal spectral ranges. A color film has a blue sensitive layer followed by a yellow filter, then a green sensitive layer, and finally a red sensitive layer attached to a film base.

Let us now look at the exposure and development process. For color reversal films producing a diapositive, the exposure with blue, green, and red light will initiate the creation of metallic silver in the respective layers. The film is subjected to a black-and-white development. This develops the metallic silver in the respective layers. The result is a black-and-white negative, which is still

light sensitive in the unexposed layers. A short subsequent illumination of the film will therefore create silver in the previously unexposed layers. This silver is color developed with color dyes in complementary colors (cyan for red, magenta for green, and yellow for blue). Bleaching of the film will convert all noncolor coupled metallic silver into soluble silver salts. Thus, a film will be the result, which in transparent viewing will yield the original object colors.

Color negative films possess the same three layers, which expose metallic silver in the respective layers. However, the generated silver is directly developed with the color dyes in complementary colors, creating the oxidation product, which cannot be removed by the bleaching process. Thus, a color negative will result, which when copied by the same process can yield a color image in the original colors.

False color photography utilizes three layers sensitive to green, red, and near infrared. The development process is similar to that of color reversal film. The green sensitive layer appears blue in the resulting diapositive, the red sensitive layer in blue, and the infrared sensitive layer in red. The false color film is particularly useful in interpreting the health of vegetation.

Digital Imaging

The irradiated element of a digital imaging system is a photodiode. This charge-coupled device (CCD) consists of a metallic electrode on a silicon semiconductor separated by an oxide insulator. An incoming photon is attracted by the positive voltage of the electrode. A charge is thereby created at the semiconductor acting as a capacitor. The charge is proportional to the number of photons arriving at the electrode (see [Figure 2.10](#)).

CCDs are now available at a pixel size up to 5 μm . They may be grouped into linear arrays.

To read out the charges of the diodes of a linear array, a voltage is applied, so that the charge of one diode is shifted to the next one along. This process is repeated until the charges of the whole line are shifted to a storage array as an analogue video signal (see [Figure 2.11](#)).

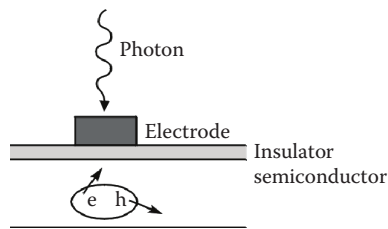


Figure 2.10 CCD detector.

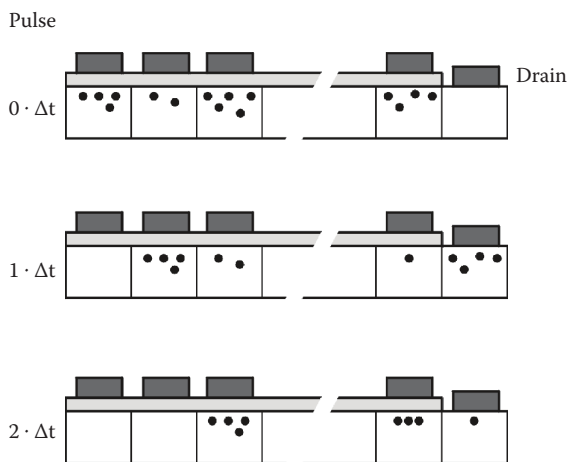


Figure 2.11 Charge transfer in a CCD array.

This video signal can be captured using a tuning signal up to 30 times per second by an analogue to digital converter, called a “frame grabber.” The frame grabber captures the exposure as a digital gray level value for later digital processing.

CCD area sensors are composed of several linear arrays arranged in a matrix fashion. The readout into a storage zone occurs line by line in parallel. While the signal is digitally converted in the frame grabber, a new image can be exposed.

The resolution of CCD sensors is limited by the sensor area and by the distance between the sensor elements. These determine a maximal sampling frequency. The geometrical properties of the sensor are governed by the precision with which the sensor elements may be positioned in the image plane.

In contrast to photography, which has a logarithmic D–log H curve, digital sensors have a linear D–H response. As a rule, the digital quantization of the gray level signals is in 2^8 or 256 bits. Newer sensors permit quantization to 2^{11} or 2048 gray levels.

IMAGING SENSORS

Aerial Survey Cameras

Aerial survey cameras must meet stringent requirements to reach high resolution and low geometric distortion for the image. This is achieved through the design of a suitable objective, as shown in Figures 2.12 and 2.13.

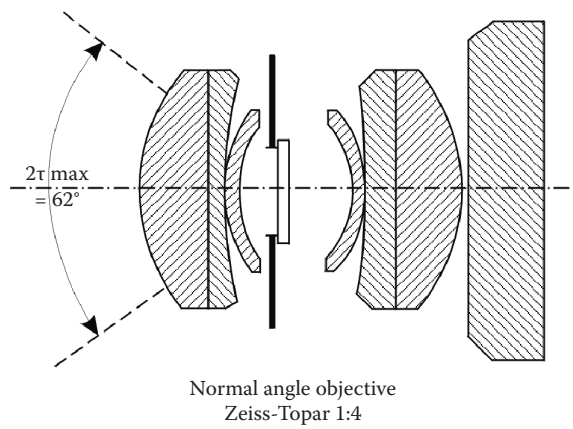


Figure 2.12 Normal angle objective.

The objective is placed into a vibration damped mount in a vertical hole in the floor of an aircraft. The camera has a rigid frame in the image plane carrying the fiducial marks, which permit the location of the principal point of the camera. The knowledge of the principal point in the image plane is important, as it defines the interior orientation for the application of the perspective laws according to which an image can be geometrically restituted. The relation of an objective with respect to the image plane is shown in Figure 2.14.

The aerial film of up to 120 m length and 24 cm width is contained in a cassette mounted on top of the image plane. It contains a pressure plate, which at the time of the exposure is pressed against the image frame. At that time, the film guided through the image plane is pressed onto the pressure plate by a vacuum system to ensure the flatness of the exposed film. For that purpose,

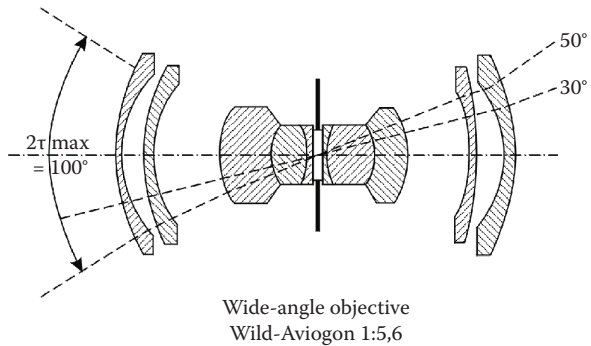


Figure 2.13 Wide-angle objective.

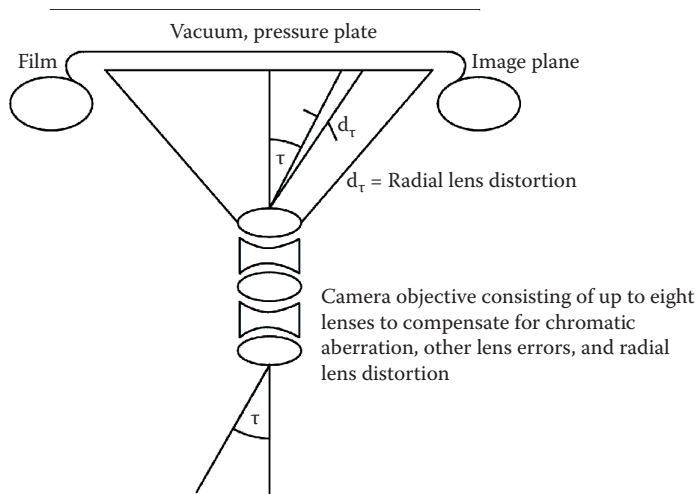


Figure 2.14 Image plane and objective.

the pressure plate is equipped with suction holes. After the exposure, the film pressure is released to allow forward motion of the film for the next exposure by about 25 cm, accounting for the standardized image format of 23×23 cm.

Photography is controlled by a rotating shutter, permitting a simultaneous exposure of all parts of the image every 2 seconds for a duration between 1/100 and 1/1000 of a second. The more recent camera types (Leica RC 30 and Zeiss RMK TOP) permit a forward motion of the film during the exposure to enable the exposure of the same terrain for longer intervals, while the airplane moves forward, permitting the use of high-resolution film, which, due to its smaller silver halide grains, needs a longer exposure time for an exposure falling into the linear part of the D-log H curve. This image motion compensation generally improves the achievable resolution (see [Figure 2.15](#)).

[Figures 2.16](#) and [2.17](#) show the aerial camera types produced by the manufacturers LH-Systems and Z/I Imaging.

A systematic survey of the terrain is only possible if the camera frame is oriented in parallel in the flight direction. To eliminate the crab angle between camera orientation and the flight axis, the camera is rotated within the mount by a mechanism (see [Figure 2.18](#)).

Older cameras control this movement by the flight photographer using an overlap regulator consisting of a ground glass image plane onto which the ground is continuously imaged while the aircraft moves forward. The overlap regulator permits the control of exposure interval of more than 2 seconds, so that a particular overlap of ordinarily 60% in the flight direction is achieved. Newer cameras

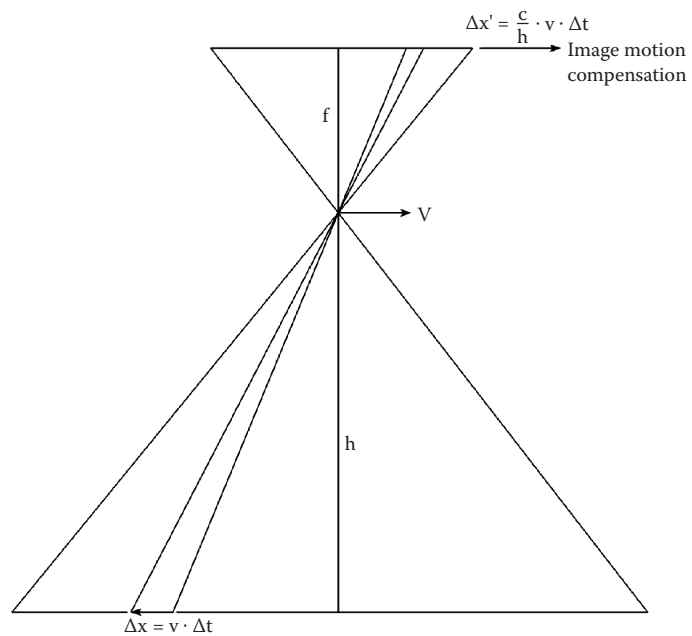


Figure 2.15 Image motion compensation.



Figure 2.16 The LH Systems RC30 camera.

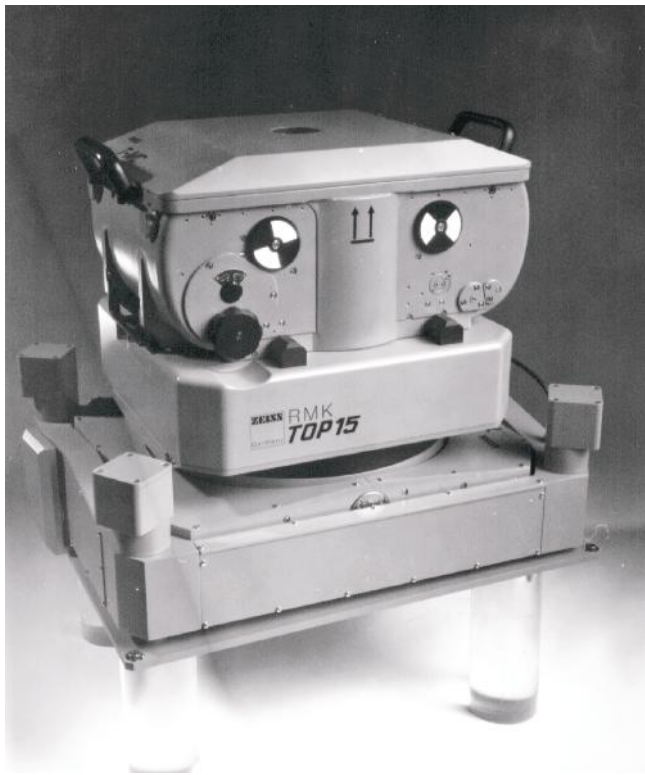


Figure 2.17 The Z/I RMK TOP camera. (Courtesy of Z/I Imaging Corporation, Oberkochen, Germany.)

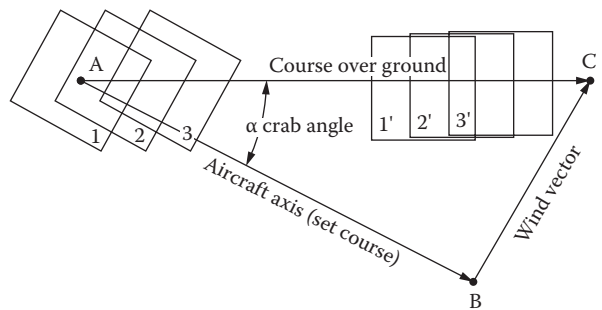


Figure 2.18 Crab angle.

TABLE 2.3 ANALOGUE CAMERA SYSTEMS

Manufacturer	Name of Camera	Type of Objective	Image Angle, $2\tau_{\max}$	Principal Distance, f	Ratio d/f	Maximal Image Distortion
LH Systems	RC 30	UAG-S	90°	153 mm	1:4	4 μm
LH Systems	RC 30	NATS-S	55°	300 mm	1:5.6	4 μm
Z/I Imaging	RMK-TOP 15	Pleogon A3	93°	153 mm	1:4	3 μm
Z/I Imaging	RMK-TOP 30	TOPAR A3	54°	305 mm	1:5.6	3 μm

control orientation of the camera mount by the crab angle and the set overlap percentage by an automatic sensor, which checks the aircraft motion over the ground h/v . The time interval between exposures, t , for a given overlap, q , is calculated by

$$t = \frac{s}{v} = \frac{h}{v} \cdot \frac{a'}{f} \left(1 - \frac{q}{100} \right)$$

in which s is the ground distance between exposures, v the velocity of the aircraft, a' the image size (23 cm) and f the chosen focal length (equal to the principal distance for imaging at infinity).

The major aerial survey camera types in use are contained in Table 2.3, along with their characteristics.

Photogrammetric camera developments had their main roots in Central Europe starting during World War I at Carl Zeiss in Jena, Germany. Aerial cameras were later also produced in Italy, France, Britain, and the United States. The other main producer besides Zeiss became Wild Heerbrugg in Switzerland, which became a major aerial camera producer between the 1930s and the 1970s. Wild became Leica Geosystems in the 1980s. Camera development in Germany after World War II was continued in West Germany by Carl Zeiss Oberkochen since the 1950s and in East Germany since the 1960s by Carl Zeiss Jena.

Now the efforts of Leica and the reunited Zeiss of the 1990s have all been consolidated by the Swedish Investment Company Hexagon after the millennium.

A major competitor has become Vexcel in Austria under the ownership of Microsoft. But also new progressive companies have emerged, such as Visionmap in Israel, IGI in Germany, and Rollei (Trimble) in Germany.

While camera development in the past has been single-sensor oriented, the current tendency is toward integration of sensor systems and a future collaboration of sensors. Oblique imagery, introduced by Pictometry and Multivision as stand-alone systems, may now be provided by inexpensive additional



Figure 2.19 Some manufactured Hexagon cameras. (From Leica Geosystems, Heerbrugg, Switzerland, for Hexagon.)

sensors with a smaller number of pixels than those required for a class A type high-resolution aerial mapping camera.

Sensors of various resolutions may now be accommodated to different platforms:

- Land based (portable on a van or fixed)
- Unmanned aerial vehicle (UAV) platforms
- Airborne
- Space

All types may be assisted by navigational sensors, such as GPS (GNSS) and an inertial measuring unit (IMU).

A few illustrations of the latest Hexagon sensors are added here (Figure 2.19):

1. Z/I (Zeiss/Intergraph) DMC frame camera
2. Leica RDC frame camera
3. Leica ADS Pushbroom scanner
4. Leica ALS Lidar

All of them may be mounted in an aircraft (Figure 2.20).

The characteristics of the Z/I Imaging DMC are shown in Figure 2.21. The DMC comes in three versions:

- DMC 140 with 4×42 Mpixel MS CCDs of $7.2 \mu\text{m}$ size and 1×140 Mpixel pan CCD of $7.2 \mu\text{m}$ size giving an image of 12096×11200 pixels (10 cm GSD at $h = 400 \text{ m}$)



Figure 2.20 Installed Hexagon cameras. (From Leica Geosystems, Heerbrugg, Switzerland, for Hexagon.)

- DMC 230 with 4×42 Mpixel MS CCDs of $7.2 \mu\text{m}$ size and 1×230 Mpixel pan CCD of $5.6 \mu\text{m}$ size giving an image of 15552×14144 pixels (10 cm GSD at $h = 1600$ m)
- DMC 250 with 4×42 Mpixel MS CCDs of $7.2 \mu\text{m}$ size and 1×250 Mpixel pan CCD of $5.6 \mu\text{m}$ size giving an image of 16768×14016 pixels (15 cm GSD at $h = 3000$ m)



Figure 2.21 Z/I Imaging DMC2. (From Leica Geosystems, Heerbrugg, Switzerland, for Hexagon.)



Figure 2.22 Mounting of 5 DMC2 camera parts in frame. (From Leica Geosystems, Heerbrugg, Switzerland, for Hexagon.)

The five DMC camera parts are mounted in one frame (see [Figure 2.22](#)).

The Leica RCD 30 is a coregistered RGB and IR multispectral camera, either with a 50 or 80 mm principal distance. The camera has 2×60 Mpixel CCDs of $6 \mu\text{m}$ size for RGB and NIR with an image size of 8956×6708 pixels (15 cm GSD at $h = 1000$ m).

The Leica Pushbroom Scanner ADS 80 scans perpendicular to the flight line with 24000 pixels in three simultaneous scans:

- Forward in panchromatic
- Nadir in panchromatic and multispectral
- Aft in multispectral or panchromatic (see [Figure 2.23](#))

The Leica ALS 70 laser scanner has a scan rate of 500 KHz for use at a flying height up to 3500 m or 250 KHz up to $h = 5000$ m. Scan patterns may be selected for sine, triangle, or raster scans. The field of view is adjustable up to 75° (full angle). The laser return image operated from aircraft is shown in [Figure 2.24](#).

The scanner can also be operated from a mobile van ([Figure 2.25](#)), with a result shown in [Figure 2.26](#).

Microsoft-Vexcel, Austria, has developed the UltraCam camera. It came on the market as UltraCam D, which subsequently was improved to UltraCam X and UltraCam Xp and finally UltraCam Eagle with 20010 pixels across (see [Figure 2.27](#)). The UltraCam Eagle has an exchangeable lens system with principal distances of either 80 mm or 210 mm ([Figure 2.28](#)).

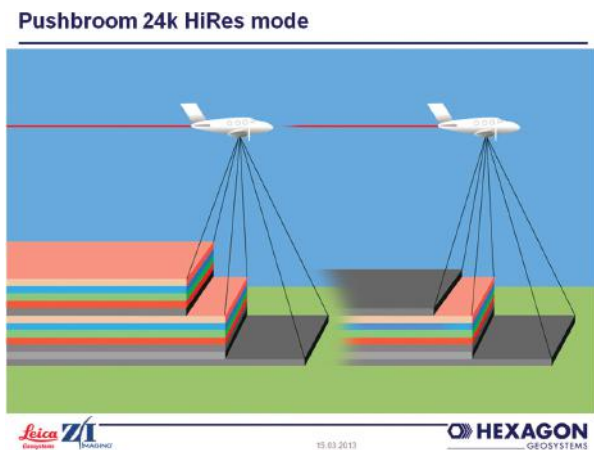


Figure 2.23 Leica Geosystems ADS80 scan. (From Leica Geosystems, Heerbrugg, Switzerland, for Hexagon.)

Processing of UltraCam images is carried out by the UltraMap software to various levels. It starts with the download of the images from the camera into mass storage immediately after the flight, with subsequent offline processing to higher levels, including aerial triangulation, by an efficient Microsoft processing system “Dragon Fly” (Figure 2.29).

It permits the use of multiray photogrammetry, based on 80% longitudinal and 60% lateral overlap, by which up to 12 rays are created for each ground pixel. This helps to avoid occlusions (see Figures 2.30 and 2.31).

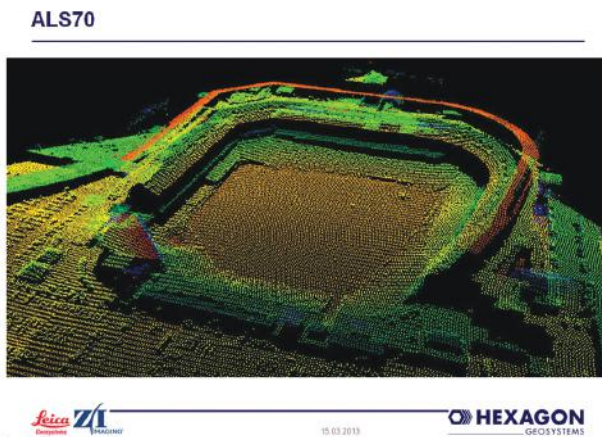


Figure 2.24 Laser image of ALS70. (From Leica Geosystems, Heerbrugg, Switzerland, for Hexagon.)



Figure 2.25 Mobile van operation of ALS70. (From Leica Geosystems, Heerbrugg, Switzerland, for Hexagon.)

This gives the possibility to generate “true orthophotos,” or as Microsoft prefers to call them, “DSM orthophotos” (see [Figure 2.32](#)).

[Figure 2.33](#) is an example of a 10 cm GSD MS image, and [Figure 2.34](#) shows the DSM derived for that image by multiray matching. [Figure 2.35](#) shows such a color-coded DSM for the cathedral area of the City of Graz, Austria.

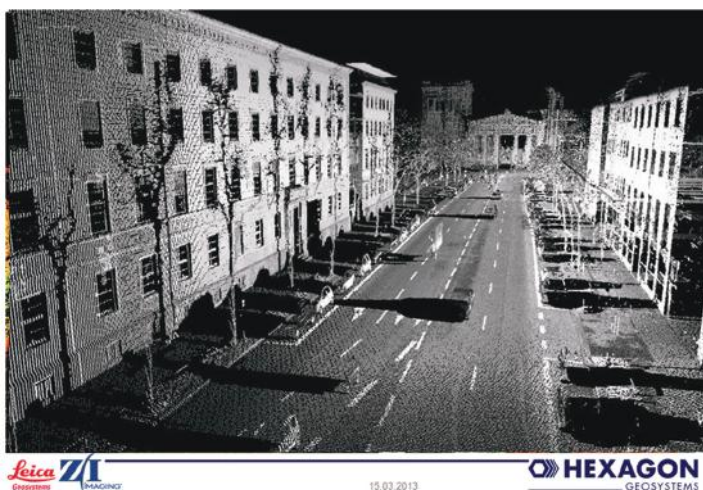


Figure 2.26 Laser image from mobile van. (From Leica Geosystems, Heerbrugg, Switzerland, for Hexagon.)



Figure 2.27 Vexcel UltraCam cameras. (From Microsoft-Vexcel, Graz, Austria.)

Image Quality of Aerial Survey Cameras

Image quality in photographic images is determined by the contrast between two image objects with the irradiances E_0 and E_N or its reflection coefficients ρ_o and ρ_N . The object contrast is therefore:

$$K = \frac{E_N}{E_0} = \frac{\rho_N}{\rho_o}$$



Figure 2.28 UltraCam Eagle. (From Microsoft-Vexcel, Graz, Austria.)

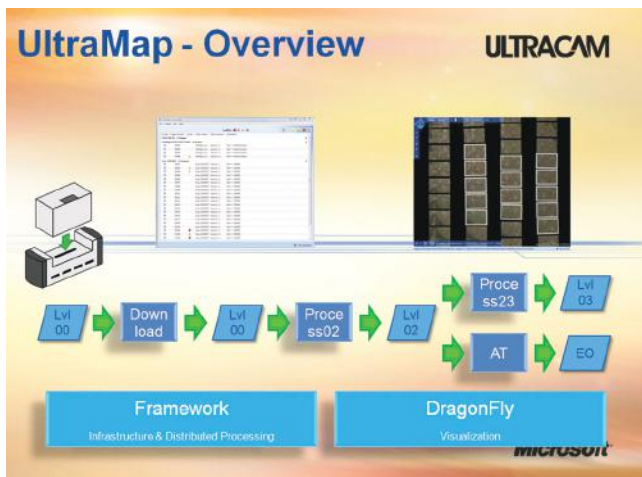


Figure 2.29 UltraMap Processing System. (From Microsoft-Vexcel, Graz, Austria.)

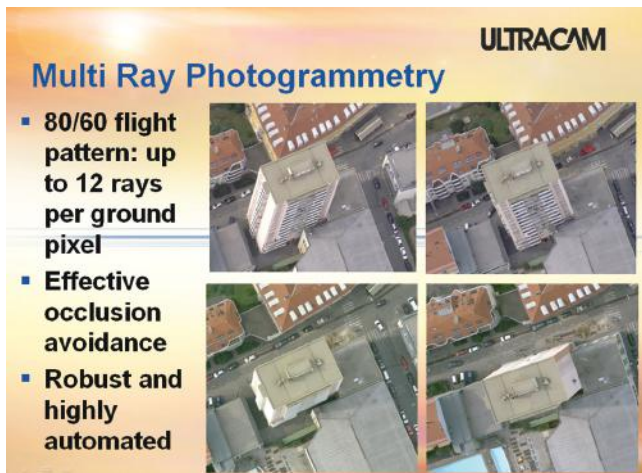


Figure 2.30 Multi Ray photogrammetry. (From Microsoft-Vexcel, Graz, Austria.)



Figure 2.31 Overlapping frames. (From Microsoft-Vexcel, Graz, Austria.)

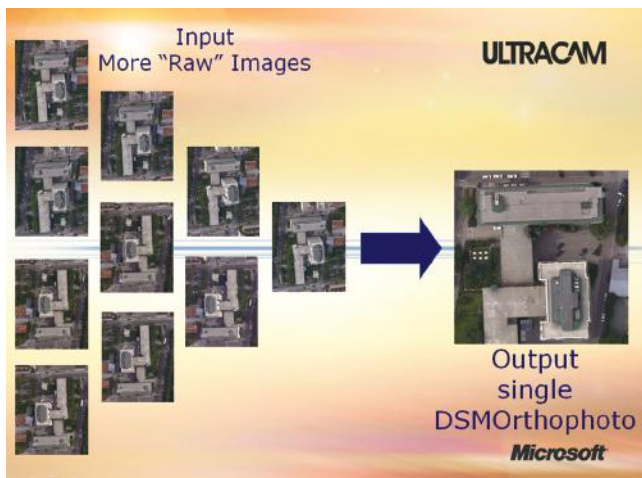


Figure 2.32 DSM orthophotos. (From Microsoft-Vexcel, Graz, Austria.)



Figure 2.33 10 cm GSD UltraCam image. (From Microsoft-Vexcel, Graz, Austria.)



Figure 2.34 DSM derived. (From Microsoft-Vexcel, Graz, Austria.)

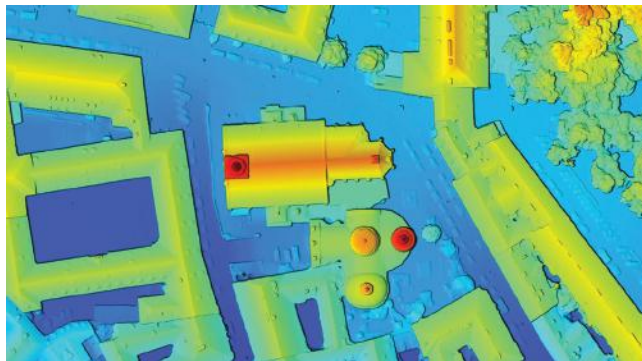


Figure 2.35 Color-coded DSM of Graz, Austria. (From Microsoft-Vexcel, Graz, Austria.)

Modulation is defined by:

$$M = \frac{\rho_N - \rho_o}{\rho_N + \rho_o} = \frac{K-1}{K+1}$$

This object contrast or the corresponding object modulation is visible in the image as image contrast K' or as image modulation M' depending on the transparencies τ_o and τ_N of the imaged object contrast

$$K' = \frac{\tau_N}{\tau_o}$$

and

$$M' = \frac{\tau_N - \tau_o}{\tau_N + \tau_o} = \frac{K'-1}{K'+1} = \frac{10^{\Delta D} - 1}{10^{\Delta D} + 1}$$

with

$$\Delta D = \log \frac{\tau_N}{\tau_o}$$

the contrast density difference and modulation can therefore be converted into corresponding values shown in **Table 2.4**.

TABLE 2.4 CONTRAST, DENSITY DIFFERENCE, AND MODULATION

Contrast	1000:1	2:1	1.6:1
Density difference	3.0	0.3	0.2
Modulation	0.999	0.33	0.23

The contrast transfer, C' , and the modulation transfer, C , through the imaging system is therefore:

$$C' = \frac{K'}{K} \quad \text{and} \quad C = \frac{M'}{M}$$

Both C' and C are functions of the spatial distance, expressed in terms of a spatial frequency v . This is shown in Figure 2.36 for the frequency dependent modulation transfer function.

Image quality in a combined optical-photographic system is deteriorated by the imaging process if the modulation transfer function, C , is < 1 . Only for an extremely high contrast (1000:1) does C become nearly 1.

Image quality in a photographic system, other than by contrast, is influenced by the following components:

- Optical system
- Film
- Image motion during exposure

Each component is characterized by its own modulation transfer function, C_{optics} , C_{film} , $C_{\text{image motion}}$. The total effect is C_{total} :

$$C_{\text{total}} = C_{\text{optics}} \cdot C_{\text{film}} \cdot C_{\text{image motion}}$$

The typical components for an aerial camera system are shown in Figure 2.37.

The resolution of an optical system is first limited by diffraction. The resolution A in line pairs per millimeter (lp/mm) can be expressed by

$$A = \frac{1000 \cdot d}{24 \cdot \lambda \cdot f}$$

in which d is the diameter of the diaphragm, λ the wavelength, and f the focal length. For a d/f value of 4, this amounts to 120 lp/mm. Other limiting effects stem from the composition of the lens system causing lower actual resolution.

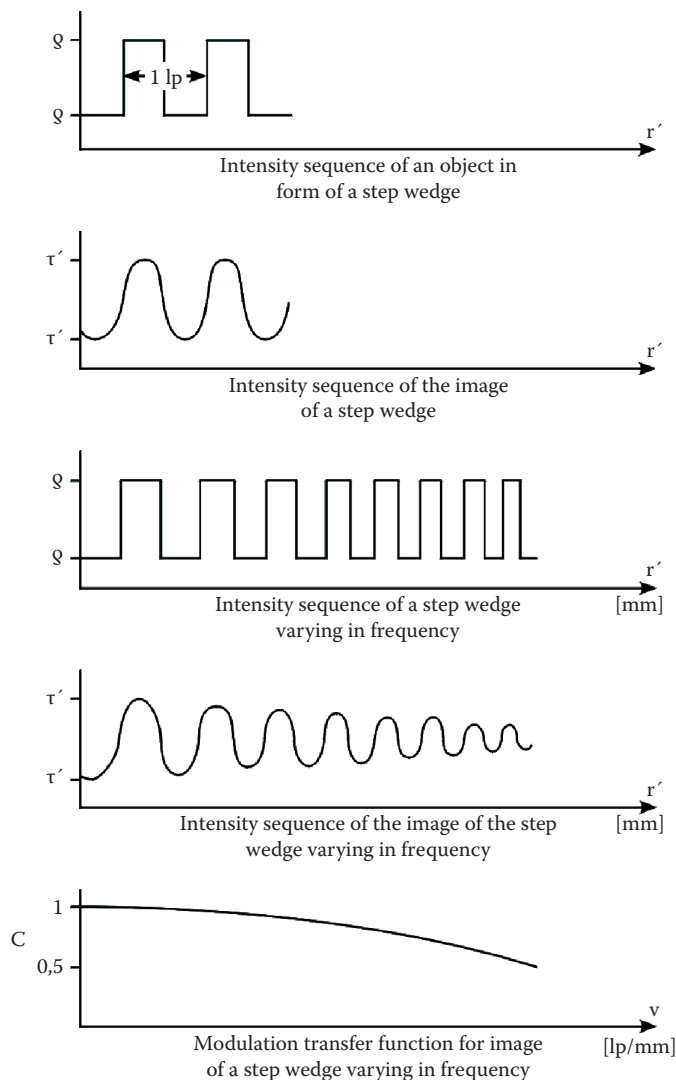


Figure 2.36 Modulation transfer function.

The photographic film resolution depends on its grain size. High sensitive film contains coarse silver halide particles with a resulting low resolution. Low sensitive film has small grain size of the particles resulting in high resolution. The resolution of typical aerial films is shown in [Table 2.5](#).

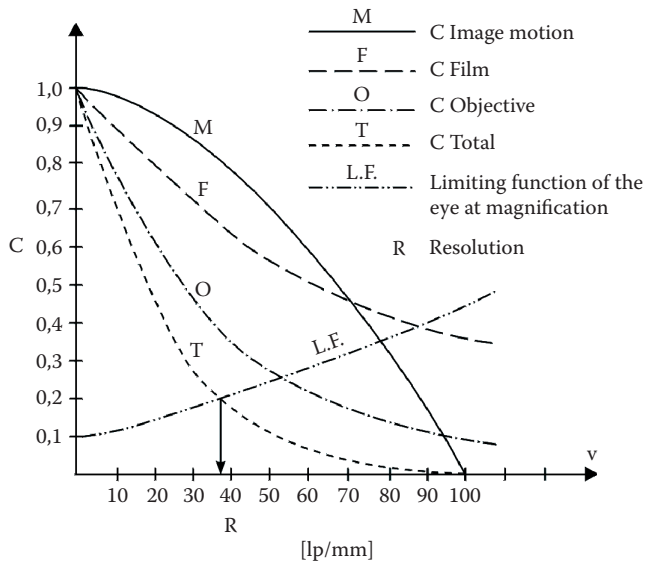


Figure 2.37 Modulation transfer function components for an aerial photographic system.

Image motion $\Delta a'$ in micrometers during exposure depends on the exposure time, Δt , on the platform movement over the ground (v) in kilometers per hour, the focal length (f), and the flight altitude (h):

$$\Delta a' = \frac{f}{h} \cdot \frac{\Delta t}{3600} \cdot v$$

Under the assumption that the modulation assumes a value of 0 at a value of

$$a' = \frac{1000}{\Delta a'}$$

in line pairs per millimeter, the modulation transfer function due to image motion becomes:

$$C_{\text{image motion}} = \cos\left(\frac{v}{2a'}\right)$$

The human eye determines a limiting function for which contrasts can still be recognized at low modulation. Intersecting this limiting function with C_{total} yields the interpretable resolution in line pairs per millimeter.

TABLE 2.5 AERIAL SURVEY FILMS

Manufacturer	Name	Sensitivity	Resolution of Contrast 1000:1	Resolution at Contrast 1.6:1	Type
Agfa	Aviphot pan 200 SPE1	125–200 C1 ISO (23 DIN)	130 lp/mm	50 lp/mm	Panchromatic
Agfa	Aviphot pan 80	64–100 ISO (20 DIN)	287 lp/mm	101 lp/mm	Panchromatic
Agfa	Aviphot color X100 PE	125–160 ISO (22 DIN)	140 lp/mm	55 lp/mm	Color negative
Agfa	Aviphot color N400 PE	400–640 ISO (28 DIN)	130 lp/mm	35 lp/mm	Color negative
Agfa	Aviphot chrome 200 PE1/PE3	200 C ISO (24 DIN)	110 lp/mm	50 lp/mm	Color reversal
Kodak	Aerographic 2402	160 ISO (23 DIN)	130 lp/mm	55 lp/mm	Panchromatic
Kodak	Aerographic 2403	640 ISO (29 DIN)	100 lp/mm	40 lp/mm	Panchromatic
Kodak	Double X Aerographic 2405	400 ISO (27 DIN)	125 lp/mm	50 lp/mm	Panchromatic
Kodak	Panatomic X3412	40 ISO (17 DIN)	400 lp/mm	125 lp/mm	Panchromatic
Kodak	Aerocolor 2445	64 ISO (19 DIN)	80 lp/mm	40 lp/mm	Color negative
Kodak	Aerochrome 2448	32 ISO (16 DIN)	80 lp/mm	40 lp/mm	Color reversal
Kodak	Aerocolor SO 846	160 ISO (23 DIN)	100 lp/mm	63 lp/mm	Color negative

The atmosphere generally diminishes the object contrast for all objects sensed by aerial imaging. If two objects consisting of sand with a reflection coefficient $\rho_{\text{sand}} = 30$ and coniferous forest with a reflection coefficient $\rho_{\text{forest}} = 1$ are observed, the object contrast, K , may be expressed as:

$$\frac{\rho_{\text{sand}}}{\rho_{\text{forest}}} = \frac{30}{1} = 30 = K$$

The image contrast is then affected by the diffused atmospheric light of 3%.

Thus:

$$K' = \frac{30+3}{1+3} = \frac{33}{4} = 8 = K'$$

This illustrates that resolutions of generally low-contrast aerial photographs should not be compared at a contrast of 1000:1, but at a contrast of 1.6:1, for which the modulation of 1 diminishes to 0.23. Thus, the modulation transfer function, as shown in [Figure 2.38](#), is flattened, and its intersection with the limiting function of the eye is lowered in resolution.

Aerial survey camera systems with image motion compensation are, in practice, achieving a resolution of between 40 to 50 lp/mm for black-and-white images and of between 30 and 40 lp/mm for color images.

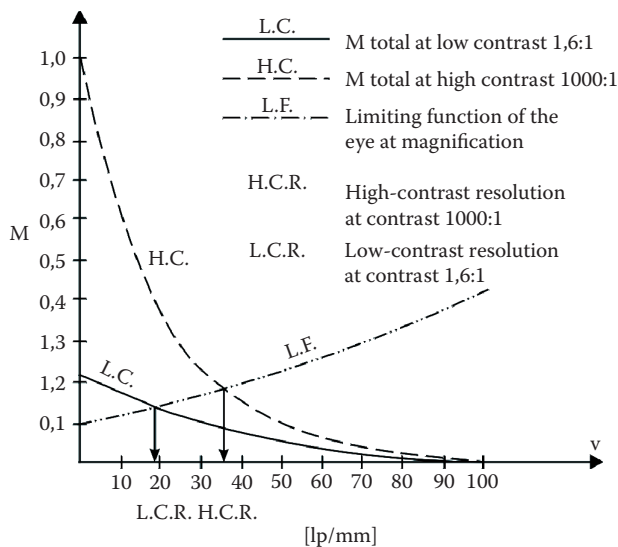


Figure 2.38 Resolution at low contrast.

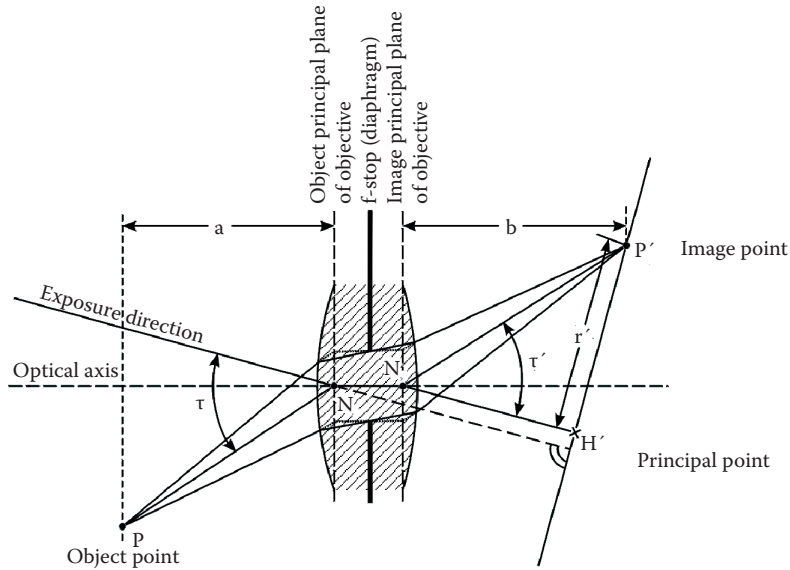


Figure 2.39 Imaging through an objective.

Another property of aerial survey cameras is the ability to generate photographic images with minimum geometric distortion. A primary source of geometric distortion stems from the objective (Figure 2.39).

Radial distortion, $\Delta\tau$, is the angular difference between the angle of exposure direction and object direction, τ_i , and their imaged difference τ'_i :

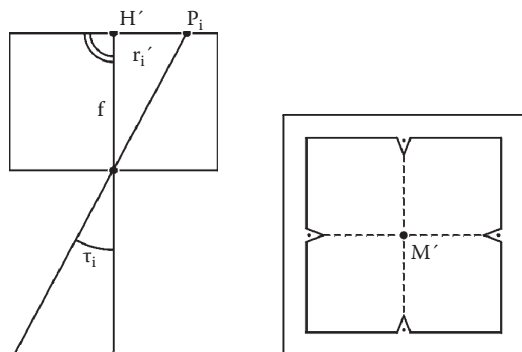
$$\Delta\tau_i = \tau_i - \tau'_i$$

Distortion can also be expressed as a radial distance difference in the image plane

$$\Delta'_r = r_i - r'_i$$

with r'_i measured from the principal point, determinable from the fiducial marks of the camera and $r_i = f \cdot \tan \tau_i$ (see Figures 2.40 and 2.41). N marks the entrance of exit modes of rays along the optical axis through the objective.

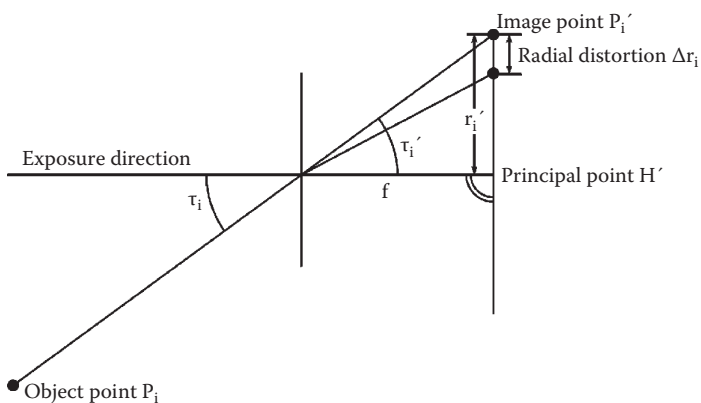
Camera manufacturers have tried to minimize the distortion in a factory calibration procedure in which the angles τ'_i are measured through the objective by a goniometer. The fiducial marks of the camera, determining the principal point, are fixed so that a minimum radial and tangential distortion results.

**Figure 2.40** Principal point.

Camera manufacturers issue calibration certificates in which the attained radial distortions are listed. They are in the order of $2 \mu\text{m}$ and usually never exceed $4 \mu\text{m}$ in the image plane. Tangential lens distortions are generally only one-third of the radial distortions and thus negligible for factory calibrations (see Figure 2.42).

A second source of distortion is the film. If the pressure plate vacuum has properly worked, the image plane can be considered as flat. Otherwise distortions of

$$\Delta r'_i = \frac{r'}{f} \Delta f = \Delta f \cdot \operatorname{tg} \tau'$$

**Figure 2.41** Definition of radial distortion.

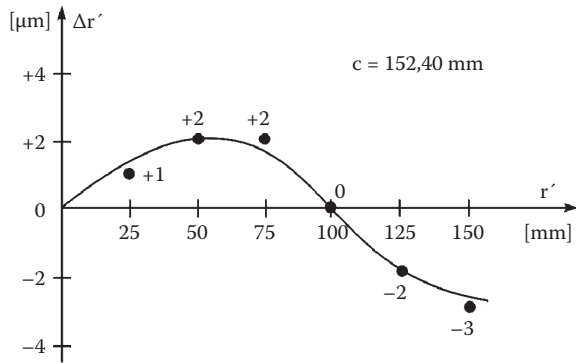


Figure 2.42 Radial distortion of a photogrammetric objective.

will result. Δf is the deviation of the image point on the film from the ideal focal plane at the principal distance f .

More serious are the geometric distortions of the film caused by the wet developing and drying process. For this reason, each camera contains between four to eight fiducial marks. If their images are measured, a correction of the film deformations in the direction of the film and perpendicular to it can be made during the restitution. Fortunately, these types of film deformations remain constant for the entire film, so that they can be accounted for by parameters in the restitution process.

Optomechanical Scanners

An optomechanical scanner contains a single sensor element, which permits the recording of the irradiance of a ground pixel. A rotating mirror scans the terrain, so that a whole line of ground pixels can be recorded in a time sequence. The next scan of a forward-moving platform records the adjacent line of ground pixels. Thus, the scanning mechanism during forward motion permits a recording of a whole image. The scanning principle is shown in [Figure 2.43](#).

For an altitude, h , a field of view of the scanned pixel, ω , the total angular scan width, Ω , and the scan angle from the vertical, α , the ground pixel size, a , in the scan direction becomes:

$$a = \frac{\omega \cdot h}{\cos^2 \alpha}$$

The ground pixel size, b , in the line of flight, b , is likewise:

$$b = \frac{\omega \cdot h}{\cos^2 \alpha}$$

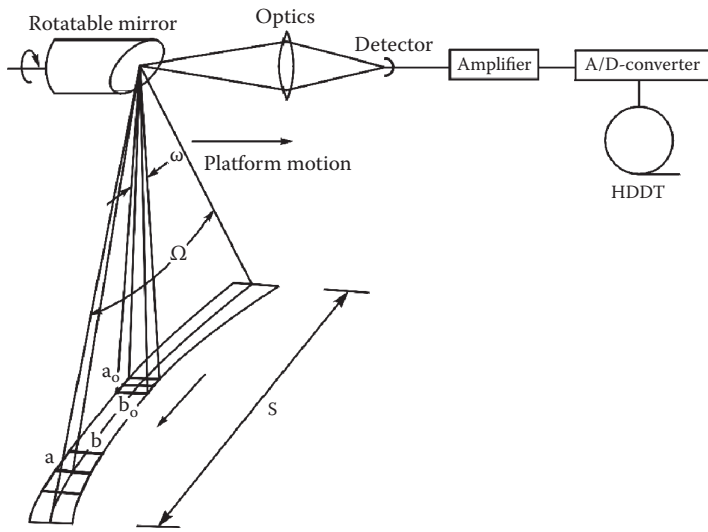


Figure 2.43 Operation of an optomechanical scanner.

The swath of the scan, s , becomes:

$$s = 2h \cdot \operatorname{tg} \frac{\Omega}{2}$$

The scan frequency, v , is a function of the platform velocity, v_g :

$$v = \frac{v_g}{\omega \cdot h}$$

Optomechanical scanners have been utilized for airborne and for satellite multispectral scanners, as shown in [Figure 2.44](#).

Instead of a single photodiode, a linear array was used as a sensor. The spectral separation of the incoming energy was achieved by the diffraction of a prism in the optical path, so that different bands of wavelengths could be recorded at the array at a particular time.

The scanner even permitted the recording of thermal energy with the use of a dichroitic separation of the ray. Thermal energy could then be collected on a thermally cooled (77 or 5 K) far-infrared sensitive mercury-doped CD-telluride or germanium detector.

The characteristics of such detectors are shown in [Table 2.6](#).

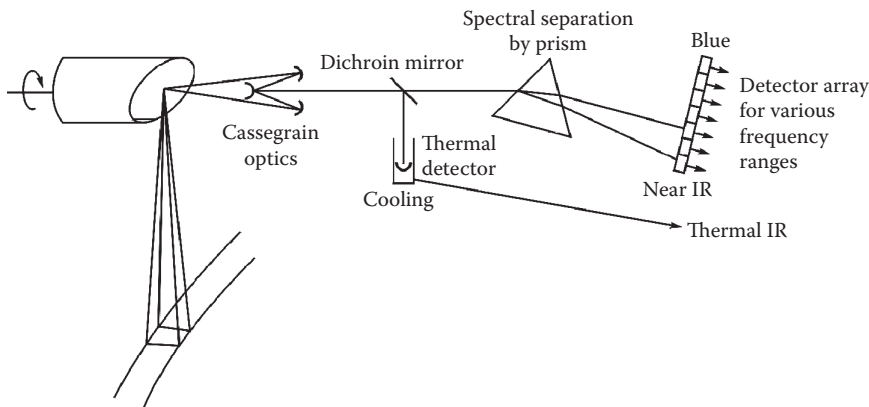


Figure 2.44 Operation of a multispectral scanner.

Laser Scanners

It is possible to direct laser light impulses to the terrain along the principles of electromechanical scanning. Part of the reflected radiation returns to the laser scanner. This gives the possibility for measuring the time between the emission of the pulse and the first and the last return, as well as the energy received.

This permits the use of the device as a laser altimeter for any spot reached by the laser pulse. If the position of the sensor is measured by in-flight GPS, and its orientation by inertial navigation devices, then it becomes possible to determine the three-dimensional position of the reflection point.

On this principle, laser scanners, such as the system operated by Toposys, have been built and operated: it is a pulsed fiber scanner, operated at an air-borne altitude of less than 1600 m with a laser wavelength of 1.55 μm . It emits pulses every 5 nsec. The scan frequency is 650 Hz and the pulse repetition rate is 83000 Hz. This permits, within a field of view of 7° from the vertical, the measurement of laser reflection points of a density of three points per square meter on the surface.

TABLE 2.6 OPTOMECHANICAL DETECTORS

Scanner	Platform	ω	Ω	Number of Visual and Near IR Channels	Number of Thermal Channels
Daedalus DS 1200	Aircraft	2.5 mrad	77°	2	1
Landsat MSS	Satellite	0.087 mrad	11.6°	4	0
Landsat TM	Satellite	0.024 mrad	11.6°	6	1

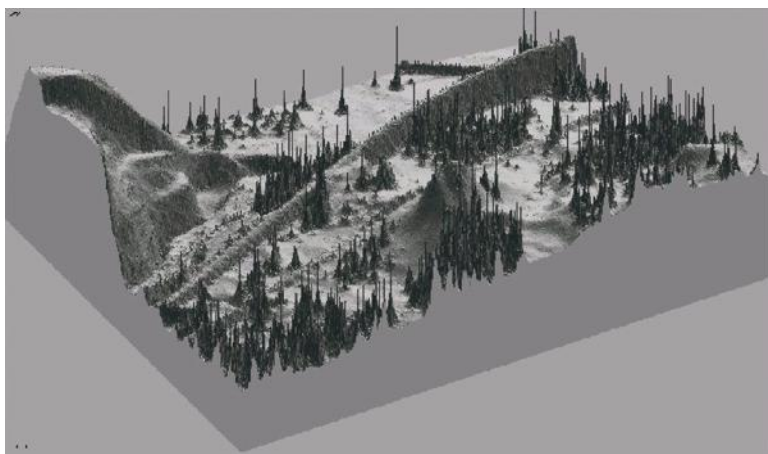


Figure 2.45 Original laser scan. (Courtesy of the Institute for Photogrammetry and GeoInformation, University of Hannover, Germany.)

The recording of the first and last pulse received from the point permits the judging of the thickness of the vegetation cover of the terrain. The swath covered in a flight strip is then up to 390 m, and elevation measurements are possible within a relative accuracy of 2 cm and an absolute accuracy of 15 cm for a digital elevation model. Leica-Helava Systems produces a laser scanner ALS 40 for the generation of digital elevation models. Figures 2.45 and 2.46 show the laser signals received in original and filtered forms.

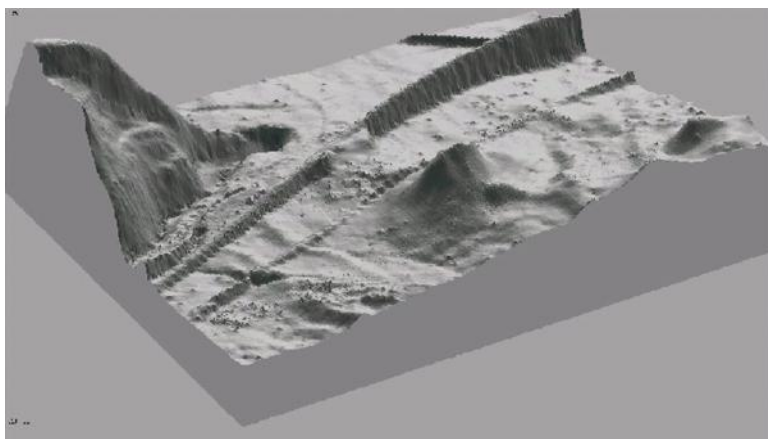


Figure 2.46 Filtered laser scan. (Courtesy of the Institute for Photogrammetry and GeoInformation, University of Hannover, Germany.)

It is possible to use the intensity of the received signal to construct an image with respect to the digital elevation model, even though this use of the laser scanner is still experimental (see www.toposys.com and www.geolas.com).

Optoelectronic Scanners

Optoelectronic imaging is possible when an image created through an optical system is created on a linear or a matrix array of CCD sensors. Linear arrays of sufficient length are easier to assemble than matrix arrays. Therefore, the electrooptical scanner, as shown in [Figure 2.47](#), has frequently been applied in satellite sensors using the push-broom principle.

A push-broom scanner has the linear array oriented perpendicular to the platform motion. A detector element of the dimension a' perpendicular to the flight direction will cover a ground pixel dimension, a , according to

$$a = \frac{h}{f} \cdot a'$$

with h being the platform altitude and f the focal length of the optics. In-flight direction, the detector element of the dimension b' in this direction, is likewise imaged at a ground pixel dimension, b :

$$b = \frac{f}{h} \cdot b'$$

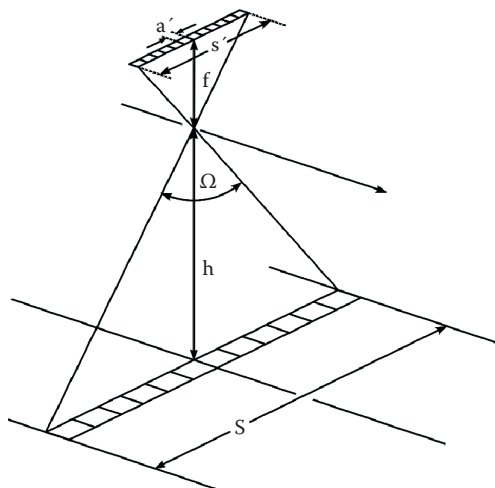


Figure 2.47 Optoelectronic scanner.

TABLE 2.7 PARAMETERS OF THE SPOT ELECTROOPTICAL SCANNER

Name	ω	Ω	Number of Channels	Type
SPOT-P	0.012 mrad	4.2°	1	Panchromatic
SPOT.XS	0.024 mrad	4.2°	3	Multispectral

To assemble an image, the exposure, Δt , must be chosen proportional to the velocity of the platform with respect to the ground, v_g :

$$b = v_g \cdot \Delta t$$

The swath of the push-broom sensor, s , becomes

$$s = \frac{h}{f} \cdot s' = 2h \cdot \tan \frac{\Omega}{2}$$

with s' being the length of the linear array pointing symmetrically to the vertical. An example is the sensor for the French Spot satellite, characterized in Table 2.7.

The Spot satellite sensor not only uses a panchromatic array with 10 m ground pixels but, in parallel to that, three farther arrays of half resolution, yielding 20 m ground pixels for the filtered spectral bands of green, red, and near infrared.

One Spot satellite sensor may be inclined sideways in a programmed mode in steps from -27° to +27° to cover any point on earth, subject to cloud cover permitting it, in 5 days. Three operating Spot satellites can do so in 1 day.

Digital electrooptical cameras have also been constructed by the DLR for use on Mars. After a Russian spacecraft failed on launch, the DLR constructed an aircraft version of that camera. Its design has been manufactured by the Leica-Helava Systems Company for aerial surveys as the ADS 40 airborne digital sensor (www.lhsystems.com) (see Figure 2.48). A raw and a rectified image of that sensor are shown in Figures 2.49 and 2.50.

The digital sensor of the Zeiss-Intergraph Imaging Company, the digital modular camera (DMC), has split objectives imaging onto matrix sensors of seven image planes (Figures 2.51 and 2.52). The images are resampled and reconstructed in a single frame by software (www.ziimaging.com).

The realization of a stereo electrooptical scanner is due to O. Hofmann at MBB. It was built for use in the space shuttle and MIR for the MOMS 02 and MOMS 02-P satellite missions (Figure 2.53).

The MOMS 02 sensor possesses a vertical CCD line with 5 to 6 m ground pixel and two forward- and aft-looking CCD arrays with 15 to 18 m pixels in the same image plane in the panchromatic range. Parallel to the vertically looking panchromatic CCD, there are three additional filtered multispectral arrays at 15 to 18 m ground pixels.



Figure 2.48 The LH Systems ADS 40 digital camera. (Courtesy of LH Systems [Leica Geosystems], San Diego, California. © Leica Geosystems, 2000.)

For stereo sensing, only the vertical panchromatic and the two forward- and aft-looking CCD lines are used. Further developments of this principle have been introduced in the Spot 5 satellite of 2002 yielding a ground pixel of 2.5 m, paired with an equivalent array oriented at a fixed angle.

Image Spectrometers

It is possible to design an optoelectronic scanner with an optoelectronic array of photosensitive elements in conjunction with diffractive gratings in such a manner that, in combination with a continuous variable optical filter, narrow bands of only 10 nm wavelength are projected onto the array resulting in continuous spectral signatures in the visible and infrared spectrum. These so-called hyperspectral devices have the ability to image in up to 224 spectral channels, which can be compared with object libraries. The spatial resolution of these hyperspectral devices has, of course, to be reduced in accordance with the reflected energy available. For the AVNIR, which operates in 60 visible and near-infrared bands at wavelengths between 430 and 1012 nm in 10 nm increments, a ground sample distance of 0.8 m can be reached from an altitude of 1600 m. The AVIRIS spectrometer of NASA-JPL is operated from high-altitude aircraft ($h = 20$ km). It has 224 spectral channels at intervals of 10 nm between 400 nm and 2450 nm wavelength. Its ground pixel size at that altitude is 17 m and the swath 11 km (<http://aviris.jpl.nasa.gov/>).



Figure 2.49 Raw ADS 40 image. (Courtesy of LH Systems [Leica Geosystems], San Diego, California. © Leica Geosystems, 2000.)

NASA has launched a TRW-built 200 channel image spectrometer Hyperion on the EO-1 spacecraft in the year 2000, with 30 m ground pixels at a swath of 7.5 km.

Oblique Imaging

The availability of lower-cost digital camera technology has generated the interest to design new multiple cameras systems, by which not only vertical imagery is acquired, but also oblique images from front and aft and left and right camera orientations.

Oblivision and Multivision designed in Israel; and Pictometry, an oblique system in the United States, are such examples. Pictometry was widely used for Homeland Security activities.



Figure 2.50 Rectified ADS 40 image. (Courtesy of LH Systems [Leica Geosystems], San Diego, California. © Leica Geosystems, 2000.)

More recently, camera manufacturers, such as Leica Geosystems, Microsoft Vexcel, and ISI in Germany have also put such multicamera systems on the market. These can effectively be used not only for the creation of digital city models, but the oblique images also permit the viewing of image details of the façades of houses.

Radar Imaging

The natural radiation in the microwave range of the electromagnetic spectrum is generally too weak to be useful for imaging. Therefore, passive sensing is rare. Radar imaging, therefore, utilizes an active sensor, generating the transmitted and reflected energy in the microwave region.



Figure 2.51 The Z/I DMC digital camera. (Courtesy of Z/I Imaging Corporation, Huntsville, Alabama.)

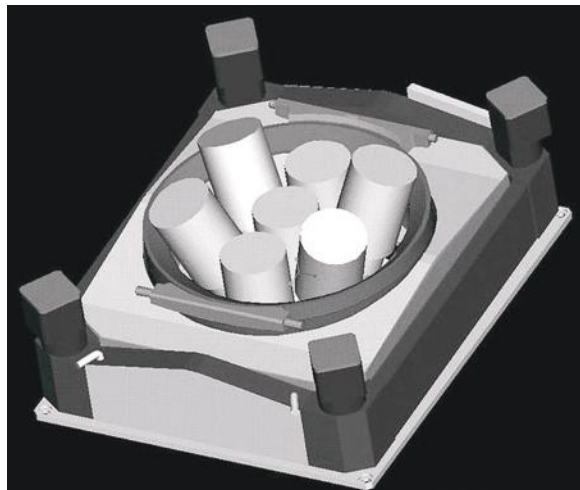


Figure 2.52 The Z/I DMC split objectives. (Courtesy of Z/I Imaging Corporation, Huntsville, Alabama.)

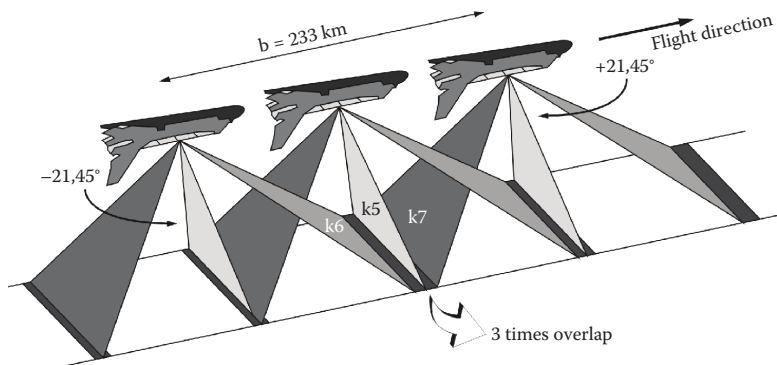


Figure 2.53 MOMS stereo scanner.

Radar systems have principally been built in three wavelength regions:

- X band, $\lambda = 2.4$ to 3.8 cm (8000 to 12500 MHz)
- C band, $\lambda = 3.8$ to 7.5 cm (4000 to 8000 MHz)
- L band, $\lambda = 15$ to 30 cm (1000 to 2000 MHz)

The X band and the C band in particular have the advantage of cloud penetration. They can therefore operate day and night in an all-weather system.

Let us now look at the simple operating principle of a radar. A transmitter generates a radar pulse composed of a wave signal in the respective band. The duration of the radar pulse is Δt . It is transmitted through an antenna with special propagation characteristics, so that the energy is concentrated in a narrow beam perpendicular to the platform motion. It reaches the ground with the speed of propagation of electromagnetic waves, v ,

$$v = \frac{c}{n}$$

with c being the velocity in vacuum and n the propagation coefficient.

At the terrain, the energy is directionally reflected, scattered, or absorbed. The reflected energy retroreflected into the direction of the transmitting antenna is characterized by the radar equation for the radiant flux received

$$\phi = \frac{\phi_o \cdot G^2 \cdot \lambda^2 \cdot \rho_o \cdot A}{(4\pi)^3 \cdot r^4} \cdot 10^{-0.2\alpha r}$$

with the following quantities:

ϕ_o = transmitted radial flux from the antenna in W

G = antenna gain along the direction of transmission

ρ_o = retroreflection or backscattering coefficient of the terrain point

A = reflecting surface in square meters

r_i = distance between antenna and object i

α = coefficient of atmospheric attenuation, which is wavelength λ dependent

The transmitted and backscattered radar pulse of different terrain points along the plane of transmission reaches the antenna at different times, T_i :

$$T_i = \frac{2r_i}{v}$$

The achievable ground resolution of a radar system in the direction perpendicular to the platform motion, a , depends on the duration of the pulse, Δt , and the depression angle, β , between the horizon and the transmitted and reflected ray:

$$a = \frac{v \cdot \Delta t}{2 \cdot \cos\beta}$$

For the reception of the backscattered energy, the antenna is switched by a duplexer from transmission to reception. This permits the recording of the incoming signals as a function of T_i . When the reception from all the terrain points in the plane is completed, the antenna is again switched to the transmitter and a new pulse is sent while the platform has moved forward.

The resolution in the direction of forward motion, b , like for scanners, depends on the platform velocity, v_g , and the time interval, ΔT , between successive pulse transmissions:

$$b = v_g \cdot \Delta T$$

However, since it is difficult to bundle the transmitted energy in one plane, the time interval, ΔT , at which two successive pulses may be transmitted, equally depends on the antenna characteristics. The azimuthal dimension Θ° of a radar beam in the transmission plane depends on the length, L , in meters of the transmitting antenna, for which the following relation is valid:

$$\Theta^\circ = 60 \cdot \frac{\lambda}{L} \quad \text{and} \quad b = r \cdot \Theta^\circ = \frac{h}{\sin\beta} \cdot \Theta^\circ$$

This limits the azimuthal resolution of a side-looking airborne radar (SLAR), since the length of an antenna depends on the length of a platform (e.g., an airplane). Radar imaging is illustrated in [Figure 2.54](#).

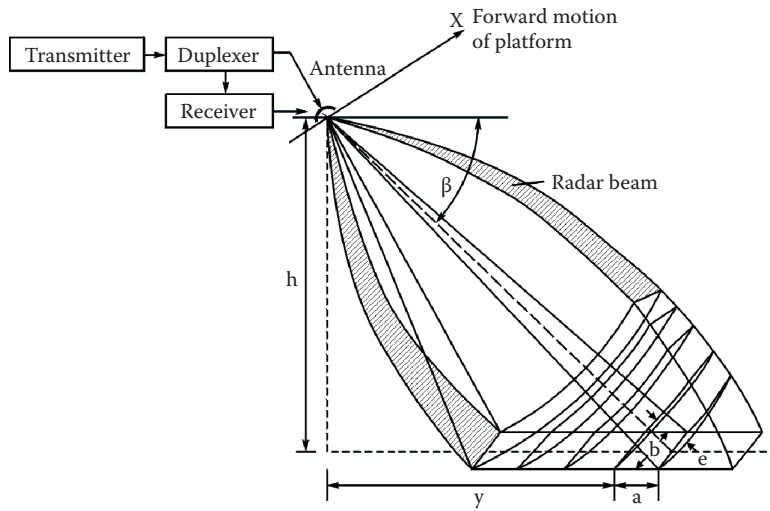


Figure 2.54 Radar imaging.

There is a better possibility to improve the azimuthal resolution with small antennas, which radiate the energy in a wide beam. Since the radar pulse emits a wave at a known frequency, the coherent energy from the reflected target not only permits the user to determine its intensity but also to use its frequency information. A target's position along the flight determines the Doppler frequency of its backscatter. Targets ahead of the aircraft produce a positive Doppler offset; those behind the aircraft produce a negative Doppler frequency.

Thus, the signal may be geometrically focused to a Doppler frequency of zero. This is analogous to a holographic reconstruction of the wave signals to form an image. The image coordinate in azimuthal direction can be generated as a slant range distance, y'_s ,

$$y'_s = \frac{v \cdot T}{2} \cdot m_y = m_y \cdot r_s$$

in which v is the velocity of wave propagation, T is the time interval between emission and reception, and m_y is a scale factor. r_s is the slant range.

The slant range distance, y'_s , can be reduced to a ground range distance, y'_G , for a specified platform elevation, h :

$$y'_G = m_y \cdot \sqrt{r_s^2 - h^2}$$

The image coordinate in flight direction is:

$$x' = m_x \cdot x$$

The scale factor, m_x , is a function of the platform velocity, v_g .

Height differences of the terrain, Δh , cause slant range differences, Δr , or their horizontal projection, Δy . According to [Figure 2.55](#):

$$\Delta r = \sqrt{y^2 + (h - \Delta h)^2}$$

or

$$\Delta y = \sqrt{y^2 - 2\Delta h h + \Delta h^2}$$

Polarization of a Radar Beam

Most side-looking airborne radar (SLAR) or synthetic aperture radar (SAR) systems have antennas emitting the radar pulses in a polarization plane. Most frequently, the horizontal polarization, H , is chosen, but it is also possible to use a vertical polarization, V .

Due to the fact that radar backscattering objects may depolarize the reflected signal in all directions, it becomes possible to receive the radar backscatter in either the horizontal or the vertical polarization plane. The following combinations are therefore possible: HH , HV , VV , or VH , of which generally only three polarization returns are independent, since $HV \approx HV$. Multipolarization therefore adds another dimension to radar remote sensing.

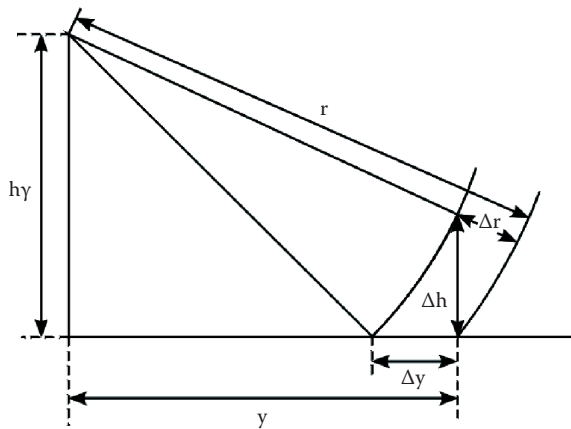


Figure 2.55 Height displacements in the radar image.

Radar Interferometry

Radar pulses are transmitted as coherent waves, and they are reflected as such. If the returning waves are received by two spatially separated antennas, then the two wave signals may be compared with respect to the phase difference by means of interferometry.

The interferometric principle is shown in [Figure 2.56](#). The axis of the interferometer perpendicular to the base, b , yields signal differences with a phase difference of zero. At an angle to that axis, phase differences will be observed that are proportional to an angle in relation to the base and half the wavelength. This permits the location of the surface in terms of a digital elevation model.

If the phase arriving at antenna 1 (transmission and reception) is

$$\phi_1 = -\frac{4\pi}{\lambda} \cdot r$$

and the phase arriving at antenna 2 (reception only) is

$$\phi_2 = -\frac{4\pi}{\lambda} (r + \Delta r)$$

then the phase difference to be observed is

$$\Delta\phi = \phi_1 - \phi_2 = \frac{4\pi}{\lambda} \Delta r$$

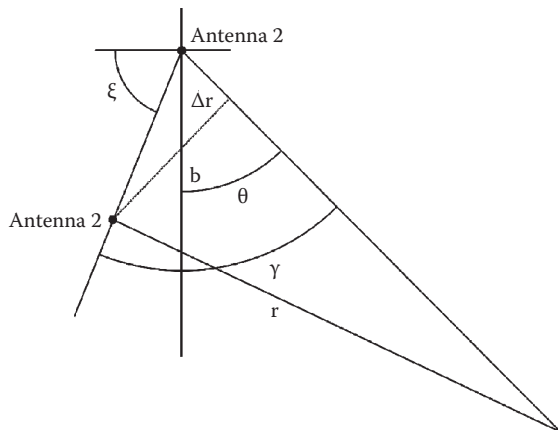


Figure 2.56 Radar interferometry.

Introducing the base, b , between the antennas, and the angles, ξ , between horizon and base as well as the angle, θ , between the point of the reflection and the vertical, one obtains

$$(r + \Delta r)^2 = r^2 + b^2 - 2rb \cos \gamma$$

with $\gamma = 90^\circ - \xi + \theta$

Thus:

$$\Delta r = \sqrt{r^2 + b^2 + 2rb \sin(\theta - \xi)} - r^2 \approx b \sin(\theta - \xi)$$

The distance, y , from the flight axis, where a phase difference of 0 occurs is $y = r \sin \theta$. The next 0 phase difference occurs at location $y = r \sin(\theta - \xi)$. The phase differences can be made visible in the form of interferometric fringes.

[Figure 2.57](#) shows an ERS radar image for the German island of Rügen. [Figure 2.58](#) shows the generated interferometric fringes for two radar images. [Figure 2.59](#) shows the derived digital elevation model for the area of Hannover derived from two subsequent ERS images.

For airborne radars, a second antenna may easily be accommodated on the aircraft. For satellites this is more difficult. During the Shuttle Radar Topographic Mission (SRTM) flown by NASA and the German DLR on the space shuttle, the second reception antenna was placed on a 60 m long beam extended from the shuttle during the radar-mapping mission. The spatial position of the two antennas and the length of the base were determined by GPS receivers.

It is also possible to create interferograms from radar signals of two different satellites, as was done during the European Space Agency's ERS1/ERS2 Tandem Mission, in which the second satellite, ERS2, followed the first, ERS1, one day later in the same orbit. On the assumption that orbital differences created a small base of between 100 to 300 m, and that the radar reflection properties have not changed during one day, interferometry became possible. ERS1 and ERS2, however, did not have precise orbital data, so that the length and the orientation of the base had to be estimated. This made the interferometric fringes ambiguous, and a restitution of the interferogram into digital elevation models required a trial and error "phase unwrapping" procedure.

For interferograms produced from the ERS 1/2 Tandem Mission, the agreement with a precise digital elevation model was within 5 m in open flat areas, although it was considerably less in forested areas, and it reached 100 m in mountain areas due to radar shadows and foreshortening.

The TerraSAR-X satellite of DLR, Germany-Astrium and the Italian-French COSMO-Skymed radar satellite succeeded to provide imagery up to 1 m GSD

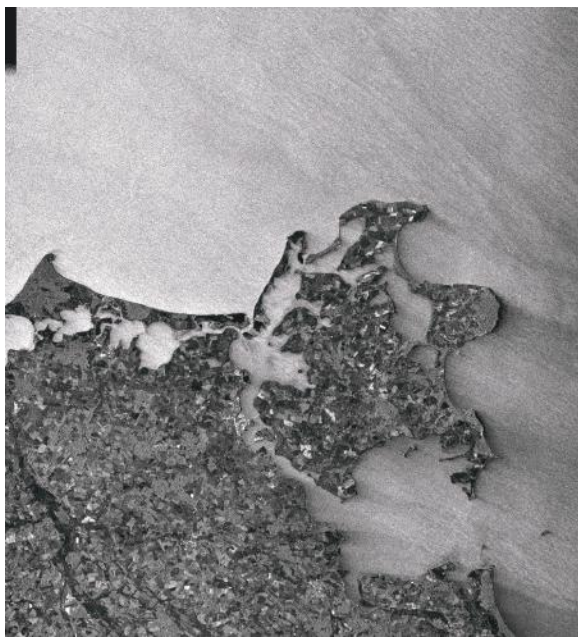


Figure 2.57 Radar image of the island of Rügen, Germany. (ERS-1 SAR © ESA, processed by DLR, courtesy of DLR, Oberpfaffenhofen, Germany.)

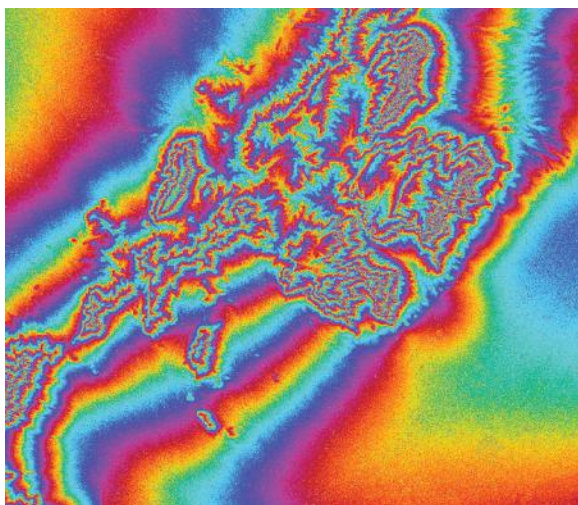


Figure 2.58 Interferogram of two radar images. (DEM from ERS 1/2 SAR © ESA, courtesy of DLR, Oberpfaffenhofen, Germany.)



Figure 2.59 Digital elevation model derived from interferogram for the area of Hannover, Germany. (DEM from ERS 1/2 SAR © ESA, courtesy of DLR, Oberpfaffenhofen, Germany.)

in X-band. A TerraSAR-X image for the Swiss city of Solothurn is shown in [Figure 2.60](#). Another image ([Figure 2.61](#)) demonstrates the distortions of radar geometry imaging a highway bridge and hilly terrain. [Figure 2.62](#) shows an open pit coal mine near Cologne, Germany. [Figure 2.63](#) illustrates the Tandem-X configuration together with TerraSAR-X to generate interferometric data for elevation models. [Figure 2.64](#) gives the result of an interferometric survey of the Hamburg harbor in Germany, showing elevation changes in color due to subsidence.

Radar Imaging Modes

Satellite radar images from high-resolution satellites, such as TerraSAR-X or Radarsat can be generated by three different scan modes:

- The basic imaging mode is the Stripmap SAR. In this mode, the antenna orientation is fixed and the side-looking radar image is generated line by line, as the satellite orbits.
- In the Scan SAR mode, a wide area of coverage is achieved by simultaneously scanning adjacent subswaths, generating lower-resolution overview images.
- In the Spotlight mode, a higher geometric resolution is obtained by directing the radar beam to the same area by multiple pulses over time.

For TerraSAR-X, the GSD in Scan SAR is 16 m, in Stripmap it is SAR 3 m, and in Spotlight it is mode 1 m or better.



Figure 2.60 TerraSAR-X image of the city Solothurn, Switzerland. (From DLR, Oberpfaffenhofen, Germany.)



Figure 2.61 Radar imaging distortions. (From DLR, Oberpfaffenhofen, Germany.)



Figure 2.62 TerraSAR-X image of coal surface mining near Cologne, Germany. (From DLR, Oberpfaffenhofen, Germany.)

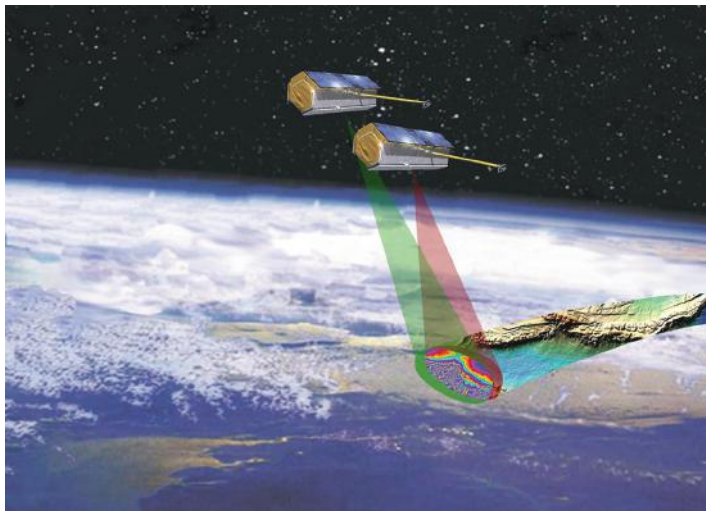


Figure 2.63 Tandem X-TerraSAR Interferometry. (From DLR, Oberpfaffenhofen, Germany.)



Figure 2.64 Interferometric survey of elevation changes in Hamburg harbor, Germany. (From DLR, Oberpfaffenhofen, Germany.)

PLATFORMS

Aircraft

The classic sensor platform is the aircraft. In order to systematically cover a portion of the earth's surface by aerial photography, flight planning is required. The aerial flights are arranged in parallel strips allowing a sufficient overlap of imaged areas by about 20% to 30%. Along the flight axis, an overlap of 60% is generally chosen, so that an overlapping pair of photos may permit the location of any photo point in at least two photographs. Since two photos are required from different exposure stations to determine an object point in three dimensions, the overlap scheme not only fulfills this condition but also permits the construction of a strong geometric interconnection between the adjacent images. The flight-planning scheme is shown in Figure 2.65.

An aerial photograph has the standardized dimension, a' , of 23 cm. Thus, the area covered by a vertical photograph $A = a'^2$, in which

$$a = \frac{h}{f} a'$$

with the flying height, h , and the principal distance, f .

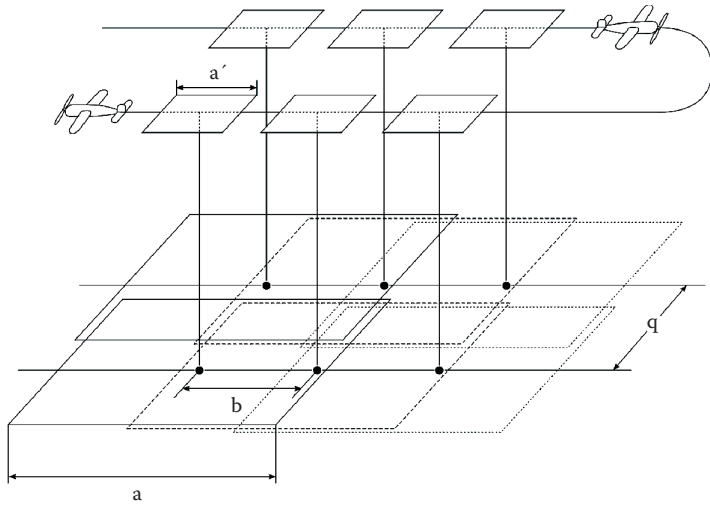


Figure 2.65 Flight plan.

The base between two subsequent photos in the strip becomes

$$b = a \left(1 - \frac{o}{100}\right)$$

in which o is the chosen longitudinal overlap of 60%. Thus, b is usually:

$$b = a \cdot 0.4$$

When the overlap between strips, p , is 20%, then the distance between two strips, q , becomes

$$q = a \left(1 - \frac{p}{100}\right) = a \cdot 0.8$$

A single model composed of the interior parts of the two photographs is of significance to calculate the number of photos required. This neat area, N , has the dimensions:

$$N = b \cdot q$$

Thus, the number of photos, n , required to cover a total area, B , is

$$n = \frac{B}{N}$$

For these photos, a film length of $0.25 \text{ m} \times n$ will be required. The scale of the image is 1:scale factor. The image scale factor is given by the ratio h/f . h is the flying height above ground. To reach the required overlap conditions, this height is always taken at the maximum altitudes of the terrain to be imaged.

Among the possible lens cones to be chosen for the flight are wide-angle objectives with the principal distance of 153 mm or normal angle objectives with the principal distance of 305 mm. In special cases, super wide-angle objectives with a principal distance of 85 to 88 mm may be utilized.

Wide-angle objectives are the most widely used. They offer about equal accuracy to determine positions and elevations. However, they have larger displacements by elevated objects such as buildings and trees. Thus, larger areas may become hidden through these objects. For this reason, urban and forest surveys in general prefer normal angle photography.

The aircraft altitude depends on the nature of the aircraft. Only military planes reach altitudes between 12 and 25 km. From 8 to 12 km, jet aircraft are required. Below 8 km, turbo prop and propeller-driven airplanes may be used. The lowest altitude, h_{\min} , at which aerial flights can be made depends on the flight velocity with respect to the ground, v , and the required minimum time interval between exposures fixed by the camera, Δt_{\min} :

$$h_{\min} = \frac{v}{a' \left(1 - \frac{0}{100} \right)} \cdot \Delta t_{\min}$$

As a rule, aerial flights are only made in clear, cloudless weather conditions when the solar altitude is higher than 30%, but it should not exceed 60° . This limits the flying season for certain areas of the globe. For topographic surveys, a winter flying season is preferred, when the foliage of trees is minimal. Central Europe, in general, only has about 22 to 28 days per year for which aerial surveys can be made.

Aerial flight navigation before the advent of GPS required the use of a variety of electronic navigation systems. Today, automatic GPS navigation with devices offered by the camera manufacturers and their affiliates have become the rule (CCNS by IGI, T-Flight and POS Z/I by Z/I Imaging, Ascot by LH Systems).

Two companies, Applanix of Canada and IGI of Germany, offer additional inertial devices, which permit the recording of flight attitudes in three axes of rotation, in addition to determining the coordinates of the exposure station at the time of exposure.

While relative positioning via differential GPS (DGPS) is possible to about ± 10 to 15 cm, angular parameters of $\pm 0.003^\circ$ may be obtained for pitch (ϕ) and roll (ω) and of $\pm 0.007^\circ$ for yaw (κ) by inertial devices. This is achieved by accelerometers for which the signals are integrated in an inertial measuring

unit (IMU). Boresight calibration procedures are required before the flight to resolve the transformation between the three spatial coordinate systems for IMU, GPS, and camera.

It has been shown that satisfactory operations are possible to cover large areas in high altitude, small-scale flights ($<1:30000$) without the use of ground control and the need for an aerotriangulation. This is particularly useful for large orthophoto projects. Also at larger photographic scales, GPS positioning and IMU attitude data can be input into aerial triangulation block adjustments to minimize the required ground control.

Satellites

After the launch of the first satellite Sputnik by the former USSR in 1957, the first U.S. satellites, such as Tiros 1 in 1960, began to carry remote sensing devices to image weather patterns.

An undisturbed satellite can stay in circular orbit, if its velocity, v , is chosen in accordance with the mass, M , around which the satellite orbits, the gravitational constant, G , and the radius of the orbit from the center of mass, r :

$$v = \sqrt{\frac{GM}{r}}$$

GM for the earth is a constant $3.980 \cdot 10^5 \text{ km}^3/\text{sec}^2$,

$$r = r_o + h$$

with $r_o = 6370 \text{ km}$ and h is the satellite altitude above the surface.

The period of one revolution, U , in minutes of time, as derived from Kepler's third law, is:

$$U = 84.491 \cdot \sqrt{\frac{r^3}{r_o^3}}$$

This means that a great number of satellites can be kept in orbit, as shown in [Table 2.8](#).

Most earth-orbiting satellites have near-circular orbits for which these simplified relations are valid.

Another orbital characteristic is the inclination, I , expressed as an angle between the orbital plane and the equatorial plane, and its relation to the vernal equinox.

Geostationary satellites orbit in the equatorial plane of the earth at a speed equivalent to the earth's rotation. These satellite orbits are ideal for

TABLE 2.8 SATELLITE CHARACTERISTICS

R	h	v	U	Remarks
6700 km	330 km	7.71 km/s	90.97 min	Space station
7370 km	1000 km	7.34 km/s	105.6 min	Earth observation satellite
26570 km	20200 km	3.87 km/s	12 h	GPS
42160 km	35790 km	3.07 km/s	23 h 56 m	Geostationary satellite
384400 km	—	1.02 km/s	27 d 08 m	Moon

communication satellites and for global weather satellites looking at the entire hemisphere (Meteosat, GOES1 and 2, GMS, and Insat). Their longitude positions are at 0°, 75°W, 135°W, 140°E, and 74°E.

Most Earth observation satellites (Landsat, Spot, etc.) prefer imaging in the mode of a sun-synchronous satellite. This is possible when a constant relation between orbital node and the direction to the sun is maintained.

The orbit with its inclination and the earth rotation determine the ground track of the satellite. Repetition of that track after a specified number of days is advantageous for earth observation satellites, permitting the gathering of images within a predetermined pattern.

A satellite is subjected to various orbit-degrading influences (e.g., solar drag). To keep it in the predetermined orbit, fuel must be carried on board. It is used to make occasional thrust maneuvers to achieve the required orbit corrections.

Ground Resolution versus Repeatability

Figure 2.66 illustrates the choice of a remote sensing system with its achievable resolution and with the repeatability to obtain data.

Geostationary meteorological satellites such as Meteosat and GOES permit the imaging of the entire hemisphere, as seen from an altitude of 35790 km, by an electromechanical scanning radiometer kept in constant rotation with 5 km pixels in three bands, one of which is thermal. This can be achieved every 30 minutes. Meteosat images are placed on the Internet at least three times a day.

Geostationary satellites permit the study of weather patterns throughout the day, viewing moving clouds on TV, but they are too coarse in resolution for vegetation studies and for viewing the polar regions. Thus, NOAA satellites with a polar orbit and an altitude of about 850 km permit the imaging of the earth every 12 hours at 1 km pixels at a swath of 2700 km in five channels.

Sun-synchronous remote sensing satellites such as Landsat (USA), Spot (France), and IRS (India) have a repetition rate of less than a month, but due to high cloud cover probability an image may be obtained only several times per year at medium resolutions between 5 and 15 m in panchromatic and

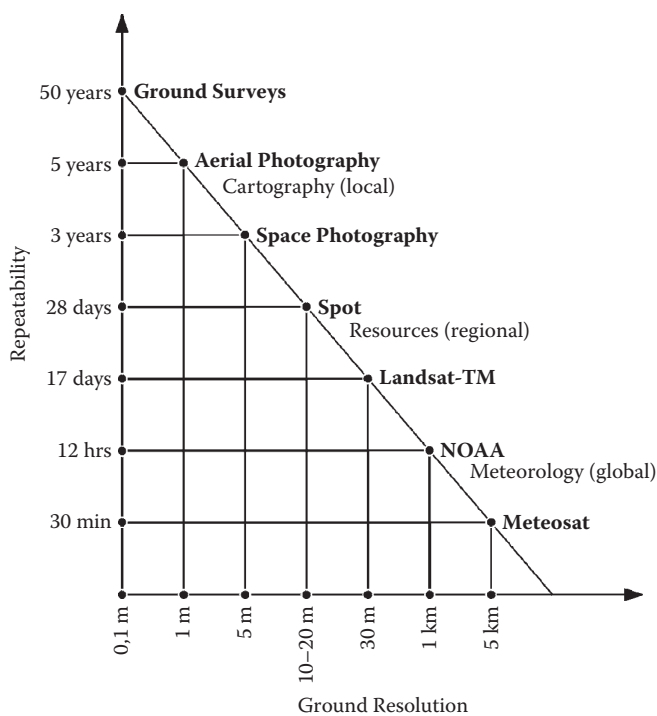


Figure 2.66 Ground resolution versus repeatability.

between 20 and 30 m in multispectral mode at swaths between 185 to 60 km.

High-resolution systems from space, such as Ikonos 2 with 1 m pixel and Russian space photography at 2 m resolution, attempt to compete with high-altitude aerial photography. However, a high area coverage with repetitiveness of less than every few years is not possible.

The highest accuracy in the centimeter to decimeter range is achieved by low-altitude aerial surveys and by ground surveys. Whether these methods can be utilized over large areas is dependent on questions of cost and time. It is appropriate to apply low-resolution, high-repetitiveness sensors for global surveys, intermediate resolution and intermediate repetitiveness surveys, and high-resolution and low-repetitiveness sensors for local (e.g., urban) surveys.

The space age began with the launch of the first satellite, Sputnik, in 1957. During the subsequent 55 years, satellite technology rapidly developed and matured. In 1961, Yuri Gagarin from Russia became the first man in space. In 1969, Neil Armstrong from the United States made his first steps on the moon. In 1981, the U.S. Space Shuttle became the first returnable platform to bring

man into space and back. This was followed in 1986 by the first space platform, MIR, leading the way to the International Space Station.

In the meantime, space technology gave rise to three phenomenal developments. Depending on the launch capabilities, three types of satellites have been introduced into practice:

1. Earth observations from low-orbiting satellites, imaging the earth with a variety of sensors at high spatial resolution, with the ability to cover changing phenomena of the earth's environment in comparison to aerial imaging platforms.
2. Medium altitude satellites in near-geostationary orbits to serve telecommunication and navigational needs.
3. Space exploration for extraterrestrial missions. This has led to an otherwise not achievable understanding of our solar system. Between 1957 and 2012, altogether 75 missions were sent to the moon, 43 to Venus, 43 to Mars, 9 to Jupiter, 5 to Saturn, 2 to Mercury, 1 to Uranus, 1 to Neptune, and 12 to the Sun.

In the context of this book, earth observations by low-orbiting satellites observing the earth are of prime interest. [Tables 2.11 to 2.15](#) demonstrate the enormous international progress made during the last 12 to 14 years. Examples of recent images are shown in [Figures 2.67 to 2.72](#).

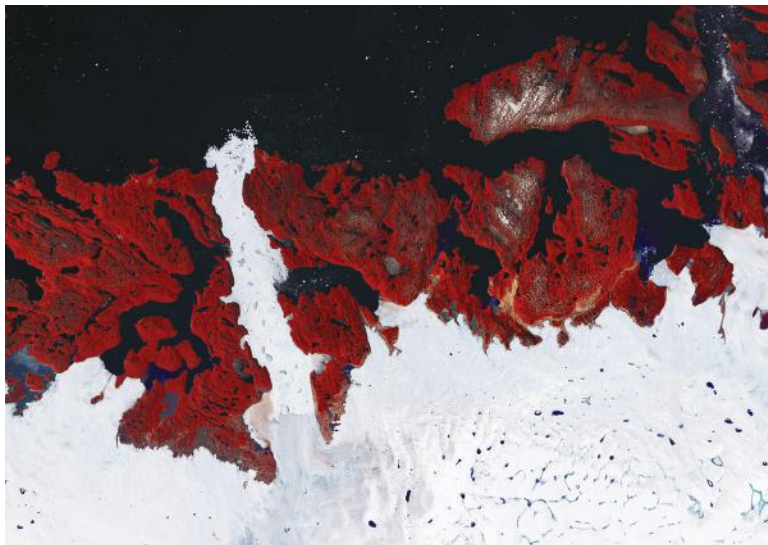


Figure 2.67 Landsat TM-ETM image of Greenland Jacobshavn glacier. (From DLR, Oberpfaffenhofen, Germany.)



Figure 2.68 Ikonos image over Cairo, Egypt. (From DLR, Oberpfaffenhofen, Germany.)



Figure 2.69 GeoEye1 image over Cologne, Germany. (From DLR, Oberpfaffenhofen, Germany.)



Figure 2.70 WorldView2 image over Dubai, UAE. (From DLR, Oberpfaffenhofen, Germany.)

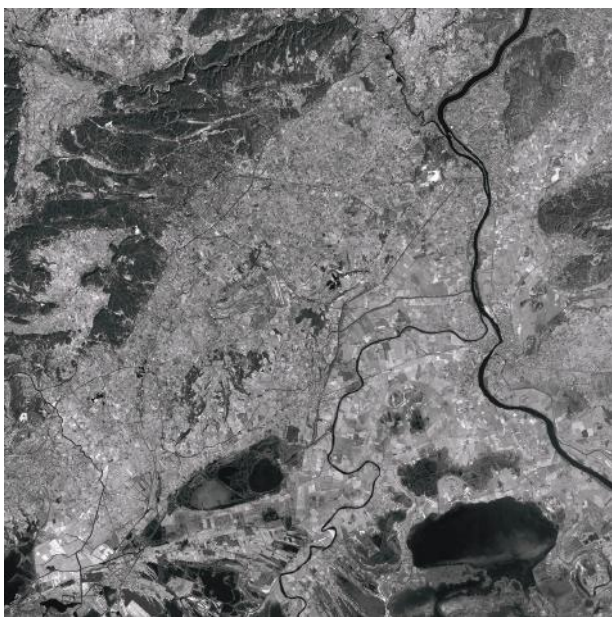


Figure 2.71 Chinese ZY-3 pan image of Rhône delta, France. (From LIESMARS, Wuhan University, China.)



Figure 2.72 Chinese ZY-3 MS image of Rhone delta, France. (From LIESMARS, Wuhan University, China.)

With respect to earth observations the following tendencies are noted:

- A multitude of sensors have now been introduced to monitor the physical behavior of our planet. The European Space Agency's (ESA's) Copernicus program has been introduced for a systematic monitoring of environmental changes.
- High-resolution optical sensors flying in constellations are now capable of monitoring rapidly changing phenomena on the earth's surface (e.g., RapidEye).
- Time series observations secured in databases are now capable of analyzing long-term environmental changes of the earth's atmosphere and the earth's surface (e.g., Landsat 1 to 8).
- The efforts to develop small satellites with miniaturized sensor and infrastructure components have made it possible to expand the possibilities, previously only available to powerful space nations, to multinational opportunities open to developing countries.
- With the great number of new satellites planned, these tendencies are expected to continue in the future.
- One of the drivers of this development is disaster management. From 1994 to 2003, there were 6145 disasters reported around the globe.

Seventy-five percent had hydrometeorological causes, 16% were biological threats, and 8% were geological events (earthquakes). In the year 2008 alone there were 397 disasters causing the deaths of 235,000 people and a loss of US\$190 billion in damages.

To effectively lessen the impact of such disasters a chain of action is required. This begins with risk assessment followed by prediction and the monitoring of actual disasters, disseminating emergency information, and response and recovery action.

Earth observation technologies, satellite communication, and satellite navigation are important elements in these tasks. A remarkable voluntary program is the International Charter for Disasters program agreed upon by the international space agencies around the globe under the United Nations Office of Outer Space to provide rapid remote sensing information free of charge to the disaster areas.

Unmanned Aerial Vehicles (UAVs)

UAVs are navigated and operated by steering controls from the ground without an onboard flight crew.

Such systems have been developed mainly for military interests (e.g., the RQ-4B Northrop Grumman Global Hawk or the Air Robot AR 100-B in the United States). Such UAVs can carry lightweight digital cameras. With these, aerial photogrammetric imagery may be recorded and restituted after recovery or transmission of the data by methods used with digital aerial mapping cameras.

Recently, UAVs have become available for civilian operators at an affordable cost. However, the legislation for the use of UAVs in different countries of the globe is still vague. Nevertheless, successful and cost-effective applications have been demonstrated for local areas and for special purposes (e.g., archaeology).

IMAGE INTERPRETATION

The image generated by a remote sensing sensor is subject to interpretation, before the remote sensing data can become information. Although there is research looking at an automation process for the information extraction procedure, currently all practical interpretations are based on the human eye–brain system.

The Human Eye

The eye performs the task of optical imaging, while the brain performs the analysis of the perceived optical data. [Figure 2.73](#) describes the composition of the human eye.

The eye possesses a lens that can change its curvature for focusing a near or far object onto the retina, creating an image. This change of focus is achieved by the movement of a muscle. The incoming light intensity on the retina is

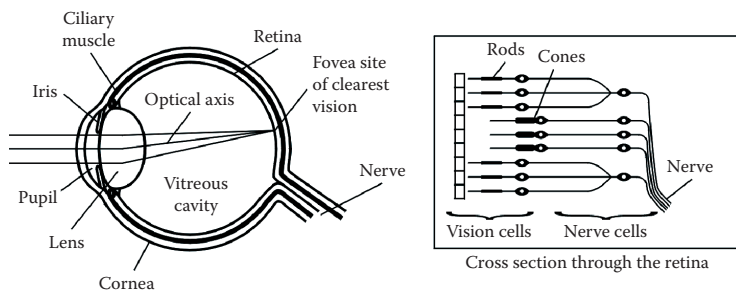


Figure 2.73 The human eye.

regulated by the pigmented part of the eye controlling the variable aperture (the pupil). The part of the retina with the highest concentration of light-sensitive cells is the fovea, extending 1° to 2° from the optical axis of the eye, whereas peripheral, low-resolution vision is possible in a range of 120° .

The young eye can change its focal length between 17 and 23 mm. The attainable resolution in the fovea is about 71 p/mm . An aerial photo of 401 p/mm can thus be observed at five- to sixfold magnification by a lens system.

The light-sensitive elements are the more densely spaced rods suitable for panchromatic sensing at low energy levels. The more widely spaced cones permit the observation of spectrally mixed energy in the form of color. The eye contains about 10^8 rods and 10^7 cones.

The lens system of the eye projects an inverted image onto the retina. The erect perception of the image is a function of the brain: the rods and cones cause chemically produced signals transmitted to the visual area of the cortex of the brain for signal processing by neural networks.

This processing analyzes the images received for gray level, color, texture, size, and context and motion, and converts them into information through a comparison with stored information in the neurons (nerve cells) of the brain. With about 10^{11} neurons contained in the brain, visual perception by far exceeds the image analysis capabilities of a computer.

Stereovision

Another interpretation tool exists in human vision; two eyes permit the fusion of two images taken from spatially different observation points, allowing a judgment of the distance of the observed object, y . **Figure 2.74** shows the capacity for natural stereoscopic vision.

The human eye base, b_E , is about 65 mm. Natural stereoscopic vision diminishes with the distance squared. The stereoscopic observation capability of the brain is $d\gamma = 15''$. Thus, the ability of the brain to judge distance differences, dy , at a distance, y , is listed in **Table 2.9**.

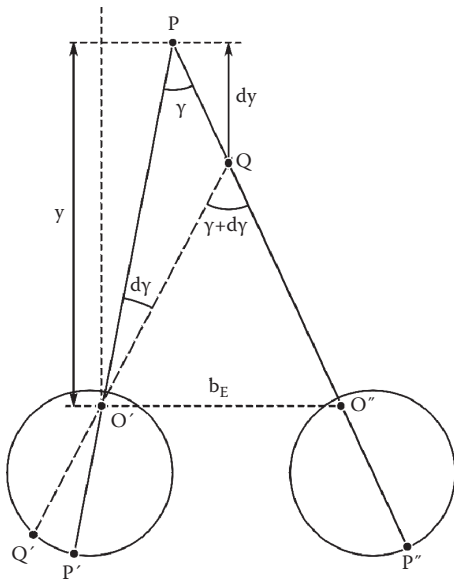


Figure 2.74 Natural stereoscopic vision.

γ , which is a small angle,

$$\gamma \approx \frac{b_E}{y}$$

By differentiation

$$d\gamma = -\frac{b_E}{y^2} dy$$

The ability to fuse images is furthermore limited by the angular range between farthest object, γ_F , and closed object, γ_c :

$$\gamma_F - \gamma_c \leq 70'$$

Image interpretation and photogrammetry have the possibility to expand the stereoscopic observation capacity to judge and to measure distances stereoscopically through the use of images, which have been taken at $n\times$ magnification of

TABLE 2.9 NATURAL STEREOSCOPIC DEPTH PERCEPTION LIMIT

y	0.25 m	10 m	100 m	500 m	894 m
dy	0.07 mm	0.1 m	11 m	280 m	894 m

the eye base. If the two images are presented to both eyes with a magnification, m , and at a magnification of the eye base

$$n = \frac{b}{b_E}$$

then

$$dy = -\frac{1}{n \cdot m} \cdot \frac{y^2}{b_E} \cdot d\gamma = -\frac{1}{m} \cdot \frac{y^2}{b} \cdot d\gamma$$

Two aerial photographs taken from a distance (flying height) of 1000 m, viewed at a 4× enlargement and at 60% overlap with a base, b , of 400 m thus permit a stereoscopic height determination from the images at 0.05 m.

For the observation of stereo adjacent aerial photographs, it is necessary to orient the images according to epipolar rays (see [Figure 2.75](#)). Epipolar rays

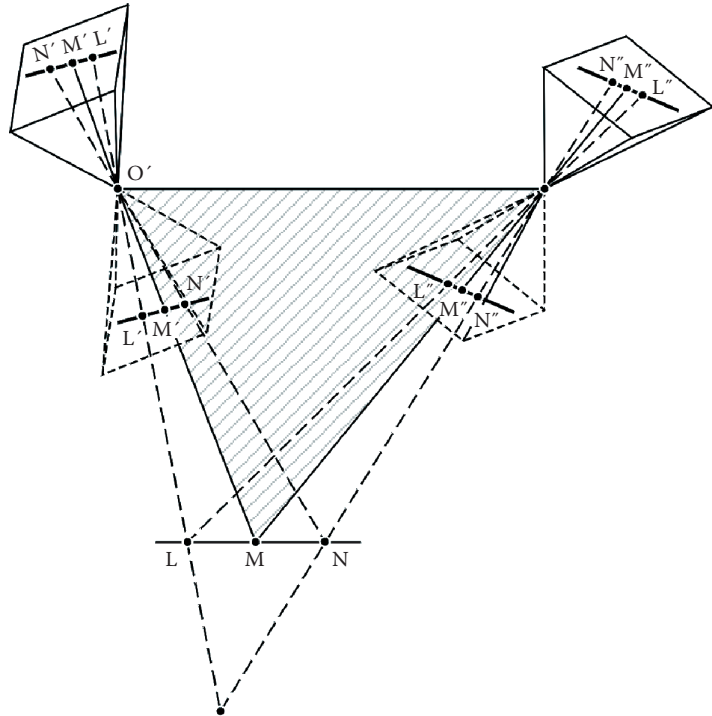


Figure 2.75 Epipolar plane and epipolar rays.

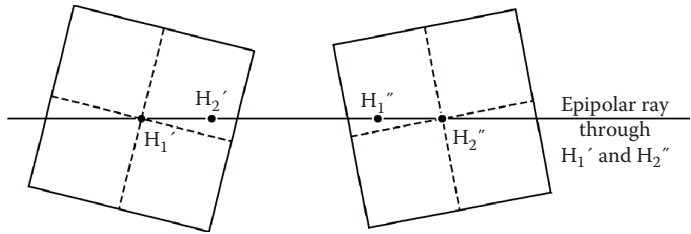


Figure 2.76 Orientation of aerial photographs according to epipolar rays.

are the lines of projection with the plane formed by the object point and the projection centers of the two images (see [Figure 2.76](#)). In practice, it is helpful to transfer the principal points H'_1 from left to right H''_1 and from right H''_2 to left image H'_2 and to position the images along a straight line containing H'_1 , H'_2 , H''_1 and H''_2 ([Figure 2.76](#)). Along this line (and parallel to it) the image points $L'M'N'$ and $L''M''N''$ can be viewed in stereo as points L , M , N ([Figure 2.75](#)). The brain is able to compensate for minor differences in that direction of about 2%, as well as scale differences up to 5%.

The images are easiest observed with lens stereoscopes having an eye base of 65 mm and a lens magnification of 1.6. The images placed along the epipolar line then require a separation of 65 mm (see [Figure 2.77](#)).

Aerial photographs of the size 23×23 m are better observed in a mirror stereoscope, which separates the images by a mirror system and allows a magnification of up to four times (see [Figure 2.78](#)).

Stereo observation is also possible via anaglyphs in complementary colors (red and green) when viewed through corresponding filters. The anaglyphic images are projected or printed on top of each other in the respective

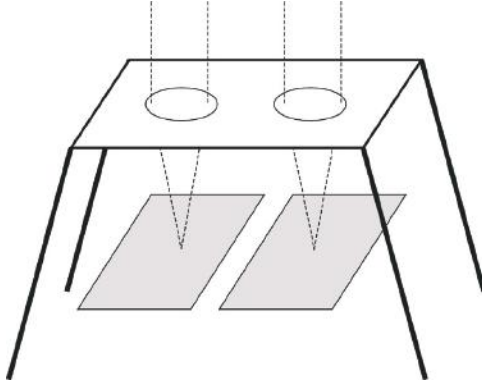


Figure 2.77 Lens stereoscope.

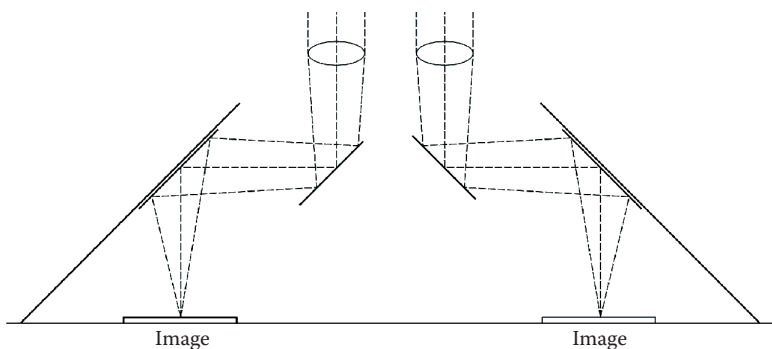


Figure 2.78 Mirror stereoscope.

colors, and viewing through filtered spectacles is possible without lenses (Figure 2.79).

Color images may be viewed if they are projected in two polarizations and viewed with corresponding polarization filters. To obtain a polarized image, not only the projected light onto a projection plane needs to



Figure 2.79 Anaglyphic stereo view of two overlapping aerial photos of Louisville, Kentucky. (Data provider: Photo Science, Inc.; Illustration provider: ERDAS Inc., the Geographic Imaging unit within Leica Geosystems GIS & Mapping Division, Atlanta, Georgia.)

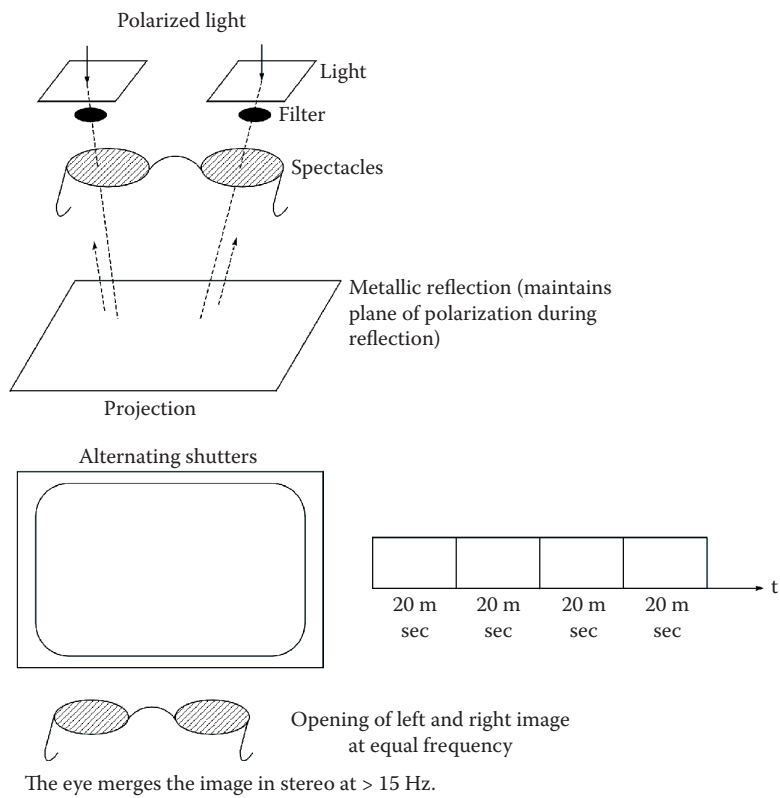


Figure 2.80 Stereo viewing by polarized light and alternating shutters.

be polarized but also the projection surface needs to reflect the projected light in polarized mode. This is possible for metallic projection surfaces (see Figure 2.80).

Stereo viewing on a computer screen becomes possible by split screens when viewed through a stereoscope. Anaglyphs may also be viewed on the screen. Special screens permit viewing with polarized light. As a rule, the “crystal eyes” principle is used, in which the left and right images are alternately generated at a 50 Hz rate. These can be viewed with filtered spectacles, which open and close the alternating left and right view at the same 50 Hz frequency.

Stereovision greatly assists in the interpretation possibilities of objects. It is also the basis for the manual photogrammetric restitution process.

Visual Interpretation of Images

Based upon the possibilities given by the human eye–brain system, the interpretation of images by an analyst starts at a primary level observing contrasts of tone and color. At a secondary level, size, shape, and texture are compared. At the third level, pattern, height difference, and shadow aids in the interpretation. At a fourth level, the association with adjacent objects plays a role.

Image interpretation has a great number of areas of application. These include:

- Military intelligence
- Forestry
- Agriculture
- Hydrology
- Topographic mapping
- Urban analysis
- Coastal area surveys
- Archaeology

For some of these applications, interpretation keys with examples of imaged objects to be interpreted have been developed.

IMAGE PROCESSING

Raster Scanning of Photographic Images

If the remotely sensed images have not been obtained by digital sensor, but by photographic imaging, the application of automated computer analysis requires a raster digitization of these images. One of the first widely used devices for this purpose, from around 1970, was the Optronics Scanner, shown in [Figure 2.81](#). It consisted of a rotating drum, onto which the film transparency was wrapped. While the image rotated, an electronically controlled lamp sent a flash of light through the aperture and the emulsion, and collected the energy on a photo multiplier. This analogue signal was amplified and digitally converted into gray levels for each exposed pixel. After exposure of an image line, the aperture was shifted by a step motor and the next line was digitized in the same manner. If desired, the scanning of the image could easily be combined with a photowrite mechanism activated by a laser diode. This permitted online image processing under control of a computer but, as a rule, it was sufficient to store the image on a suitable storage medium. Color images could be scanned sequentially using three-color filters only permitting the recording of blue, green, and red light.

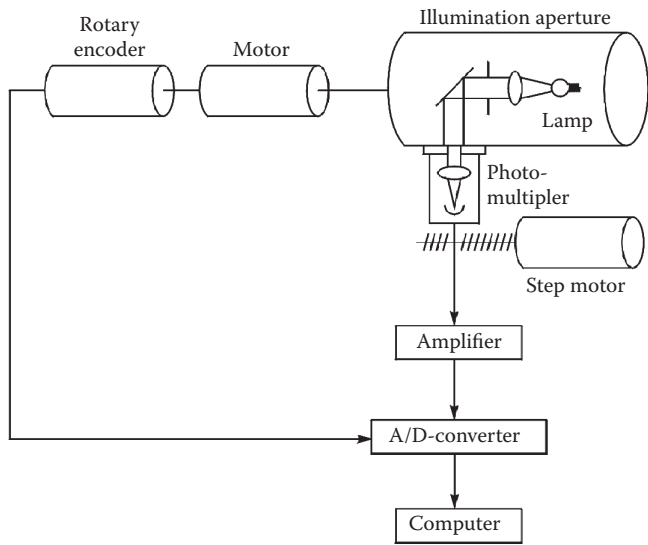


Figure 2.81 The Optronics drum scanner.

The Optronics permitted digitization in pixel increments of 12.5, 25, 50, and 100 μm . Mechanical and thermal instabilities of the instrument, however, limited the practical use to only 50 μm pixels. To reach higher digitizing resolutions, flatbed scanners have been introduced. [Table 2.10](#) gives a summary of the available devices. [Figure 2.82](#) demonstrates the principle of a flatbed scanner. [Figure 2.83](#) shows the Z/I Imaging Photoscan 2001.

Gray Level Changes

Gray level changes are single pixel-based operations, which permit the changing of the available digital density of a pixel, d_i , by changing the analogue D-log H or the digital D-H curve into a new pixel density d'_i . Examples of the possibilities are shown in [Figure 2.84](#).

- For a change of the slope of the γ curve or the response curve:

$$d'_i = a_o + a_1 d_i$$
- The response may also be logarithmically changed: $d'_i = \log^n d_i$.
- Densities may be grouped into preselected density ranges, by a step function.
- Finally, a gray level adaptation may be achieved by a histogram linearization, in which the surface under the histogram is divided into equal areas, defining new limits, d_i , which are to be imaged as d'_i with constant intervals. This is shown in [Figure 2.84](#).

TABLE 2.10 FLATBED SCANNERS FOR AERIAL PHOTOGRAPHS

Manufacturer	Name	Sensor	Color	Image Pixel Size	Radiometric Range	Film
Leica	DSW 500	Camera with 2048 × 2048 pixel patches, stair stepped	Yes	Continuous 4 to 20 μm	0.1–2.5D	Single or roll film
Vexcel	Ultrascan 5000	Trilinear array	Yes	Continuous 2.5 to 2500 μm	0–4D	Single or roll film
Wehrli	RM2 Rastermaster	Linear array	No	10 μm	0.1–2D	Single film
Z/I	Photoscan 2001	Trilinear CCD	Yes	7, 14, 21, 28, 56, 112, 224 μm	0.1–3D	Single or roll film

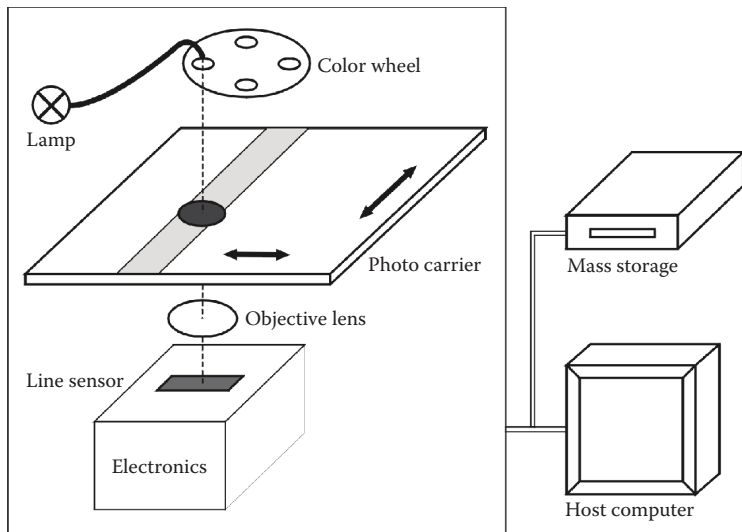


Figure 2.82 Principle of a flatbed scanner.



Figure 2.83 Z/I Photoscan 2001. (Courtesy of Z/I Imaging Corporation [Photoscan™], Huntsville, Alabama.)

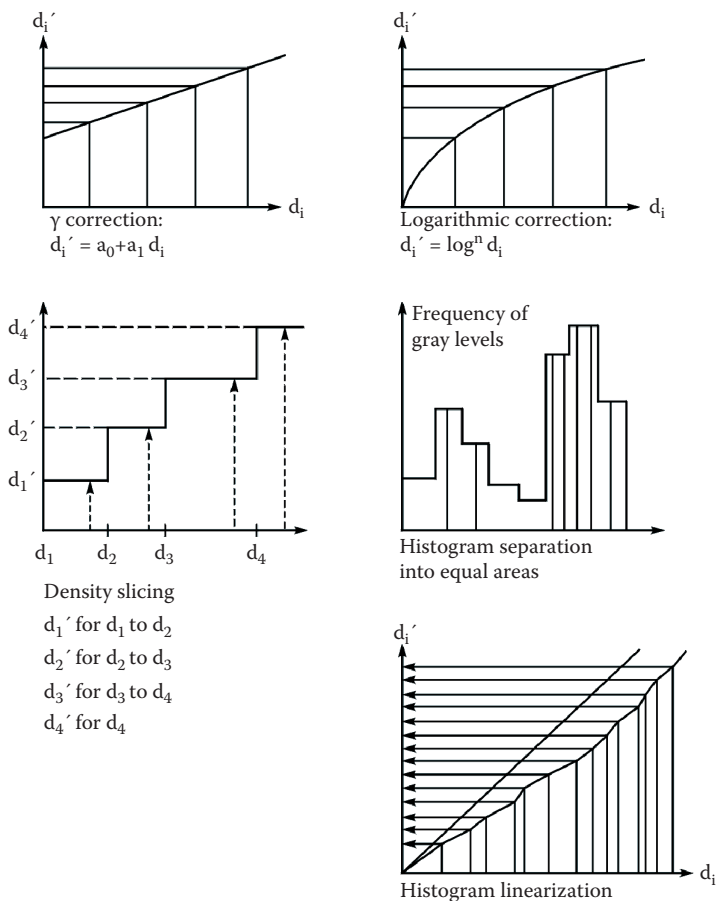


Figure 2.84 Gray level changes.

Gray level changes permit the display of an image at better contrast conditions for viewing, since the eye favors a density range between 0.1 and 1.0d.

Filtering

Filtering operations involve the adjacent pixels for each pixel. Local filters operate on an image matrix, $D(x, y)$, with a finite, usually small dimension, for example, 3×3 or 5×5 . For this matrix there exists an assigned weight matrix, $W(x, y)$. The result of the filtering process for each pixel, $d(x, y)$, results out of a convolution of the image matrix, $D(x, y)$, with the weight matrix, $W(x, y)$.

IMAGE D(X,Y)

$d_{i-1,j-1}$	$d_{i,j-1}$	$d_{i+1,j-1}$
$d_{i-1,j}$	$d_{i,j}$	$d_{i+1,j}$
$d_{i-1,j+1}$	$d_{i,j+1}$	$d_{i+1,j+1}$

FILTER W(X,Y)

1/9	1/9	1/9	+1/3	+1/3	+1/3	+1/3	0	-1/3
1/9	1/9	1/9	0	0	0	+1/3	0	-1/3
1/9	1/9	1/9	-1/3	-1/3	-1/3	+1/3	0	-1/3
Low pass			Vertical direction			Horizontal direction		
0	+1	+1	+1	+1	0	+1/3	0	-1/3
-1	0	+1	+1	0	-1	+1/3	0	-1/3
-1	-1	0	0	-1	-1	+1/3	0	-1/3
Diagonal direction			Diagonal direction					

Figure 2.85 Low-pass filter and directional filters.

Examples for a 3×3 image matrix, $D(x,y)$, and a number of important weight matrices, $W(x,y)$, are shown in Figures 2.85 and 2.86.

The result of the convolution for pixel i,j is:

$$D'(i,j) = W(x,y)^* D(x,y)$$

- Applied to a low-pass filter this means:

$$d'_{ij} = \frac{1}{9} \left(\sum_{k=i-1}^{k=i+1} \sum_{\ell=j-1}^{\ell=j+1} d_{k,\ell} \right)$$

- Applied to a vertical directional contrast:

$$d'_{ij} = \sum_{k=i-1}^{k=i+1} |d_{k,j-1} - d_{k,j+1}|$$

- Applied to a horizontal directional contrast:

$$d'_{ij} = \sum_{k=j-1}^{k=j+1} |d_{i-1,k} - d_{i+1,k}|$$

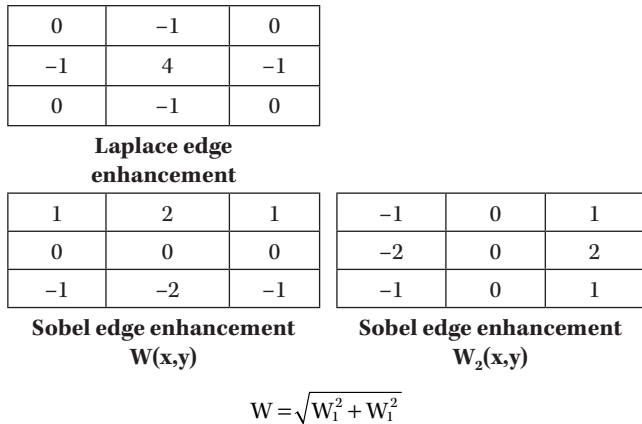


Figure 2.86 Edge enhancement filters.

Diagonal contrasts can be obtained in an analogous manner by the shown filters.

- The Laplace operator for edge enhancement is:

$$\Delta d(i,j) = \frac{\delta^2 d_{ij}}{\delta x^2} + \frac{\delta^2 d_{ij}}{\delta y^2}$$

Its approximation becomes:

$$d'_{ij} = 4d_{ij} - (d_{i-1,j} + d_{i,j-1} + d_{i+1,j} + d_{i,j+1})$$

- Edge enhancement is also possible by the Sobel operator, in which two filter matrices $W_1(x,y)$ and $W_2(x,y)$ are applied simultaneously.
- A high-pass filter results from the subtraction of a low-pass filtered image from the original image:

$$d'_{ij} = 2d_{ij} - d'_{i,j}$$

The filtering operations are executed pixel by pixel for the entire image.

Another type of filtering is possible for the entire image using the frequencies at which the gray values occur. This involves calculation of a Fourier transform for the image. It is basically a coordinate transformation from the

image space in Cartesian coordinates (x, y) or in polar coordinates r, α into Fourier Space (u, v) , where the frequency of the signal f and α are represented as polar coordinates.

The calculation of a Fourier transform of the image, D , is:

$$FouD(u, v) = \int_{-\infty}^{+\infty} \int_{-\infty}^{+\infty} e^{2\pi\sqrt{-1}(ux+vy)} \cdot D(x, y) dx dy$$

If a filter, W , is subjected to the same type of transformation

$$FouW(u, v) = \int_{-\infty}^{+\infty} \int_{-\infty}^{+\infty} e^{2\pi\sqrt{-1}(ux+vy)} \cdot W(x, y) dx dy$$

then the filtered image Fourier transform can easily be obtained by the multiplication of the two Fourier transforms in u, v space:

$$FouD'(u, v) = FouW(u, v) \cdot FouD(u, v)$$

$D'(u, v)$ can be subjected to an inverse Fourier transformation to obtain the filtered image, $D'(x, y)$, in the image space:

$$D'(x, y) = Fou^{-1} D'(u, v) = \int_{-\infty}^{+\infty} \int_{-\infty}^{+\infty} e^{-2\pi\sqrt{i}(ux+vy)} \cdot FouD'(u, v) du dv$$

Use of Fourier filtering is particularly useful for the purposes of image reconstruction, when known or estimated sources of image degeneration need to be eliminated or, at least, reduced.

For the source of degradation (defocusing, image motion), a modulation transfer function $M(u, v)$ can be set up

$$\frac{1}{M(u, v)}$$

can be used as an inverse filter $I(u, v)$.

The Fourier transform of the reconstructed image then becomes

$$FouD'(u, v) = FouD(u, v) \cdot I(u, v)$$

in which $FouD(u, v)$ is the Fourier transform of the degraded image.

The inverse Fourier transform of $D'(u, v)$ then yields the reconstructed image $D(x, y)$, improved in sharpness:

$$D'(x, y) = Fou^{-1} D'(u, v)$$

Geometric Resampling

The geometry of a two-dimensional image is distorted due to the imaging geometry of the sensor, the sensor orientation, and the displacement of the three-dimensional scene when imaged into two dimensions; for these deformations of the image, models exist which are described in Chapter 3. Such a model is a function between image coordinates, $x'_i y'_i$, and object coordinates, $x_i y_i z_i$:

$$x'_i = f_1(x, y, z)$$

$$y'_i = f_2(x, y, z)$$

The inverse relations may be generated from these functions as:

$$x'_i = f_3(x', y', z)$$

$$y'_i = f_4(x', y', z)$$

With the functions f_1, f_2, f_3 , and f_4 known, two resampling algorithms for geometric correction of the images may be used. They are illustrated in Figures 2.87 and 2.88.

In the direct method of resampling, the coordinate $x_i y_i$ of an image pixel $x'_i y'_i$ is calculated with functions f_3 and f_4 . The z_i is to be interpolated within the $x_i y_i$ pixel grid. The density $d'_{x'y'}$ is transferred to that location. All calculated points are used for further interpolation of the gray values of the output pixel matrix.

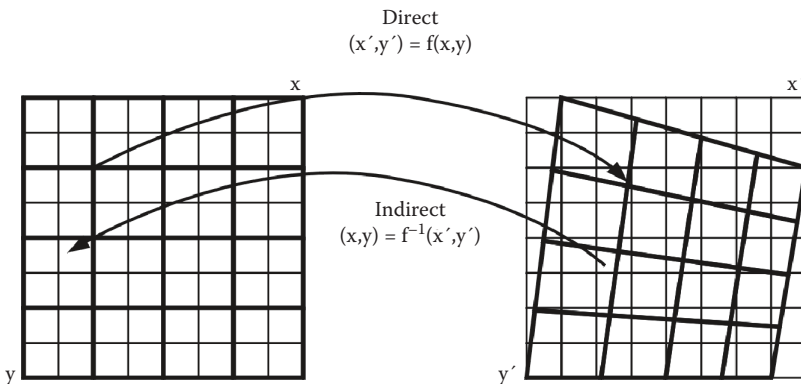
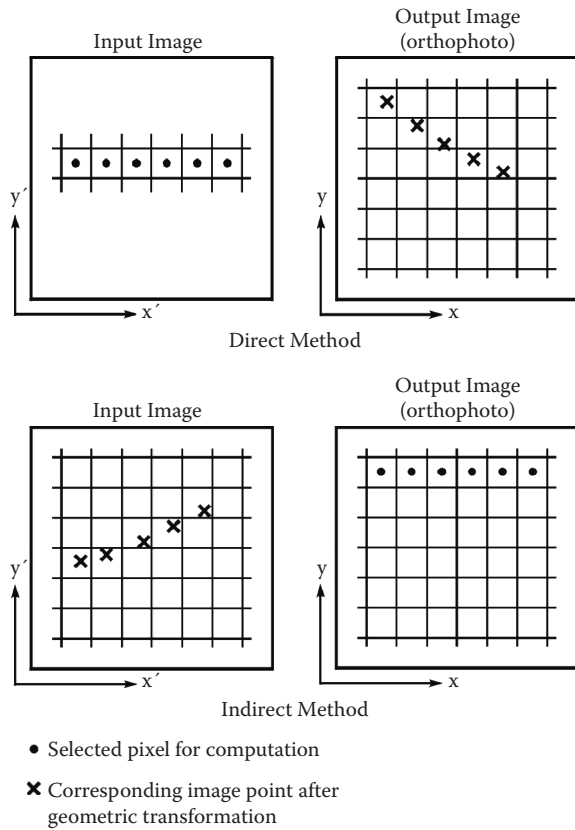


Figure 2.87 Digital rectification.



- Selected pixel for computation
- ✗ Corresponding image point after geometric transformation

Figure 2.88 Digital rectification.

In the simpler indirect resampling method, the output pixel $x_i y_i$ coordinates with their known or interpolated height z_i permit the calculation of the location of an image point $x'_i y'_i$ assigned to the output pixel.

For this assignment, it is possible to use three options:

1. The assignment of gray values to the output pixel grid by the nearest neighbor.
2. Bilinear interpolation—The nearest four pixels for the calculated image point for the indirect method, or object pixels for the direct method, with densities of d_1 to d_4 and their distances to the output or input pixel center $x_0 y_0$ are used in a weighted function:

$$d_i = \frac{p_1 d_1 + p_2 d_2 + p_3 d_3 + p_4 d_4}{p_1 + p_2 + p_3 + p_4}$$

with

$$p_k = \frac{1}{\sqrt{(x_k - x_0)^2 + (y_k - y_0)^2}}$$

with k varying from 1 to 4.

3. Cubic convolution—Here the nearest 16 calculated points are used in the same manner.

Multispectral Classification

The objective of multispectral classification is to analyze the spectral properties of unknown objects and to compare them with spectral properties of known objects. Each spectral channel consists of a digital gray level image matrix, which geometrically coincides with the gray level image matrices of other spectral channels.

For each image a histogram of gray levels can be generated. A specific object class will produce a gray level distribution, which can be compared with a normal distribution. Statistical parameters for this comparison are, for example:

- Mean of gray levels
- Variance or the standard deviation
- Maximum and minimum gray levels for this object

Two separable objects in this channel will produce two gray level distributions.

Two channels define a two-dimensional feature space, in which the gray levels of different object types are shown as clusters (see [Figure 2.89](#)).

For n channels, there exists an n -dimensional feature space. Each pixel in any of the multispectral images can be expressed by an n -dimensional feature vector:

$$\boldsymbol{x} = \begin{pmatrix} x_1 \\ x_2 \\ \vdots \\ x_n \end{pmatrix}$$

containing the gray levels in each band.

For all object clusters, a mean value, \boldsymbol{m} , can be formed:

$$\boldsymbol{m} = \frac{1}{K} \sum_{k=1}^K \boldsymbol{x}_k$$

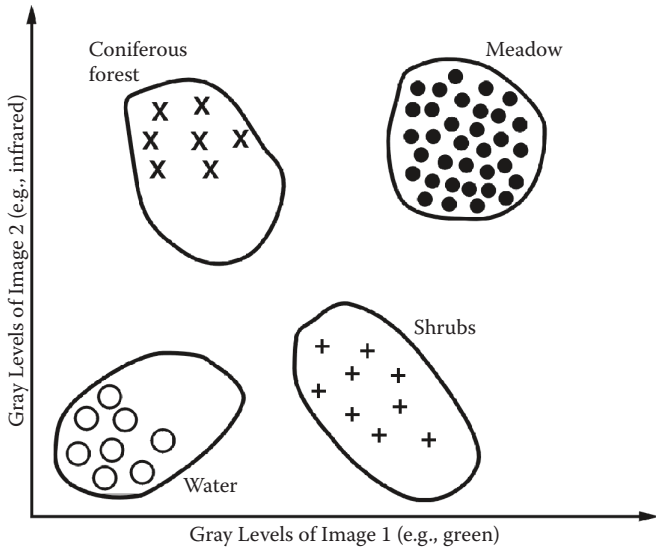


Figure 2.89 Two-dimensional feature space with object clusters.

The simplest type of classification is, then, for each group of pixels with the same geometry to form the minimum Euclidian distance to the cluster centers, m . Each pixel, i , obtains the classification of the closest cluster:

$$d(x_i, x_m) = \sqrt{(x_i - x_m)^T \cdot (x_i - x_m)}$$

The minimum distance classification can be refined into a maximum likelihood classification by use of covariance matrices for each cluster.

The covariance matrix, Σ_x , can be expressed as:

$$\Sigma_x = \frac{1}{K-1} \sum_{K=1}^K (x_K - m)(x_K - m)^T$$

From the covariance matrix, Σ_x , the correlation matrix, R , can be formed, in which the coefficients of the matrix are scaled down to a diagonal value of 1, so that the elements of the covariance matrix, v_{ij} , are transformed to

$$r_{ij} = \frac{v_{ij}}{\sqrt{v_{ii} \cdot v_{jj}}}$$

The study of the covariance matrix or of the correlation matrix therefore permits the checking of the separability of the chosen object classes.

Each feature vector finds the probability of belonging to a certain class, ω :

$$p(x) = \frac{1}{(2\pi)^{n/2} |\Sigma|^{1/2}} \exp\left\{-\frac{1}{2}(x-m)^T(x-m)\right\}$$

The measure of separability between two probability distributions of the classes ω_i and ω_j is the divergence, d_{ij} :

$$d_{ij} = \int_x \left\{ p(x|\omega_i) - p(x|\omega_j) \right\} \ln \frac{p(x|\omega_i)}{p(x|\omega_j)} dx$$

It represents a covariance-weighted distance between the means of two object pairs. It may be calculated as

$$d_{ij} = \frac{1}{2} T_r \left\{ (\Sigma_i - \Sigma_j)(\Sigma_i^{-1} - \Sigma_j^{-1}) \right\} + \frac{1}{2} T_r \left\{ (\Sigma_i^{-1} - \Sigma_j^{-1})(m_i - m_j)(m_i - m_j)^T \right\}$$

with T_r being the trace of the matrix in question.

More refined judgments are possible by the Jeffries-Matusita distance J_{ij} , which is the distance between a pair of probability distributions:

$$J_{ij} = \int_x \{\sqrt{p(x|\omega_i)} - \sqrt{p(x|\omega_j)}\}^2 dx$$

For normally distributed classes, it becomes the Bhattacharyya distance, B :

$$B = \frac{1}{8} (m_i - m_j)^T \left\{ \frac{\Sigma_i + \Sigma_j}{2} \right\}^{-1} (m_i - m_j) + \frac{1}{2} \ln \left\{ \frac{|(\Sigma_i + \Sigma_j)/2|}{|\Sigma_i|^{\frac{1}{2}} \cdot |\Sigma_j|^{\frac{1}{2}}} \right\}$$

The covariance matrix, Σ_x , or the correlation matrix, R , shows that the feature vectors, x , assigned to object clusters, m , are often highly correlated between the n channels available. This permits the rotation of the feature space, x , by a rotation matrix, G , into a new feature vector space, y , so that $y = Gx$ for which the covariance matrix, Σ_y , becomes a diagonal matrix of eigenvalues, λ_i :

$$\Sigma_y = \begin{pmatrix} \lambda_1 & 0 & 0 \\ 0 & \lambda_2 & 0 \\ & \ddots & \vdots \\ 0 & 0 & \dots & \lambda_n \end{pmatrix}$$

This transformation is called a principal component transformation. Only the equations with the largest eigenvalues suffice for an optimal separation of the chosen classes in feature space.

Classification can be performed in two ways:

1. Supervised classification—It is applied if a number of object types can be recognized in the images. This implies delineation of training areas as a subset of image pixels and a generation of clusters for these areas, determining their mean vector, m . This permits the direct use of the minimum distance classifier.

Another simple possibility is to apply a parallelepiped classifier in which the parallelepiped dimensions are formed from the maximum and minimum gray values of the training areas for a certain object, with the risk of class overlaps.

Most appropriate is the use of the maximum likelihood classifier for each object class with its covariance matrix.

The decision rule that x belongs to ω_i is

$$x \in \omega_p \text{ if } p(\omega_i|x) > p(\omega_j|x)$$

for all $j \neq i$.

A somewhat simpler classification is possible by the Mahalanobis distance. In the special case, that all priority probabilities are assumed equal, the decision function becomes the Mahalanobis distance:

$$d(x, m_j)^2 = (x - m_j)^T \Sigma^{-1} (x - m_j)$$

The Mahalanobis classifier, like the maximum likelihood classifier, retains sensitivity to direction contrary to the minimum distance classifier.

An internal check of the classification accuracy is possible through analysis of classifications for the training areas. There it is possible to generate a confusion matrix for all object classes, listing the total numbers of pixels in each training area and their portion classified into other object classes. Obviously, an overall check in this form should be made for data obtained in the field.

2. Unsupervised classification—If no ground information to establish training areas is available, then clustering must be started by an iterative procedure estimating the likely location of clusters for ω objects. For example, in three-dimensional space, a set of clusters may be chosen along the diagonal at equal distances. Then a preliminary minimum distance classification is made, and the mean vector of the cluster centers is formed. Then the process is iterated.

The obtained clusters can again be checked via the divergence to decide whether some clusters should be merged. A maximum likelihood classification can follow the process. At the end the classification result can be assigned as a plausible object class.

While the statistical approach to multispectral classification prevails in practice, another approach using neural networks is possible.

In two dimensions, a straight line may be drawn between two pixels so that

$$w_1xw_1 + w_2xw_2 + w_3 = 0$$

with x_1, x_2 representing gray values and w_1, w_2, w_3 as weights. In n -dimensions, for n bands, the equation becomes

$$w_1x_1 + w_2x_2 + \dots + w_nx_n + w_{n+1} = 0$$

or

$$w^T x + w_{n+1} = 0$$

For a set of image data, these weights have to be determined by a training process with the decision rules:

$$\begin{aligned} x &\in \text{class 1 if } w^T x + w_{n+1} > 0, \text{ or } w^T y > 0 \\ x &\in \text{class 2 if } w^T x + w_{n+1} < 0, \text{ or } w^T y < 0 \end{aligned}$$

The weight, w , is modified to w' with a correction increment, c :

$$w' = w + cy$$

so that

$$w'^T y = w^T y + c|y|^2$$

In practice, this is iterated until

$$w'_i = w_i + cy$$

and

$$w'_j = w_j - cy$$

The disadvantage of the pixel-based multispectral classification approach is that homogeneous objects are not treated as a unit. This can be overcome by image segmentation. Image segmentation can be implemented either by edge detection techniques or by region growing. The classification algorithms may then be applied to regions rather than to pixels. A recently developed product is the eCognition “context-based” classifier.

If segmented data are available through a GIS system, a knowledge-based classification approach may be applied to image regions. Knowledge is introduced by a set of rules: *if* a condition exists, *then* inference is applied. Figure 2.90 shows the example of a semantic network, which can be used to test segmented images for their content.

Examples for such rules are

- If Landsat band 7 > Landsat band 5, then vegetation
- If radar tone is dark, then smooth surface

It is also possible to incorporate texture parameters into the classification process. Characteristic texture parameters for an image region are

- Autocorrelation function
- Fourier transforms
- Gray level occurrence

An example of a multispectral classification of a multispectral image (Figure 2.91) is shown in Figure 2.92 for the urban area of Augsburg, Germany, with a Landsat image.

Classification Accuracy

Of great interest in remote sensing is the assignment of multispectral classification accuracy.

Traditionally, the accuracy has been checked by photointerpretation, assuming that this higher-resolution classification is 100% correct. This permits an error matrix to be developed for the classes chosen and the pixels or objects correctly or incorrectly determined.

The application of statistical techniques is often handicapped because of a lack of a normal distribution for the observations.

One of the tools to compare two independent classifications is Cohen's Kappa Test. If one classification is superior in accuracy (e.g., by photointerpretation)

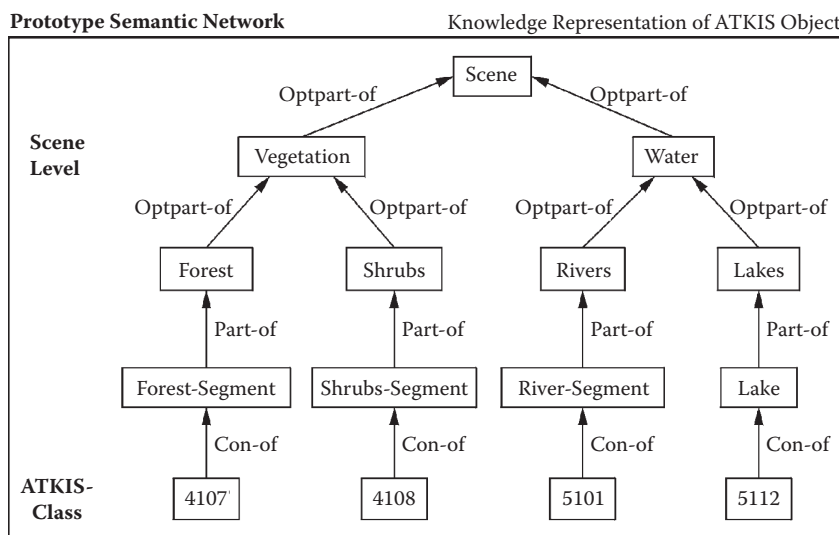


Figure 2.90 Semantic network. (From the Institute for Photogrammetry and GeoInformation, University of Hannover, Germany.)

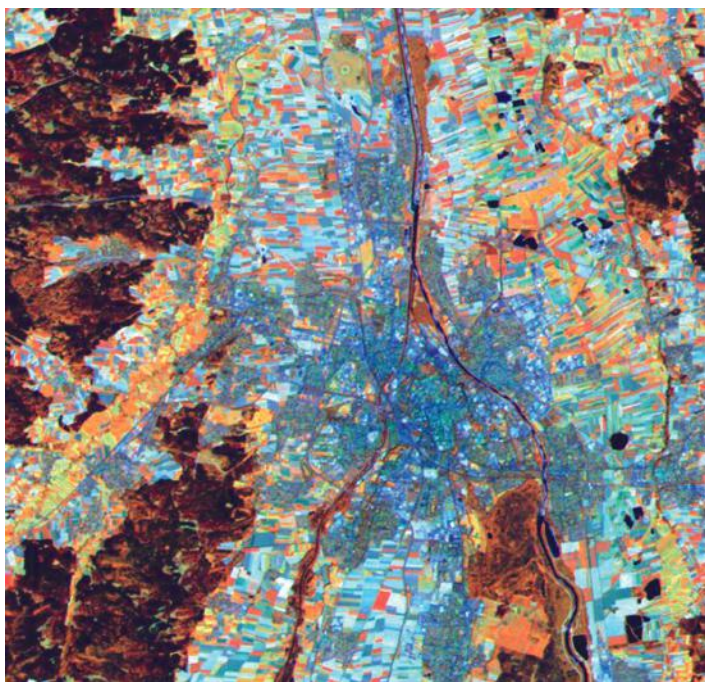


Figure 2.91 Multispectral Landsat image of Augsburg in Germany. (Landsat 7 false color composite; USGS 2000, GAF 2000, courtesy of GAF Remote Sensing and Information Systems, Munich, Germany.)

and the other is derived from satellite imagery, the agreement for a certain object class will be less than 1 (e.g., 0.1 = poor; 0.5 = moderate; 0.7 = substantial; 0.9 = perfect).

Image Fusion

Image fusion in remote sensing is a technique by which high-resolution single-channel (panchromatic) images are geometrically merged with lower-resolution multispectral images in three spectral bands for visualization in the colors blue, green, and red. As the color space is not suitable for merging because of correlation between channels, the multispectral information is transformed into intensity, hue, and saturation of the three colors, with the intensity representing the high-resolution component of the panchromatic image.

The methodology is also applicable to more than three multispectral channels, if the number of existing bands is subjected to a principle component transformation.

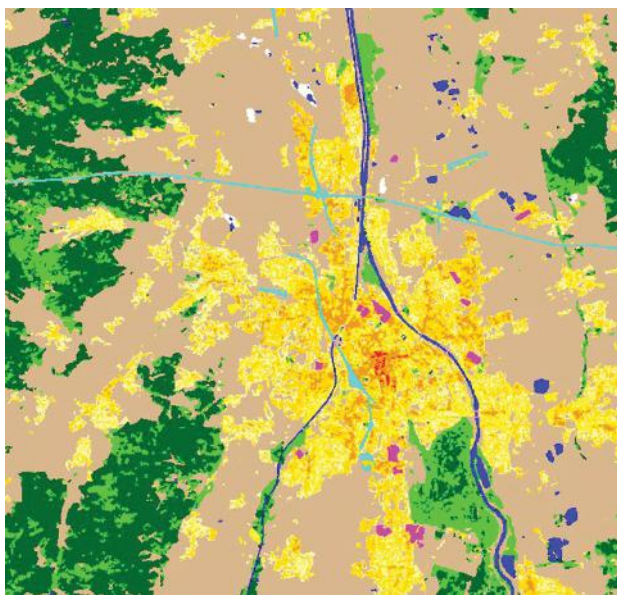


Figure 2.92 Multispectral classification of Augsburg in Germany. (Land cover classification, courtesy of GAF Remote Sensing and Information Systems, Munich, Germany.)

Provided that the images are geometrically registered with respect to each other, multitemporal and multisensor data fusion may also be used. A comparison of multitemporal data is generally done for change detection. Here again, a knowledge-based approach is advantageous.

REMOTE SENSING APPLICATIONS

A great number of satellite systems have provided satellite imagery for remote sensing applications in different disciplines. Table 2.11 provides a summary of the classical remote satellite systems with optical sensors. Table 2.12 augments this list with the high repletion satellites, which have been available since 1999. Table 2.13 lists important new medium resolution satellites that have been launched since the millennium. Table 2.14 shows the early classical radar satellite systems; Table 2.15 augments the list with the recent high-resolution radar systems since the millennium.

In addition to these satellites, a great number of images have been acquired through shorter duration missions by Russian photographic camera systems from Kosmos satellites and the MIR space station, for example, the Russian KFA 1000, KVR 1000, and TK 350 cameras; the German Metric camera on the space shuttle; as well as the MOMS-2P digital sensor flown on the space shuttle and on MIR.

TABLE 2.11 COMMONLY USED CLASSICAL OPTICAL REMOTE SENSING SATELLITES

Type	Name	Orbit	Repeat Cycle	Swath	<i>h</i>	Resolution	Bands	Country	Application
Meteorological	Meteosat	Geostationary	30 min	Half spheric	36000 km	5 km		ESA	Meteorology, climate
	GOES-1	75°W						USA	
	GOES-2	135°W						USA	
	GSM	140°E						Japan	
	Insat							India	
	Meteor 3							Russia	
	FY 2	105°E						China	
Meteorological	NOAA	Polar	12 h	2394 km	705 km	1 km	5	USA	Climate
	DMSP	Polar		2400–3000 km		3 km	0.58–21.5 μm	USA	Military
	5 satellites	Polar					6	Russia	Climate
	Meteor P						6		(TOMS, ozone)
							0.31–0.38 μm		
Earth resources	Landsat (1–3) MSS	Sun synchronous 9:30 at 40°	18 d	185 km	918 km	80 m	3–4	USA	1972–1984

	Landsat (4-5) TM	10:30 at 40°	16 d	185 km	705 km	30 m (thermal 120 m)	7	USA	1982, 1984
	Landsat 7 TM	10:00 at 40°	16 d	185 km	705 km	15 m pan	7	USA	1999
Earth resources	Spot P 1-4	Sun synchronous	26 d	60 km	832 km	10 m pan	1	France	1986
	Spot XS 1-4	10:00 at 40°				20 m MS	3		1993
Earth resources	JERS 1 OPS			75 km	568 km	20 m	7	Japan	1992
Earth resources	IRS 1 A,B	Sun synchronous	22 d to 24 d	141 km	904 km	MS 36.6 m	3	India	1988, 1991
	IRS 1 C,D	9:25 at equator			774 km	Pan 5.6 m	1		1995, 1997
						MS 23.5 m	3		
						WIFS 188 m	2		
Cartographic	Ikonos' 2	Sun synchronous	11 km	677 km	1 m pan	1	USA	1999	
	EROS A1	Sun synchronous	12 km	480 km	4 m MS	1	Israel	2000	
		Sun synchronous	8 km	450 km	1.8 m pan	1	USA	2001	
					0.6 m pan				
					2.4 m MS				

TABLE 2.12 RECENT OPTICAL HIGH-RESOLUTION SATELLITE SYSTEMS

Agency	Satellite	Year	GSD-pan	GSD-MS	Number of Bands	Swath	Remarks
Digital Globe, USA	Ikonom	Sept 1999	0.82 m	3.2 m	4	11.3 km	
Imagesat, Israel	EROS-A	Dec 2000	1.9 m	—	—	14 km	Pan only
Digital Globe, USA	Quickbird	Oct 2001	0.61m	2.44 m	4	16.5 km	
CNES, France	Spot 5	May 2002	2.5/5 m	5/10 m	4	60 km	
Taiwan	Formosat 2	May 2004	2 m	8m	4	24 km	
ISRO, India	Cartosat 1	May 2005	2.5 m	—	—	30 km	Pan, stereo
Jaxa, Japan	Alos	Jan 2006	2.5 m	10 m	4	70 km	Stereo
Imagesat, Israel	EROS-B	April 2006	0.7m	—	—	11 km	Pan only
Russia	Resurs-DK1	June 2006	0.9 m	2.5 m	3	28.3km	
Digital Globe, USA	WorldView 1	Sept 2007	0.5 m	—	—	17.6 x 14 km pan (750000 km ² /d)	
ISRO, India	Cartosat 2A,B (2010)	April 2008 (July 2010)	0.8 m	—	—	9.6 km	Pan only
Digital Globe, USA	Geo Eye 1	Sept 2008	0.41 m	1.65 m	4	12.5 km (250000 km ² /d)	
Digital Globe, USA	WorldView 2	Oct 2009	0.46 m	1.8 m	8	16.4 km (1 M km ² /d)	
Astrium, F & D	Pleiades1A(B)	Dec 2011 (Dec 2012) resampled)	0.7 m (0.5 m resampled)	2 m	4	20 km constellation	
China	ZY-3	Jan 2012	2.1 m	3.5 m	2	51 km	
Korea	Kompsat 3	May 2012	0.7 m	2.8 m	4	16.8 km	

TABLE 2.13 RECENT OPTICAL MEDIUM-RESOLUTION SATELLITE SYSTEMS

Agency	Satellite	Year	GSD-pan	GSD-MS	Number of Bands	Swath	Remarks
ISRO, India	IRS-IC	Dec 1995	5.8 m	23 m	4	141 km	
NASA, USA	Landsat 7+ETM	April 1999	15 m	30 (90) m	7	185 km	
NASA, USA	ASTER	Dec 1999	—	15m VNIR	1–3	60 km	
		—	—	30m SWIR	4–9		
		—	90m TIR	10–14			
China-Brazil	CBERS 2	Oct 2003	20 m	to 260 m	4	113 km	
Germany	RapidEye	Aug 2008		6.5 m	5	77 km	Constellation, red edge, 5 satellites
UK	DMC 2	July 2009		2.2 m	3	660km	
USGS, USA	Landsat 8	May 2013	15 m	30 m (100 m Thermal)	7	185 km	

TABLE 2.14 HISTORICAL RADAR SATELLITES

Name	Year	Inclination of Orbit	Swath	<i>h</i>	Resolution	Polarization	Country/ Agency
Seasat	1978	72°	100 km	790 km	40 m	HH 23.5 cm	USA
SIR-A	1981	50°	50 km	250 km	38 m	HH 23.5 cm	USA
SIR-B	1984	58°	40 km	225 km	25 m	HH 23.5 cm	USA
SIR-C	1994	51°	30 to 60 km	225 km	Variable 13–26 m	Multiple HH, HV, VH, WV, 23.5 cm, 58 cm, 3.1 cm	USA
ERS 1/2	1991, 1995	Polar	100 km	785 km	30 m	VV 5.7 cm	ESA
JERS 1	1992	Polar	75 km	568 km	18 m	HH 23.5 cm	Japan
Almaz	1991	Polar	50 to 100 km	350 km	1.5 m, variable	HH	Russia
Radarsat	Since 1995	Polar	50 to 500 km	800 km	Up to 10 m	HH 5.7 cm	Canada
Envisat (ASAR)	2002	Polar	100 km	800 km	12.5 m	HH, WV	ESA

TABLE 2.15 RECENT HIGH-RESOLUTION RADAR SATELLITE IMAGING SYSTEMS

Agency	Satellite	Year	GSD	Swath	Band
ESA	ERS-1	1991	10–30 m	100 km	C
Jaxa, Japan	JERS1	1992	18 m	75 km	C
ESA	ERS-2	1995	10–30 m	100 km	C
Canada	Radarsat 1	1995	9–100 m	50–500 km	C
NASA, USA	SRTM	2000	30 m	225 km	C
DLR, Germany	SRTM	2000	30 m	45 km	X
ESA	Envisat	2002	30–1000 m	100–405 km	C
Italy, France	COSMO-SkyMed	2006	1–50 m	10–200 km	X
Canada	Radarsat 2	2006	3–50 m	20–500 km	C
Germany, Astrium	TerraSAR-X	2007	1, 3, 18 m	10, 30, 100 km	X
China	SurveyorSAR	2007	10–25 m	100–250 km	C
ISRO, India	Risat 1,(2)	2009 (2012)	3–50 m	10–240 km	C
Germany, Astrium	Tandem X	2010	1, 3, 16 m	10, 20, 100 km	X radar interferometry
China	Civilian	2012		Radar satellite	S



Figure 2.93 IRSIC/D image of Munich Airport in Germany. (IRS-PAN/LIIS image: Munich; SI/Antrix/Euromap 1999, GAF 2000, courtesy of GAF Remote Sensing and Information Systems, Munich, Germany.)

An example image of the airport of Munich, Germany, taken by IRS-C is shown in Figure 2.93.

These images are available from nationally and internationally operating space agencies, such as NASA, NOAA, ESA, CNES, NASDA, ISRO, or their vending agencies (e.g., USGS, Spot Image, Space Imaging, Eurimage, DigitalGlobe). The data cost still differs greatly but it is in a process of stabilization.

Meteorological data, though reduced in quality, are available over the Internet free of charge. Original resolution meteorological images can be obtained at reproduction cost. Medium- and high-resolution images have a weak to strong commercial component, depending on the policies of the space agency maintaining the satellite system. Privately funded commercial systems charge full price, unless they are supported by large government programs.

Global applications, therefore, use low-cost, low-resolution imagery, which is easily obtainable. Regional and local applications requiring higher resolutions rely on substantial imagery purchases. There, remote sensing competes with other data acquisition methods with respect to obtainable quality, cost, and evaluation effort and time.

Project-based research applications were the easiest to be realized. The present focus of applications is to concentrate on organized data acquisition

and analysis programs depending on the socioeconomic priorities to be placed on applications made possible by public or industrial funding.

We will now consider the situation in the major application areas of remote sensing.

Meteorology and Climatology

Atmospheric sciences study the different layers of the earth's atmosphere:

- Troposphere, from 0 to 20 km altitude
- Stratosphere, from 20 to 50 km altitude
- Mesosphere, from 50 to 80 km altitude
- Thermosphere, from 80 to 300 km altitude

The "weather zone" is the troposphere, which is of direct meteorological interest. However, the other zones also affect weather and climate.

Ozone

The earth's ozone shield extends from an altitude of 25 to 60 km. It absorbs or reflects most of the ultraviolet (UV) light, so that only minimal amounts of ultraviolet reach the earth's surface.

NASA has launched an ultraviolet sensor, TOMS (Total Ozone Mapping Spectrometer), which observes the ozone layer in six bands between 312.5 mm and 380 mm wavelength. From these six bands, three pairs can be formed. They determine transmission minus absorption of UV energy. This ratio is a measure of ozone concentration. TOMS was carried on the U.S. satellite Nimbus 7 from 1978 to 1993, on the Russian satellite Meteor 3 from 1991 to 1994, and on a special satellite since 1996. TOMS detected a rapidly deteriorating ozone concentration over the south polar regions in 1992 and 1993, which created great public interest. The cause could have been the eruption of the volcano Mount Pinatubo in 1991, even though aerosols produced by human activity may also have played a part. Since then, ozone measurement has been a major global remote sensing application.

The European Space Agency (ESA) launched an ozone sensor on the ERS-2 satellite in 1995. [Figure 2.94](#) shows the global ozone concentrations on a particular day ([Figure 2.94a](#)) and a monthly average ([Figure 2.94b](#)). The observations were continued by Schiamachy on Envisat under the GOME experiment for ozone studies. [Figure 2.95](#) shows the ozone vertical column density for the northern hemisphere and [Figure 2.96](#) for the southern hemisphere.

Cloud Mapping

The first U.S. imaging satellite launched in April 1961 was Tiros 1, which made it possible to observe clouds. Today, geostationary satellites permit a

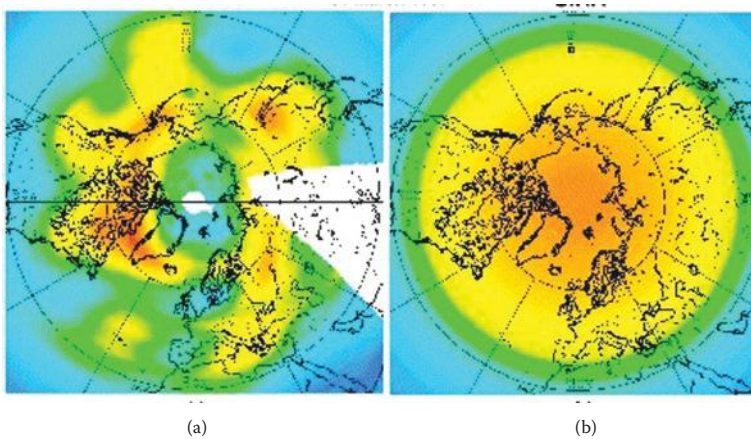


Figure 2.94 Images of ERS2 ozone sensor of the globe. (ERS-2/GOME; DLR, courtesy of DLR, Oberpfaffenhofen, Germany.)

daily weather watch following the movement of cloud patterns. The satellites Meteosat (over Africa), GOES 1 (over Venezuela), GOES 2 (over Hawaii), GMS (over the Philippines), and Insat (over the Indian Ocean) gather images every 30 minutes in the visible and thermal range. These may be geocoded and used in animations, which are commonly shown on television programs.

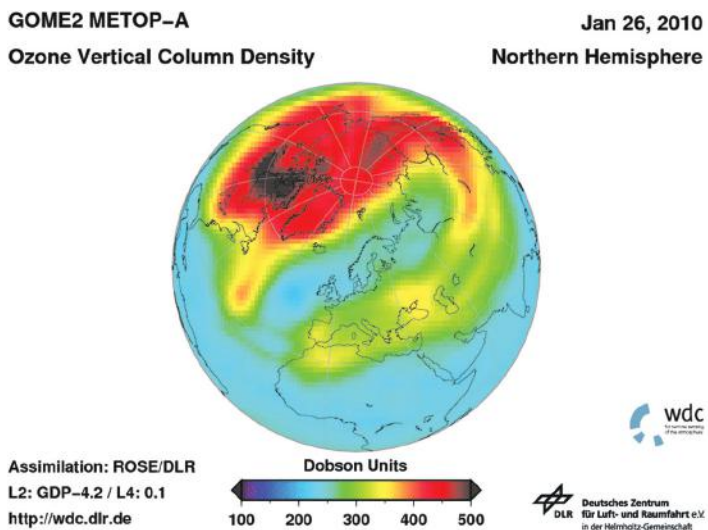


Figure 2.95 Image of Envisat Schiamachy GOME ozone sensor of the Northern Hemisphere. (From DLR, Oberpfaffenhofen, Germany.)

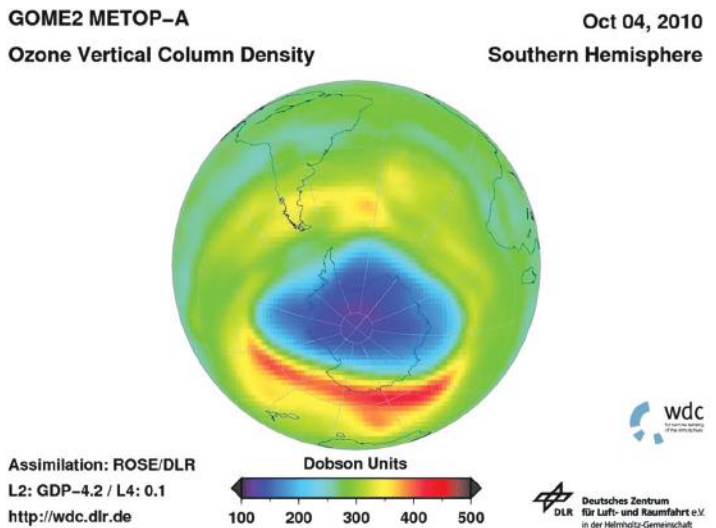


Figure 2.96 Image of Envisat Schiamachy GOME ozone sensor of the Southern Hemisphere. (From DLR, Oberpfaffenhofen, Germany.)

The data collected at an interval of 6 hours may be used to determine parameters of the radiative transfer model, into which the distribution of clouds, water, ice, snow, and the land mass is entered.

The combination of visual and thermal bands permits the visual separation of clouds, water, ice, snow, and land. If combined with atmospheric non-remote sensing measurements, a radiative transfer model can be arrived at. **Figure 2.97** shows the thermal GOES-1 image of a hurricane, and **Figure 2.98** gives a view of a hurricane with SeaWiFS from OrbView-2.

Rainfall

The measurement of rainfall is of great meteorological interest. The sources of worldwide rainfall data are rain gauges, which are very scarcely distributed over the globe. If no rain gauge data are available over a region, data from Meteosat, GOES, and so on relating to thermal bands can be used to determine cloud temperature. Cold clouds with <235 K temperature give an indication of possible rainfall.

On the U.S. military DMSP satellite, four wavelengths from 0.35 to 1.55 cm are provided for passive microwave sensing in two polarizations (HH, VV). The images of 55 km ground resolution permit the derivation of a scattering index, indicative of rainfall.



Figure 2.97 Thermal GOES image of hurricane. (Meteosat-3 MVISSR; Eumetsat, processed by DLR, courtesy of DLR, Oberpfaffenhofen, Germany.)



Figure 2.98 SeaWiFS OrbView-2 image of a hurricane. (From SEOS. EARSeL is a partner in the ESA project SEOS, Greece.)

Wind

Since wind drives ocean currents, scatterometers can measure the roughness of the sea to estimate wind vectors. Radar images are also able to detect roughness parameters.

Weather Prediction

Terrestrial measurements for weather forecasting can easily be combined with remote sensing data for cloud motion, the estimated precipitation, and the measurement of surface temperature.

Other phenomena detected from images are

- Analysis of snow cover
- Location and the motion of tropical storms
- Detection of fog and its dissipation

Climate Studies

Climate studies become possible by the comparison of NOAA-AVHRR aggregates on a seasonal and annual basis.

Oceanography

The geodetic aspects to be studied are ocean heights, as determined in the ERS1-Topex mission by radar altimeters. When related to the geoid, the data permit the derivation of ocean height (see [Figure 2.99](#)).

Let us now consider some phenomena of direct interest to remote sensing.

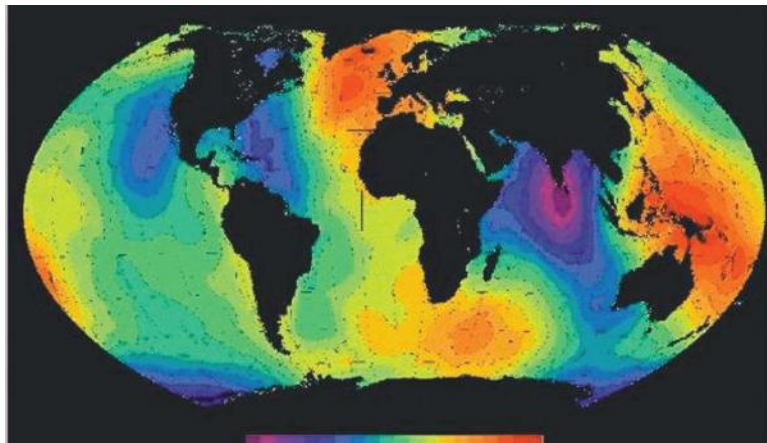


Figure 2.99 Heights from Topex altimeter ocean ERS-1. (Courtesy of DLR, Oberpfaffenhofen, Germany.)

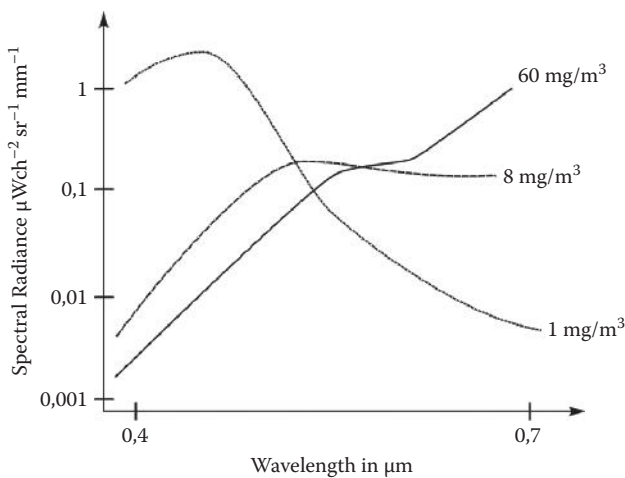


Figure 2.100 Spectral chlorophyll response at sea.

Ocean Productivity

The main objective of studying ocean productivity is to detect organic substances, such as phytoplankton, which are important for fisheries. It contains chlorophyll, which can be differentiated from suspended sediments prevalent near the coast and transported by estuaries (see Figure 2.100). Figure 2.101 shows an image of chlorophyll concentration and sediments in the Strait of Gibraltar.

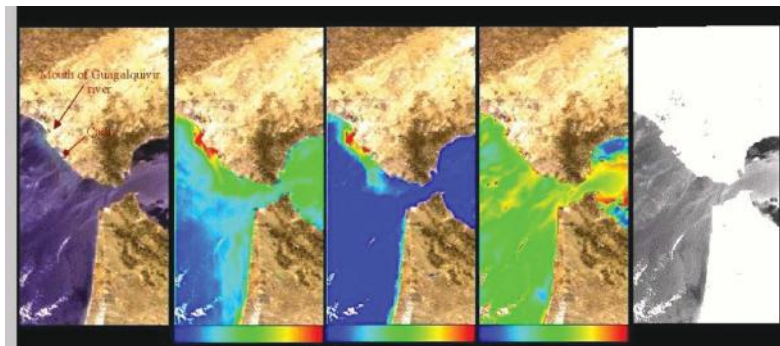


Figure 2.101 Chlorophyll separation of pigments, sediments, and aerosols from MOS. Images of IRS for the Strait of Gibraltar. (Left) Multispectral image followed by the separation of pigments (chlorophyll concentrations), sediments, and aerosol concentrations. (Right) A black-and-white image for the separation of clouds over the sea. Pigments in $\mu\text{g}/\text{l}$ (blue = 0, green = 3, red = 6; sediment: blue = 0, red = 5; aerosol optical thickness: blue = 0, red = 1). (MOS-IRS; DLR, courtesy of DLR, Oberpfaffenhofen, Germany.)



Figure 2.102 Algae bloom in the Bay of Bisquay. (From SEOS. EARSeL is a partner in the ESA project SEOS, Greece.)

Sediments reflect mainly in red. Therefore, a blue/green ratio can indicate the chlorophyll concentration at sea (see Figure 2.102 for algae bloom). The actual concentration can be calibrated by *in situ* measurements.

The satellites Nimbus 7 and OrbView-2 carried the sensor SeaWiFS for observation in eight channels at 1 km resolution with a swath of 2800 km. Of particular interest is the observation of sea surface temperature, which is made available at weekly intervals (see Figure 2.103 for the eastern Mediterranean Sea).

Ocean Currents

Ocean currents are visible along the coast because of plumes of suspended matter. In the midocean, the radiant temperature, which can be measured day and night by NOAA-AVHRR, shows the distribution of ocean currents. Global thermal phenomena, like El Niño, can be monitored by NOAA satellites (see Figure 2.104).

Radar images are also an indicator that can help to determine the level of surface roughness, since currents produce small waves.

Sea Ice

The principal objective of the Canadian Radarsat satellite is to be able to follow sea ice motion in the polar areas. In multitemporal mode the images can be observed in stereo, giving an indication of the direction of flow (see Figure 2.105).

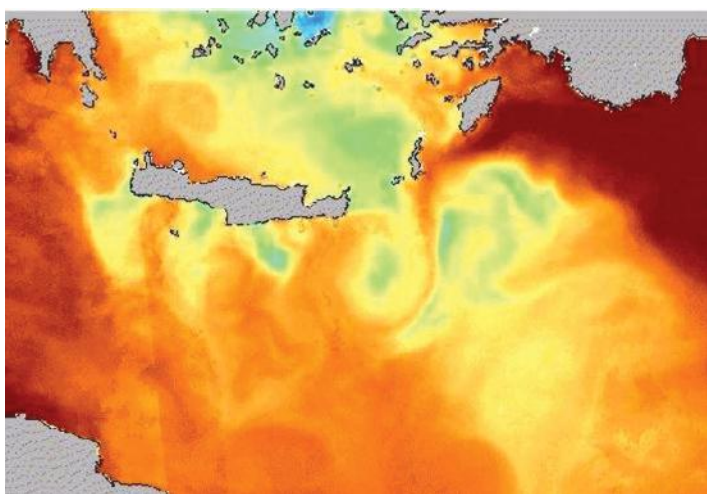


Figure 2.103 Sea surface temperature in the Eastern Mediterranean, weekly mean temperature, summer 1994. Dark red = 30°C, blue = 23°C. (From NOAA-AVHRR; DLR, courtesy of DLR, Oberpfaffenhofen, Germany.)

The ESA-ERS1/2 satellites have been able to classify Arctic sea ice. The thermal band six of Landsat TM can distinguish ice temperatures. Thin ice is warmer than thick ice.

The surface roughness of sea ice can be measured by nonimaging radar scatterometers, flown from aircraft at altitudes below 1 km.

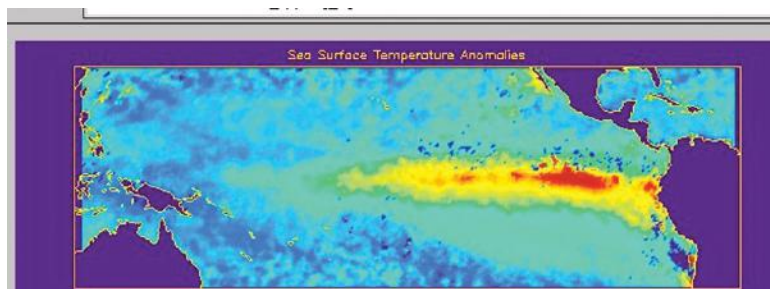


Figure 2.104 El Niño observed sea surface temperature anomaly by ERS along track scanning radiometer (monthly mean, October 1997). (From CEOS CDROM 98, courtesy of CNES, Toulouse, France.)

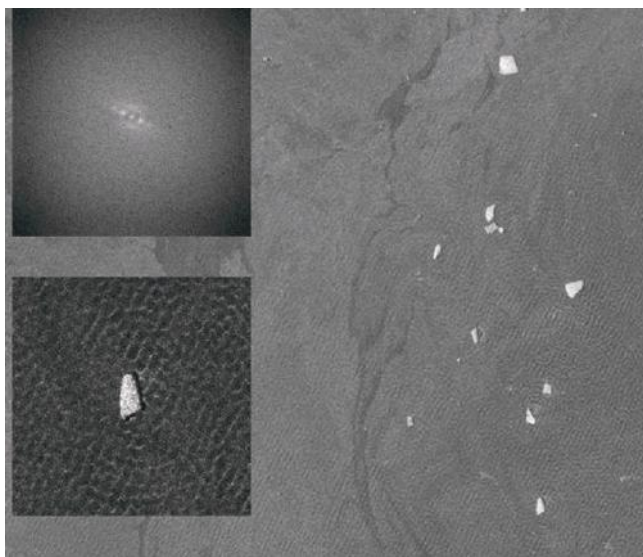


Figure 2.105 Radarsat image of icebergs on the west coast of Antarctica with wave patterns around the icebergs. (From ERS-1, © ESA, processed by DLR, courtesy of DLR, Oberpfaffenhofen, Germany.)

Bathymetry

Bathymetry at sea is generally made by sounding from ships, which have, however, difficulties in navigating in shallow areas. In these areas, remote sensing from aircraft and satellites can help to assess water depth, even though, depending on the turbidity of the water, light penetration and reflection is generally limited to not more than 10 m water depth. Figure 2.106 illustrates the transmission in water, which is best for the green band. A blue-green ratio can therefore be used for an assessment of water depth in shallow areas. Figure 2.107 shows the composition of the Wadden Sea near Wilhalmeshaven, Germany, at low tide.

Environment

Remote sensing concentrates on the detection of environmental pollution.

Hazardous Waste

The task to identify hazardous waste is to find its location, to map it, and to monitor it. If identification is not directly possible by visual inspection, the health of vegetation over the waste area can be a good indicator for hidden

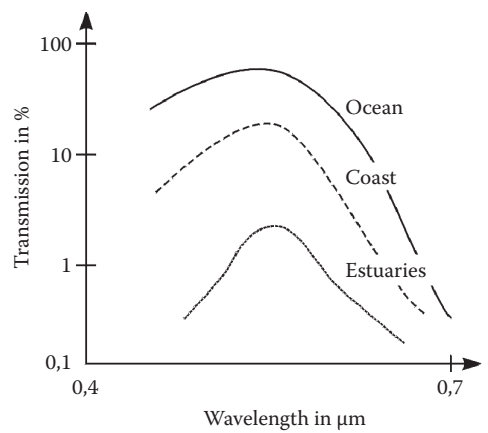


Figure 2.106 Water penetration in the visual spectrum.



Figure 2.107 Wadden Sea on the German North Sea coast near Wilhelmshaven at low tide. (IRS 1D-LISS image, SI/Antrix/Euromap 1998, GAF 2000, courtesy of GAF Remote Sensing and Information Systems, Munich, Germany.)

waste. A ratio of infrared-red is a good discriminator. Waste areas will usually have a low infrared-red ratio.

Plumes

Thermal pollution in water can be monitored by thermal infrared scanners operated from aircraft or by multispectral optical sensors from satellites. [Figure 2.108](#) shows the thermal pollution in the Po River, and [Figure 2.109](#) shows the sediment concentration caused by the Po River in the Adriatic Sea.

Oil Spills

Of particular environmental interest are oil spills at sea and in coastal regions. Due to its fluorescent properties, oil floating on water has a high reflectance in

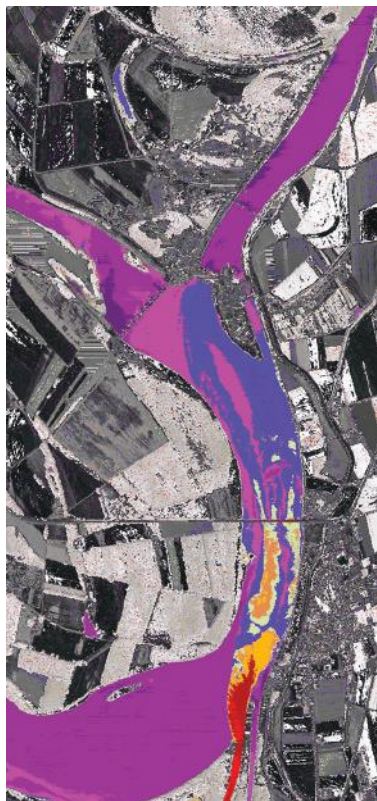


Figure 2.108 Po River thermal pollution. (Daedalus, DLR, courtesy of DLR, Oberpfaffenhofen, Germany.)

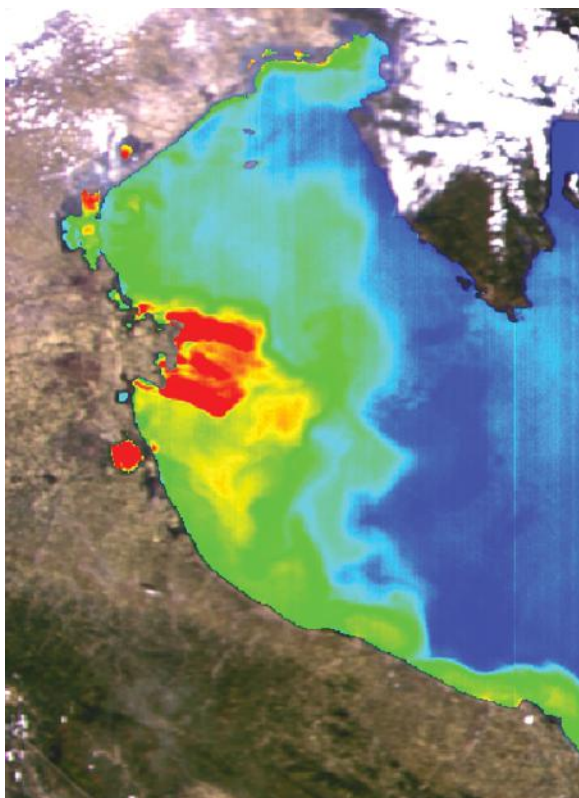


Figure 2.109 Sediment concentration at sea caused by the Po River in the Adriatic sea. (From MOS-IR; DLR, courtesy of DLR, Oberpfaffenhofen, Germany.)

the ultraviolet region (0.3 to 0.4 μm). An aircraft scanner operated from low altitude can be used to determine the thickness of the oil film on water.

On a more regional and global level, radar images permit the location of oil slicks. They dampen the natural roughness of ocean water. They are thus observable due to their low backscatter in the images. On a local level, laser scanners are able to differentiate between oil types (see [Figure 2.110](#) as an example for a ship accident near the coast of Northern Spain). Thermal images may also be of help, since the oil surface is cooler than the water.

Nonrenewable Resources

Locating nonrenewable resources is the task of geological and geophysical exploration.



Figure 2.110 Oil pollution after ship accident on the north Spanish coast. (From SEOS. EARSeL is a partner in the ESA project SEOS, Greece.)

Mineral Exploration

For the prospecting of minerals, the methodologies of structural geology are very important. Geological prospecting is difficult in areas covered by vegetation, however, it becomes easier in the dry belts of the globe.

Ore deposits are usually associated with structure zones. The interpretation of lineaments in the rocks permits the visible determination of fractures. Digital directional filtering of the images helps to better recognize these fractures. Fractures are often also combined with hydrothermal activity. Therefore, thermal aircraft scanners are useful in this respect. To identify the mineral composition of outcrops, hyperspectral scanners, such as AVIRIS, offer special possibilities to distinguish minerals of outcrops.

Oil Exploration

Remote sensing plays an initial role in oil exploration. The analysis of Landsat and radar images to determine the extent of sedimentary basins is usually the first step in oil exploration, even though a whole slate of geophysical prospecting methods must be applied to focus on potential exploration locations. These are

- Aeromagnetic surveys
- Gravity surveys
- Reflection seismology
- Drilling



Figure 2.111 Deforestation in Bolivia. (Courtesy of SEOS, Greece.)

Renewable Resources

The task of making an inventory and then monitoring renewable resources is intimately connected with the establishment of geographic information systems. It consists of compiling base data by standard mapping procedures, of supplementing these data by geocoded remote sensing data, and of adding attribute data from a multitude of sources.

Remote sensing has the advantage of quick acquisition of up-to-date images at adapted spatial and spectral resolution without limitations of costly ground access. It has the disadvantage that not all desired categories of information can be extracted from the images. **Figure 2.111** illustrates the deforestation observed from Landsat in Bolivia.

Land Cover and Land Use

Land cover describes the physical appearance of the earth's surface, whereas land use is a land right-related category of economically using the land. Remote sensing concentrates on observing land cover.

Land cover consists of classifiable terrain objects for which different governmental base data providers have implemented a number of object-oriented classification schemes. The UN Food and Agricultural Organization has devised a hierarchical land cover catalog suitable for the application of remote sensing and applicable to developing continents, such as Africa. It has been implemented in the Africover project distinguishing 90 different land cover classes in different East African countries.

The German Surveys and Mapping administration has devised an object-oriented land cover catalog with the following major categories:

1000	Text information
2000	Settlements
3000	Transportation
4000	Vegetation
5000	Hydrology and water
6000	Topographic elevation data
7000	Administrative boundaries

These major categories are subdivided into subclasses. Many of the subclasses can be identified and monitored with 85% accuracy by remote sensing at the global and regional or even at the local level. [Figure 2.112](#) shows the result of a land cover classification from an airborne multispectral scanner. As shown in [Figure 2.113](#), the result is significantly enhanced if it is merged with vector information from a GIS. [Figure 2.114](#) is an example of two satellite image-based classifications for the island of Tenerife, Canary Islands, with changes of land cover.

Vegetation

Of particular significance is the monitoring of vegetation. On a global level, this is done from NOAA-AVHRR images obtainable twice a day. Many of these images contain clouds, which have to be eliminated from the images. This is possible by taking all of the images of a 10- or 14-day period and substituting cloudless pixels into the data set.

Whereas the original 1 km resolution provides too much data, a reduced resolution of 4 km or 16 km can provide a global vegetation index data set. This is possible by the use of the ratio for the Normalized Difference Vegetation Index (NDVI):

$$\text{NDVI} = \frac{\text{Infrared} - \text{Red}}{\text{Infrared} + \text{Red}}$$

The calculated NDVI for each pixel can attain a value between 1 and -1.

Green vegetation has an NDVI of about +0.7 (shown in red in [Figure 2.115](#)), whereas water, barren lands, and clouds have an NDVI of about -0.3, shown in blue.

After radiometric calibration and the consideration of atmospheric scattering and geocoding are applied, the NDVI gives a clear indication of seasonal vegetation changes. On the Northern Hemisphere, greenness tends to rise in May, with a peak in July and a decrease until September. Yearly comparisons for the respective months can be useful for comparing crop estimates from year to year.



Figure 2.112 Daedalus aircraft scanner image over agricultural area. (Daedalus, © DLR, courtesy of DLR, Oberpfaffenhofen, Germany.)



Figure 2.113 Parcel-based land cover from DaedalusScanners image merged with GIS vector data. (Daedalus; DLR, courtesy of DLR, Oberpfaffenhofen, Germany.)

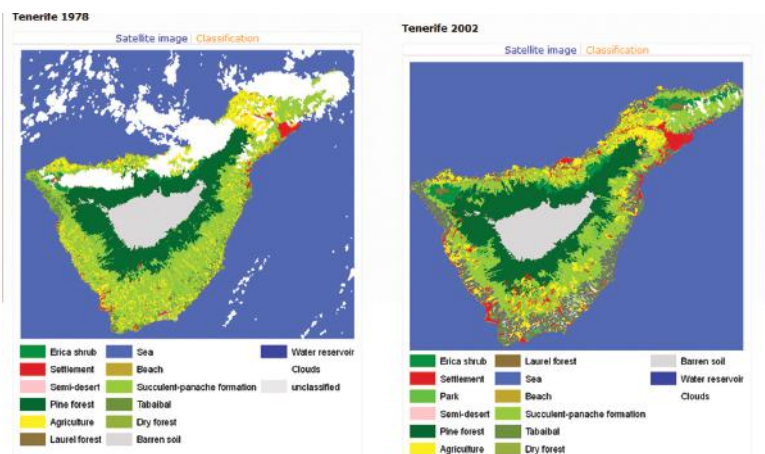


Figure 2.114 Land cover changes of Tenerife from supervised classification. (From SEOS. EARSeL is a partner in the ESA project SEOS, Greece.)

Another use of the NDVI is in the monitoring of tropical vegetation and the depletion of forests, or of agricultural crops (Figure 2.116 shows the application for a multispectral aircraft scanner in agriculture).

Natural Hazards

Earthquakes

Seismic risks are not directly observable by remote sensing. However, active faults may be visible in Landsat images, and the plate movements along these faults can be monitored by radar interferograms.

Landslides

Fresh landslides are observable in radar images.

Land Subsidence

Land subsidence can be interpreted from images by a change in drainage patterns and an observation of vegetation anomalies.

Volcanoes

Volcanic eruptions are associated with clouds of ash, slope changes, and mudflows. Changes in topography can be monitored by radar interferometry, but it is also possible to use thermal images from Landsat TM and from aerial scanners to study changes in heat emission.

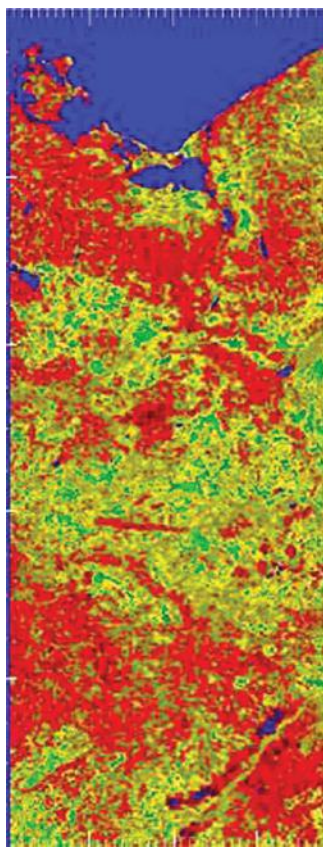


Figure 2.115 NDVI of the Oder region from MOS on IRS from channels 7 (651 nm) and 11 (869 nm). (MOS-IRS; DLR, courtesy of DLR, Oberpfaffenhofen, Germany.)

Floods

Floods can easily be monitored with radar images. Figures 2.117 and 2.118 show multitemporal images of a river flood on the Oder River along the German-Polish boundary.

Forest and Grass Fires

In fire monitoring, three stages are important:

1. Determination of fire hazards—An index with data indicating humidity, wind speed, cloud cover, ground temperature, and green composition of the land can be formed to judge fire potential.
2. After a fire has broken out, NOAA-AVHRR can monitor the extent of the fire in the thermal band. A band 1, 2, and 4 combination can

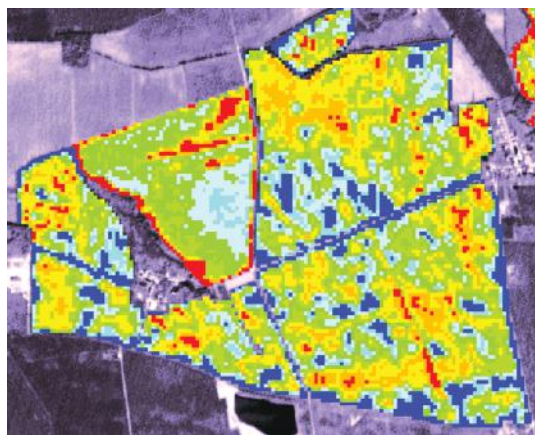


Figure 2.116 NDVI from DaedalusScanners for an agricultural area. (NDVI image: SI/Antrix/Euromap 1997, GAF 1999, courtesy of GAF Remote Sensing and Information Systems, Munich, Germany.)

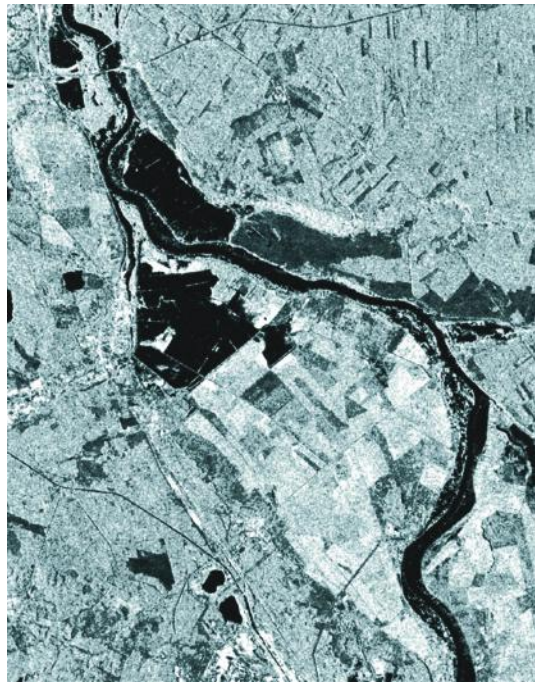


Figure 2.117 Radarsat flood image of the Oder River. (© Radarsat 1997, GAF 1997, courtesy of GAF Remote Sensing and Information Systems, Munich, Germany.)

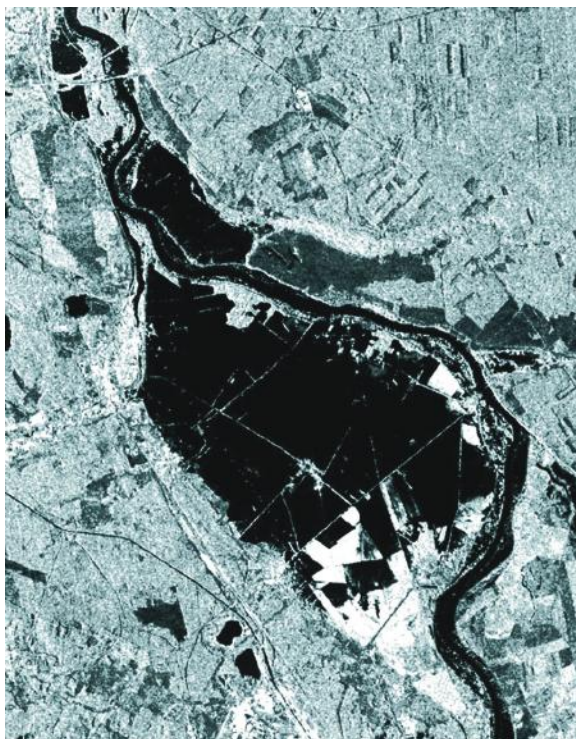


Figure 2.118 Radarsat sequential flood image of the Oder River. (© Radarsat 1997, GAF 1997, courtesy of GAF Remote Sensing and Information Systems, Munich, Germany.)

distinguish smoke and differentiate between burned and unburned areas.

3. After a fire, damage assessment can be made with the help of the images. **Figure 2.119** shows the NOAA image of a forest fire along the Siberian–Chinese border.

Environmental awareness has prompted the European Space Agency to launch a series of dedicated satellites for the Global Monitoring for Environment and Security (GMES) program starting with the launch in 2013. This program was renamed in 2013, as “Copernicus.”

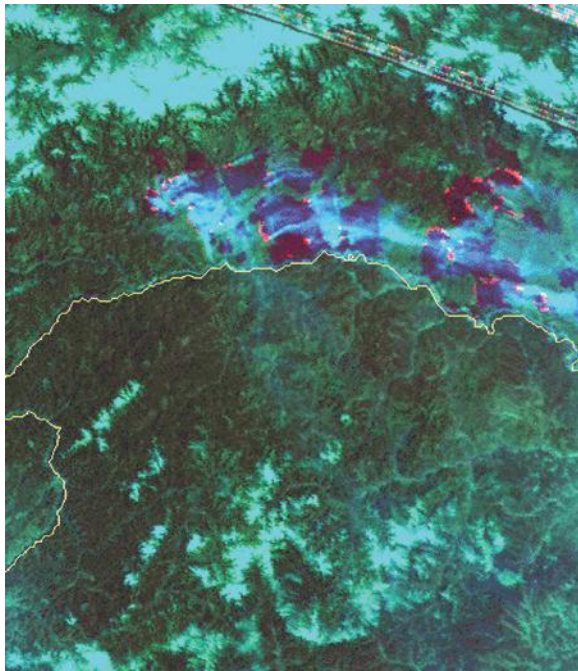


Figure 2.119 Forest fire at the Siberian–Chinese boundary. (Image from CEOS CDROM 98, courtesy of CNES, Toulouse, France.)

The Sentinel satellites focus on:

- Sentinel 1—Synthetic aperture radar applications in C-band to monitor sea ice, the marine environment, and land surface risks
- Sentinel 2—A multispectral earth observation system for disaster relief of the SPOT type
- Sentinel 3—An ocean-oriented satellite to monitor ocean color, sea surface topography, and sea temperature